Report
**R-21-13**
June 2021

# Exploratory integration of discrete fracture network models and 1D stress models with data from hydraulic tests for the shallow bedrock at the Forsmark site

**Lee Hartley**
**Steven Baxter**
**James Carty**
**Simon Libby**

SVENSK KÄRNBRÄNSLEHANTERING AB

SWEDISH NUCLEAR FUEL
AND WASTE MANAGEMENT CO

Box 3091, SE-169 03 Solna
Phone +46 8 459 84 00
skb.se

SVENSK KÄRNBRÄNSLEHANTERING

ISSN 1402-3091
**SKB R-21-13**
ID 1883765
June 2021

# Exploratory integration of discrete fracture network models and 1D stress models with data from hydraulic tests for the shallow bedrock at the Forsmark site

Lee Hartley, Steven Baxter, James Carty, Simon Libby
Golder Associates UK, Ltd

*Keywords:* DFN, Numerical modelling, Sheet joints, Hydraulic data, ECPM.

# Abstract

The hydrogeological characterisation of the Forsmark Site has identified significant differences in the hydraulic properties of the bedrock with increasing depth within the tectonic lens. This has been attributed to sub-horizontal fracturing at shallow depths (< 100 m) some of which may have formed due to stress changes associated with glaciations. These structures are termed sheet joints. These relatively continuous and high aperture fractures significantly increase the lateral permeability of the bedrock. Although such shallow bedrock features were acknowledged in SDM-Site, their characterisation was limited by the casing of core drilled boreholes in the upper c 100 m. New core drilled boreholes drilled in the area targeted for the accesses of the spent nuclear fuel repository now provide a substantial dataset with which to better quantify and model the geometry and hydraulic properties of these sheet joints.

The sheet joints form an important component of the natural fracture system in the Forsmark tectonic lens. To understand the hydraulic system, however, one needs to characterise each part the system: deformation zones, ancient sub-vertical and sub-horizontal fractures and the sheet joints. Therefore, a discrete fracture network (DFN) model is developed combining each part of the bedrock system.

In this work, the geometric aspects of the background (non-sheet joint) modelled fractures are configured in the same stochastic manner as per SDM-Site, with the sheet joint geometric aspects calibrated according to mapped sheet joint traces and connectivity constraints determined from hydraulic modelling. The hydraulic properties of the modelled fractures include the influence of bedrock stress controlling transmissivities, their depth trend and orientation dependence. The calibration data for the hydraulic modelling includes both logged borehole flows using steady-state flows (Posiva Flow Logging), and transient interference test responses.

The key output of this analysis and modelling exercise is an updated hydrogeological property model extrapolated over the local catchment area, 22 km by 20 km, for input to hydrological modelling of the environmental impacts of construction of the facility. The model development has allowed prototyping of new methods in data management, model conceptualisation and hydraulic calibration, which informs the definition of new DFN methodologies. However, since the focus is on updating the characterisation of the upper bedrock within the Forsmark tectonic lens, it does not represent a complete implementation of the methodology or to the whole Forsmark catchment volume.

As part of this work a PostgreSQL database was developed that allowed rapid access to both data and data processing routines targeted at numerical modelling tasks. Key differences with existing databases are its ease of extension, supporting both Python and SQL scripts with support for sophisticated spatial functions, and ease of access, supported by QA and audit trails. It is envisaged that the database could act as ‘hot’ storage, supporting cross-disciplinary interpretations, but with existing databases remaining as ‘cold’ storage, acting as a fixed record of raw source data.

# Sammanfattning

Den hydrogeologiska karakteriseringen av berggrunden i Forsmark har identifierat betydande skillnader i berggrundens hydrauliska egenskaper med ökande djup inom den tektoniska linsen. Dessa anses bero på subhorisontella sprickbildningar på grunt djup (< 100 m), s k bankningsplan. En del av bankningsplanen har troligtvis uppkommit i samband med spänningsförändringar i anslutning till den senaste inlandsisens framväxt och tillbakadragande. De bankningsplanen som påträffats inom den tektoniska linsen i Forsmark i området ovanför det planerade djupförvaret är långa (kontinuerliga) med stora sprickaperturer, vilket sammantaget ökar den ytnära berggrundens laterala transmissivitet avsevärt. I SDM-Site begränsades möjligheterna till avancerad strukturgeologisk modellering av bankningsplanens utbredning och bra hydraulisk karaktärisering av deras transmissivitet av det faktum att de flesta av kärnborrhålen i den tektoniska linsen hammarborrades och därefter fordrades med stålrör de översta ca 100 m. Kärnborrhål som borrats efter SDM-Site, i nära anslutning till det s k tillfartsområdet, har inte dessa begränsningar, vilket innebär att det idag finns ett betydligt bättre dataunderlag för att kvantifiera och modellera de ytnära bergets geometriska och hydrauliska egenskaper.

Bankningsplanen utgör en viktig komponent av det naturliga spricksystemet inom den tektoniska linsen. För att fullt förstå det hydrauliska systemet måste man emellertid förstå och karakterisera alla delar av spricksystemet: deformationszoner, äldre subvertikala och subhorisontella sprickor i bergmassan mellan zonerna, samt de relativt sett yngre bankningsplanen. Därefter kombineras de olika delarna av spricksystemet till en diskret spricknätverksmodell (DFN) för hela bergsystemet.

I detta arbete har är de geometriska egenskaperna hos sprickor som inte tolkats vara bankningsplan modellerats på samma (stokastiska) sätt som i SDM-Site. Sprickor som tolkats vara bankningsplan har i detta arbete kalibrerats mot karterade strickspår. Tillräcklig konnektivitet vid hydraulisk simulering av utförda enhålstester och mellanhålstester har också varit ett kriterium för den hydrauliska kalibreringen. De hydrauliska egenskaperna hos modellerade sprickor inkluderar hydromekanisk koppling, djuptrend och orienteringsberoende.

Det viktigaste resultatet av utfört arbete är en uppdaterad hydrogeologisk egenskapsmodell för spricksystemet i Forsmark. Modellen är extrapolerad över det lokala avrinningsområdet, som är ca 22 km gånger 20 km stort. Den uppdaterade hydrogeologiska egenskapsmodellen kan användas som indata till olika typer av hydrologiska/hydrauliska studier, t ex simulering av potentiella hydrologiska miljöeffekter orsakade av undermarkskonstruktioner. Modellutvecklingen har möjliggjort prövning och testning av nya metoder till gagn för utvecklingen av en ny metodik för DFN modellering, t ex inom datahantering, modellkonceptualisering och hydraulisk kalibrering. Eftersom fokus i utfört arbete har legat på att uppdatera den strukturella-hydrauliska karakteriseringen av den övre delen av berggrunden inom den tektoniska linsen i Forsmark, behövs det dock mer utvecklingsarbete innan metodiken kan implementeras fullt ut och tillämpas inom alla delar av berggrunden inom Forsmarks avrinningsområde.

Som en del av detta arbete utvecklades en PostgreSQL-databas som möjliggjorde snabb åtkomst till både data- och databehandlingsrutiner riktade mot numeriska modelleringsuppgifter. Viktiga egenskaper hos en PostgreSQL-databas är: enkel dataåtkomst/-hantering, lämplig för skript programmering med såväl Python som SQL, vilket innebär tillgång till sofistikerade rumsfunktioner, god kvalitetssäkring och spårbarhet. Man kan se den utvecklade PostgreSQL-databasen som en ”het” lagringsplats i syfte att möjliggöra/underlätta tvärvetenskapliga tolkningar, medan den befintliga (traditionella) databasen (Sicada) i princip är ”kall” lagringsplats för ”rådata” med få eller inga visualiserings och tolkningsfunktioner.

# Contents

# 1 Introduction

The Swedish Nuclear Fuel and Waste Management Company, SKB, has undertaken site characterisation at Forsmark as part of identifying a suitable location for geological disposal of spent nuclear fuel. A conceptual model of the geological environment at the Forsmark site, termed the site descriptive model (SDM), has been constructed, and is detailed in the SDM-Site report (SKB 2008).

## 1.1 Background

In SDM-Site, the hydrogeological model of the bedrock system within the prioritised area/volume for the spent fuel repository was conceptualised as a shallow hydraulic system with aquifer type properties on top of a deep hydraulic system with aquitard type properties. The average depth to the interface between the two hydraulic systems was envisaged to be approximately 150 m (−150 m elevation) (Follin 2008).

The porous medium analogy of an aquifer on top of an aquitard is purely schematic as the bedrock is not porous but fractured. The shallow hydraulic system has a larger hydraulic diffusivity (transmissivity (T) divided by storativity (S) for fracture representation, or hydraulic conductivity (K) divided by specific storage ($S_s$) if regarding as an equivalent continuous porous medium). This is not an uncommon situation for crystalline rock in Sweden. The stress release following the last deglaciation and its impact on the occurrence of near surface sub-horizontal bedrock structures, so-called sheet joints, and their impact on near surface hydrogeology is well recognised across Fennoscandia (Morland 1997, KASAM 2001, Gudmundsson et al. 2002, Mäkelä 2012. Lunkka et al. 2013). What makes the prioritised area/volume in Forsmark remarkable compared to many other studied crystalline rock sites in Sweden is the extreme contrast in hydraulic diffusivity of the near surface system compared to the deep system; the hydraulic diffusivity of the shallow system is approx. 10 –1 000 $m^2/s$, whereas the hydraulic diffusivity of the deep system is approx. 0.01–1 $m^2/s$ depending on depth. By comparison, the hydraulic diffusivity of the shallow system around the final repository for short-lived radioactive waste (SFR) was around 1–10 $m^2/s$ according to the SDM of the extension of the SFR (SDM-PSU) (Öhman et al. 2012).

The focus of the hydraulic characterisation (Follin 2008) and discrete fracture network (DFN) modelling (Follin et al. 2007) for SDM-Site performed between 2002 and 2007 was the deeper bedrock system as the host rock for the repository. Posiva flow log (PFL) flow and fracture logging began at approximately 100 m depth in most core drilled (KFM) holes below the casing. PFL logging was performed in KFM01A, -01D, -2A, -02B, -03A, -04A, -05A, -06A, -07A, -07C, -08A, -08C, -08D, -10A, -11A. Double-packer injections tests in 5 m intervals in the shallow bedrock were performed in KFM01B, -03B, -06B, -07B, -08B, -09B. Fracture logging at shallow depths is also available in percussion drilled (HFM) holes, but hydraulic characterisation is limited to impeller flow logging or double-packer injection tests to identify the most conductive intervals rather than continuous logging of discrete flows.

Additional boreholes have been drilled in 2011 (KFM12–23) and 2016 (KFM24), which provide substantial extra fracture and hydraulic data for the shallow bedrock system, particularly around the access area and toward the north close to SFR.

## 1.2 Outstanding issues

The hydraulic testing in SDM-Site revealed a significant hydraulic anisotropy in the shallow system where the horizontal conductivity was much larger than the vertical. For instance, hydraulic responses were observed laterally across large distances during two large-scale interference tests conducted 2006 and 2007, respectively. Together with other significant hydraulic observations inside the so-called Forsmark tectonic lens, such as (i) high specific capacities (Q/s in [$m^2/s$]) of shallow groundwater wells, and (ii) similar levels of the “water table in the upper rock” in a larger number of shallow

groundwater wells, the interference test responses were thought to be caused by the combination of two structural phenomena: 1) a high conductive fracture frequency (CFF in [$m^{-1}$]) throughout the shallow system of fractures (associated with fracture domain FFM02), and 2) presence of an unknown number of presumably extensive and irregular sub-horizontal structures in the uppermost 150 m of rock. The combination of these two structural phenomena was conceptualised as a "shallow bedrock aquifer system" within the prioritised area for the planned deep geological repository, cf. above.

As mentioned above, the conceptual models invoked for 1) and 2) were based on sparse information and uncertain assumptions. First, the estimated value of CFF was based on flow logging data acquired in the limited number of cored boreholes where the thickness of the shallow system was thicker than the 100 m long casings installed in the top part of each cored borehole (telescopic drilling). Second, there was no structural model for the sub-horizontal structures reported by the geologists (cf. below), and hence only acquired hydraulic data was available to parameterise a groundwater flow model.

For the sake of groundwater flow modelling in SDM-Site, a purely hypothetical structural model consisting of three parallel structures at 40 m, 80 m, and 120 m depth, respectively, was assumed for the shallow bedrock system. The hypothetical structural model was parameterised using hydraulic data from single-hole tests and the ECPM properties were calibrated to match observed interference test responses. Nevertheless, none of the calibrated ECPM flow models used in SDM-Site were able to reproduce the low groundwater levels observed in the groundwater wells drilled into the shallow system of fractures. The best match was obtained if the anisotropy of the hydraulic conductivity of the ECPM model for the shallow system was significantly modified (increased anisotropy with Kxx and Kyy >> Kzz).

The occurrence of presumably extensive and irregular sub-horizontal structures in the uppermost ca 150 m of rock was not a prioritised subject for the geological/geometric modelling during the site investigation; in SDM-Site. In effect, there is at present no structural model for the hydraulic observations at hand inside the tectonic lens and hence no support for the construction of a robust hydrogeological model of the shallow system that can be implemented, parametrised, and tested by means of groundwater flow modelling.

It is noted that geological/geometric modelling of extensive and irregular sub-horizontal structures occurring in the uppermost 150 m of rock in Forsmark is not as straightforward as it may seem. First, until recently there were few drill cores from this depth to examine as most of the cored boreholes have a steel casing down to approximately 100 m depth and geological markers of deformation such as rock alteration, fracture frequency, etc are of little or no use in percussion-drilled boreholes. Second, sub-horizontal structures rarely outcrop or are difficult to trace on topography. Third, they are not readily identified below ground surface using conventional geophysical methods. Furthermore, the occurrence and genesis of very shallow sub-horizontal structures within the prioritised area/volume are most likely different from the genesis of deeper sub-horizontal structures. That said, the most superficial ones are probably classic sheet joints, i.e., caused by changes in vertical stress during one or several glaciations and deglaciations, whereas the deeper ones are more likely splays to the significant gently dipping deterministic deformation zone ZFMA2, which outcrops NW of Lake Bolundsfjärden. The orientation (strike/dip, right-hand rule method) of ZFMA2 is 080/24.

The structural-hydraulic model for the shallow system therefore needs to be revised. The newly acquired data from KFM13–KFM24 includes fracture locations, orientations, properties and flow logging allowing the properties of individual fractures as well as networks to be analysed and implemented as (DFN) models when simulating realisations of the fracture system. By building on the DFN descriptions for the deeper bedrock in SDM-Site (Follin 2008) an integrated model for both parts of the system can be made as the foundation for the hydrogeological property model of the complete bedrock system. A further component of this system is the deterministically modelled deformation zone model that extends through both shallow and deep parts of the bedrock. This includes the structural models by Stephens et al. (2007, 2015) and Curtis et al. (2009) and was further updated during 2018 based on the modelling reported by Follin (2019).

The key result of this analysis and modelling exercise is a hydrogeological property model that extends over the local catchment area (see Figure 4-29), 22 km by 20 km, for input to hydrological flow modelling to assess the environmental impacts of construction of the facility.

## 1.3 Approach and scope

SKB are currently updating their methodologies for Geological, DFN, Rock Mechanics, Hydrological-Hydrogeological Flow and Transport modelling to be used in future updates of site models during the pre-construction, construction and operational periods of the spent fuel repository and the extension of the existing repository for low and intermediate radioactive waste (SFR). These methodology updates were not completed during the study described here. However, some elements of these methodologies have been prototyped or expanded relative to what was done in SDM-Site.

Some notable examples of methodology prototyping work include:

- Integration of geometric, structural, and hydraulic borehole data with interpretations and models in a "spatially aware" database environment.
- Formulating fracture transmissivity through a hydromechanical coupling to stress to describe hydraulic anisotropy and depth dependencies.
- Calibrating DFN connectivity and hydraulic properties by simulating hydraulic tests in each individual borehole in the contact of its geological setting.

Since a complete update of both data and DFN modelling methodology is beyond the scope of this study, the hydrogeological property model developed here is only an interim delivery. The workflow involves the following main steps:

- Interpret a suitable fracture network orientation model for each borehole considering fracture orientations, foliation orientations, trends with depth and mineralogy.
- Review the definition of fracture domains defined in SDM-Site (Olofsson et al. 2007) as appropriate for describing differences in fracture statistics in the shallow bedrock system.
- Derive fracture orientations and intensity statistics by fracture domain as input to DFN models.
- Analyse possible fracture size distributions for sheet joints from mapping of the inlet channel for the Forsmark power plant during its construction (Carlsson 1979).
- Analyse the relationship between transmissivity and 1D stress model for deformation zones to derive a suitable hydromechanical model predicting trends with orientation and depth (after Follin and Stigsson 2013).
- Analyse the relationship between transmissivity and 1D stress model for fractures outside deformation zones to confirm the above.
- Build a DFN model of open fractures integrated with the deformation zone model for an area covering the Forsmark tectonic lens.
- Simulate hydraulic tests in 23 KFM and HFM holes to calibrate the model and quantify the sensitivities to fracture size and transmissivity distributions.
- Upscale a selected a DFN realisation to equivalent continuous porous medium (ECPM) and extrapolate these properties over the catchment area.

In summary, the scope of this project is comprehensive in the sense that it covers a complete workflow from integration of the primary with the latest geological models, through DFN conceptualisation, hydraulic calibration to delivery of the catchment-scale hydrogeological property models. However, it is focused on updating the near surface description and only parts of the evolving DFN modelling methodology are prototyped. For example, the model reported here considers open fractures to be conductive over their whole surface, as in SDM-Site and SDM-PSU, whereas the ongoing work with new DFN modelling methodology would model all fractures and consider alternative forms of intra-plane heterogeneity.

## 1.4 Conceptual framework for structures

The description of bedrock fracturing at Forsmark, the DFN model, involves describing a system of structures of different types and scales as sketched in Figure 1-1. Analysing the effects of hydraulic disturbances during construction and long-term effects of natural dynamic processes are most concerned with deformation zones and the fractures associated with them on scales of hundreds of metres to kilometres. Assessment of flow and advective transport in and around the deposition areas is concerned with fractures on the scale of decimetres to hundreds of metres. Near surface mechanical

stability, flow and transport also have to evaluate sheet joints that are typically on scales of tens to hundreds of metres. On the smallest scale, micro-structures of millimetres to decimetres collectively host significant volumes of water and minerals that determine the retardation of contaminants moving through the fracture system. The current study considers fractures from metre scale to deformation zones of order ten kilometres in length.

## 1.5 Acronyms used in this report

| | |
|---|---|
| CFI | Cumulative Fracture Intensity |
| CFF | Conductive Fracture Frequency |
| DFN | Discrete Fracture Network |
| DZ | Deformation Zone |
| ECPM | Equivalent Continuous Porous Medium |
| FORSIDE | FORsmark Site Interpretative Database Environment |
| HDM, HFR | Percussion-drilled boreholes |
| KFM, KFR | Core-drilled boreholes |
| PDZ | Possible Deformation Zone |
| PFL | Posiva Flow Log |
| PSU | SFR extension project |
| RD | Rock domain |
| SDM | Site Descriptive Model |
| SFR | Short-lived radioactive waste Final Repository |
| SICADA | SKB database |
| ZFM | deformation Zone at Forsmark |

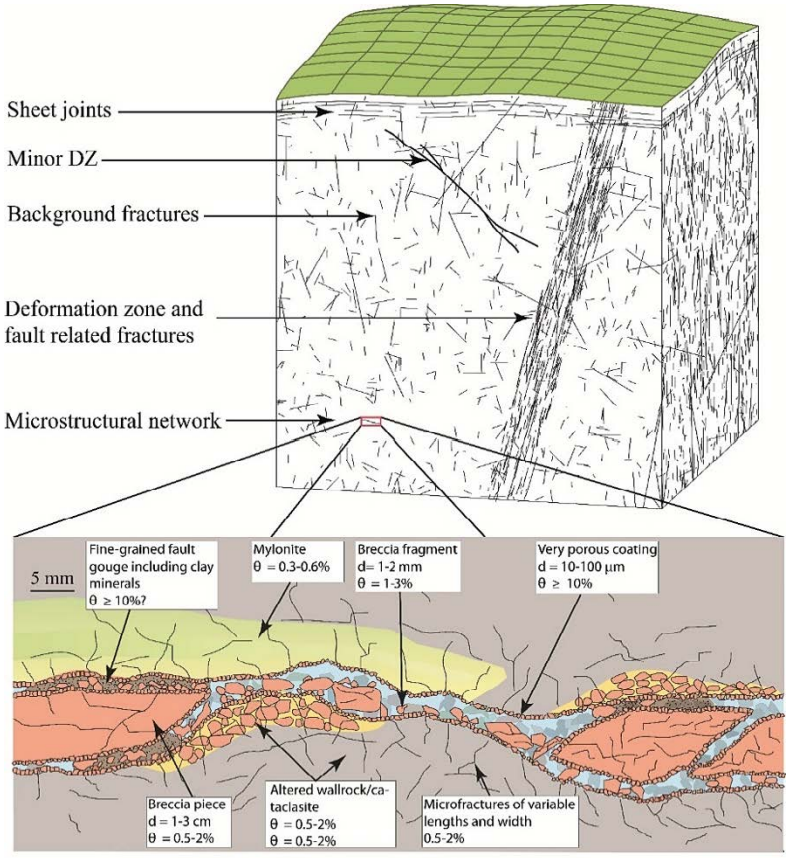


***Figure 1-1.*** *Conceptual framework for fractures of different types and scales. The insert shows a highly magnified schematic of fractures at the microstructural scale (after Winberg et al. 2003), which can be down to the scale of the micro-fissures between individual grains.*

# 2 Overview of the study area and available data

This chapter introduces the areas considered in the modelling and site data used in this study.

## 2.1 Extent of modelled and investigations areas for this study

Several different model areas are relevant to this study:

- The catchment area for which a hydrogeological property model is required has an origin at (154750, 6689970), a rectangular region extending 22 km east–west and 20 km south–north and to an elevation of −1 000 m (see Figure 4-29).
- The local-scale area for geological modelling including the deformation zone model that is aligned to northeast, a rectangular region extending 15 km NW–NE and 11 km SE–NW.
- The facility-scale area relevant to the interference tests around the Forsmark tectonic lens where a DFN model has been generated. The facility-scale DFN modelling area (1.9 km radius red circle), traces of the deformation zones (grey lines) and the borehole locations (collars shown as dots) are shown in Figure 2-1.
- Borehole-scale DFN models used to simulate single-hole hydraulic tests, circles extending 250 m beyond any point along the hole.

All coordinates given in this document are in the SWEREF 99 18 00 RH 2000 coordinate system.

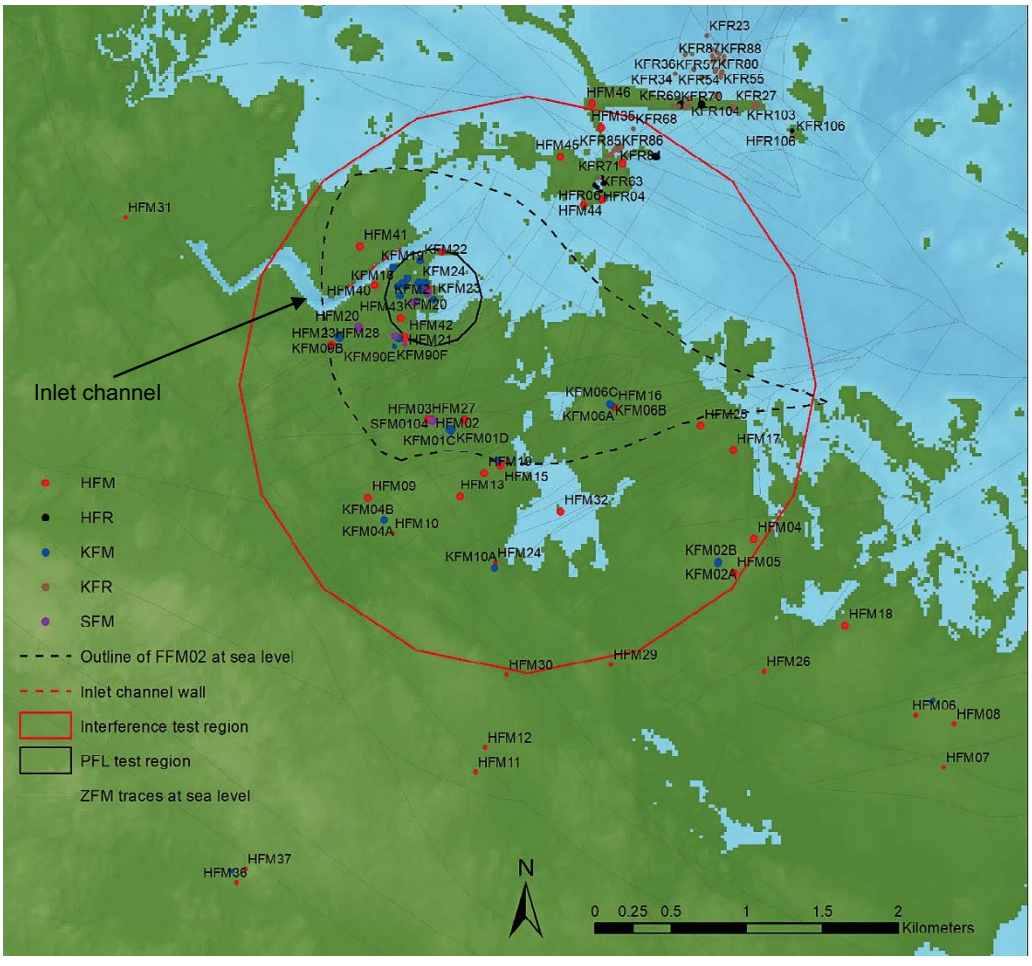


***Figure 2-1.*** *Map showing the location of boreholes, regions and traces of ZFMs. The larger borehole markers indicate boreholes that were monitored during one of the interference tests.*

## 2.2 Available borehole data

Borehole data was obtained for all core drilled holes at Forsmark (KFM) and at SFR (KFR) and all percussion drilled holes (HFM and HFR) from SICADA. Figure 2-1 shows the locations of all boreholes for which data was available and loaded into the modelling database. As noted earlier, many of the KFM holes are cased in the top 100 m, Figure 2-2 gives an indication of the holes for which there is data for the near surface within the facility-scale DFN area (red circle).

Besides borehole geometry (trajectories) the types of borehole data used include:

- Rock type interpretations.
- Single-hole interpretations of borehole intercepts with deformation zones.
- Structural mapping of fractures (depths, intensity, orientations, alteration, mineral types, apertures).
- Crush zones.
- Structural mapping of ductile structures (foliations, brittle-ductile or ductile shear zones).
- P-wave velocity.
- Transmissivity measurements from various types of hydraulic tests; PFL sequential logging (5 m section) and PFL-f difference logging (c 0.1 m resolution), impeller flow logging and double packer injection tests (PSS).

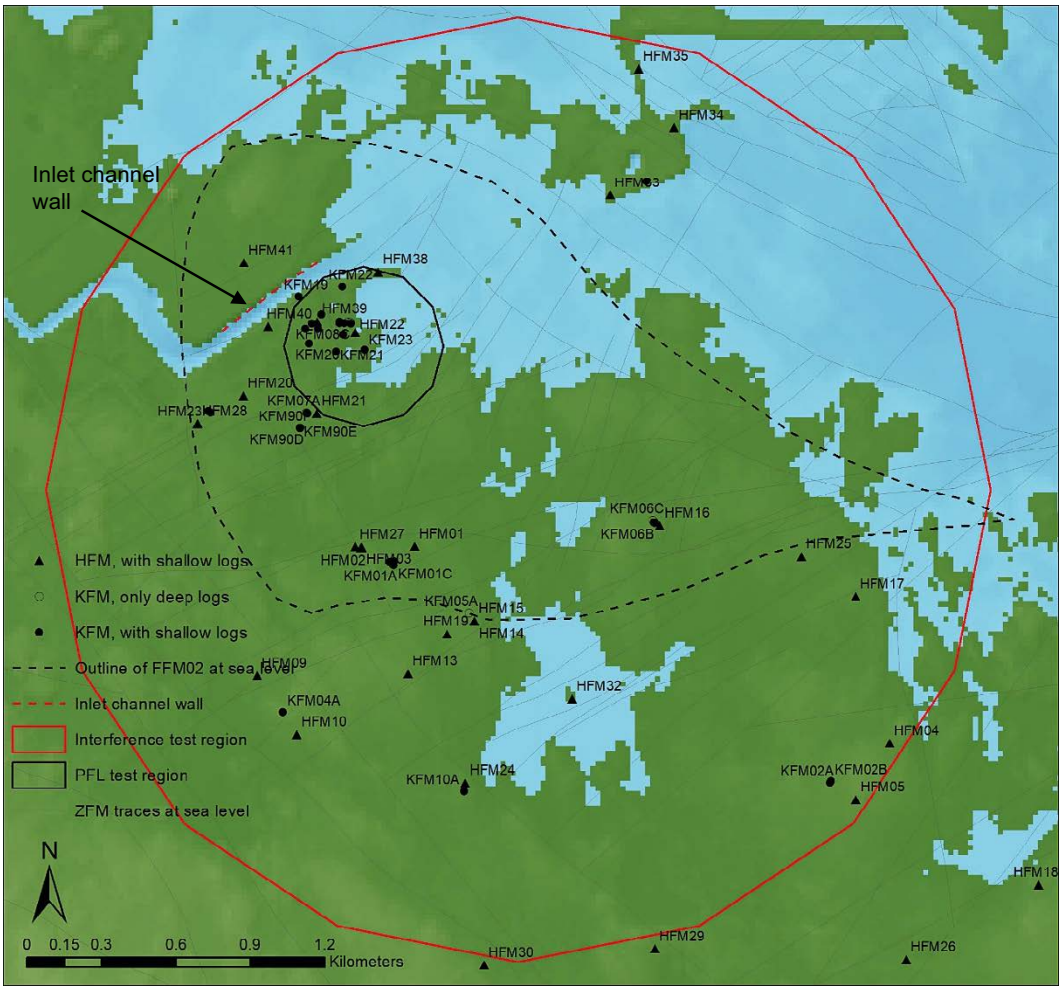


***Figure 2-2.*** *Map showing HFM and KFM boreholes with shallow (< 100 m depth) and deep (> 100 m depth) structural logs. The red circle shows the facility-scale model region used to simulate the interference test in HFM43.*

In order to make statistical analyses of the fracture properties it is first necessary to divide the rock into a set of fracture domains. Fracture domains provide a framework for describing overall spatial heterogeneity in rock fracturing. The goal behind identifying fracture domains is to find rock volumes with fracture characteristics such that the statistical variability between volumes is larger than the intrinsic fracture variability within volumes (Munier et al. 2003, Darcel et al. 2012, 2013), in line with geologic best practice. As such, fracture domains should form the basic divisions over which spatial heterogeneity in rock fracturing is characterised but may not, necessarily, correspond to the limits of other geologically significant volumes such as those defined in the Rock Domain (RD) model although this is generally the case.

Based on mainly borehole data, six fracture domains inside and immediately outside the proposed repository volume at Forsmark were identified in SDM-Site (Olofsson et al. 2007), see Figure 2-7. The main fracture domains of interest in this study are FFM02, which is a near surface domain, and the uppermost parts of FFM01 and FFM06, which represent different parts of the deeper rock below FFM02, where the spent fuel repository will be constructed. Together, the three fracture domains represent the Forsmark tectonic lens to the west of the major sub-horizontal zone ZFMA2. As part of this study, FFM02 is split into an upper FFM02U and lower FFM02L domain based on the new area from the planned access area, Figure 2-9. All data outside of these domains is treated as belonging to an "outside lens" domain. The upper domains are split at an elevation of −30 m (pers. comm. Jesper Petersson and Peter Hultgren, 2019).

Table 2-1 and Table 2-2 provide lists of how much borehole coverage there is by the different fracture domains and depths. Table 2-1 also indicates the depths below which PFL-f logging was performed. There are only 7 boreholes with PFL difference logging at shallow depths. Table 2-3 gives overall percentages of the rock types in each fracture domain. The rock inside FFM01/02/06 is over 80 % granite or granodiorite, while outside it is more mixed with felsic to intermediate volcanics, amphibolite and pegmatite.

**Table 2-1. List of KFM boreholes indicating the borehole length of fracture mapped interval, the borehole length to start of PFL logging, the borehole length inside and outside the Forsmark Lens, and the % of the logged fractures with sufficient orientation data to define a fracture set.**

| idcode | Fracture mapped interval | PFL-f | Length in FFM02U | Length in FFM02L | Length in FFM01 z > −200 m | Length in FFM01 −200 m > z > −400 m | Length outside lens z > −30 m | Length outside lens −30 m > z > −200 m | Length outside lens −200 m > z > −400 m | % with orientation data |
|---|---|---|---|---|---|---|---|---|---|---|
| KFM01A | 30.5 m – 1 001.5 m | PFL from 105.3 m | 33.5 m | 173.4 m | 34.8 m | 199.3 m | Not in domain | Not in domain | Not in domain | 97.30 % |
| KFM01B | 15.7 m – 500.5 m | No PFL | 33.9 m | 190.7 m | 36.5 m | 192.5 m | Not in domain | Not in domain | Not in domain | 98.80 % |
| KFM01C | 12.3 m – 452.1 m | No PFL | 43.5 m | 183.4 m | 195.2 m | 183.1 m | Not in domain | Not in domain | Not in domain | 100.00 % |
| KFM01D | 91.7 m – 800.2 m | PFL from 106.1 m | 37.5 m | 115.7 m | 212.1 m | 259.3 m | Not in domain | Not in domain | Not in domain | 100.00 % |
| KFM02A | 14.7 m – 1 002.4 m | PFL from 102.1 m | Not in domain | Not in domain | Not in domain | Not in domain | 37.7 m | 170.4 m | 200.7 m | 93.70 % |
| KFM02B | 89.0 m – 573.9 m | PFL from 91.5 m | Not in domain | Not in domain | Not in domain | Not in domain | 38.3 m | 172.3 m | 202.9 m | 99.90 % |
| KFM03A | 102.3 m – 1 001.2 m | PFL from 106.4 m | Not in domain | Not in domain | Not in domain | Not in domain | 38.5 m | 170.4 m | 200.7 m | 98.60 % |
| KFM03B | 5.7 m – 101.5 m | No PFL | Not in domain | Not in domain | Not in domain | Not in domain | 38.8 m | 62.8 m | Not in domain | 97.50 % |
| KFM04A | 13.3 m – 1 001.4 m | PFL from 109.7 m | Not in domain | Not in domain | 9.8 m | 27.7 m | 44.7 m | 183.4 m | 209.7 m | 100.00 % |
| KFM04B | No fracture log | No PFL | Not in domain | Not in domain | Not in domain | Not in domain | 45.0 m | 55.6 m | Not in domain | No fracture log |
| KFM05A | 102.3 m – 1 002.7 m | PFL from 108.8 m | 41.3 m | 195.6 m | 142.9 m | 239.3 m | Not in domain | Not in domain | Not in domain | 98.10 % |
| KFM06A | 13.8 m – 1 000.6 m | PFL from 102.2 m | 39.5 m | 97.5 m | 99.0 m | 236.7 m | Not in domain | Not in domain | Not in domain | 98.70 % |
| KFM06B | 6.5 m – 100.3 m | No PFL | 34.5 m | 65.8 m | Not in domain | Not in domain | Not in domain | Not in domain | Not in domain | 98.00 % |
| KFM06C | 102.1 m – 1 000.9 m | No PFL | 39.6 m | 101.5 m | 99.8 m | 249.8 m | Not in domain | Not in domain | Not in domain | 100.00 % |
| KFM07A | 101.8 m – 1 002.1 m | PFL from 110.7 m | 39.0 m | 94.1 m | 102.8 m | 237.3 m | Not in domain | Not in domain | Not in domain | 99.90 % |
| KFM07B | 5.3 m – 298.9 m | No PFL | 41.0 m | 148.0 m | 63.1 m | 46.7 m | Not in domain | Not in domain | Not in domain | 0.00 % |
| KFM07C | 86.0 m – 500.3 m | PFL from 98.6 m | 33.7 m | 90.2 m | 80.8 m | 201.1 m | Not in domain | Not in domain | Not in domain | 62.10 % |
| KFM08A | 103.4 m – 1 001.2 m | PFL from 107.6 m | 37.6 m | 13.2 m | 188.2 m | 249.1 m | Not in domain | Not in domain | Not in domain | 100.00 % |
| KFM08B | 6.1 m – 200.5 m | No PFL | 38.1 m | 13.3 m | 149.2 m | Not in domain | Not in domain | Not in domain | Not in domain | 100.00 % |
| KFM08C | 102.3 m – 951.1 m | PFL from 102.3 m | 37.7 m | 13.2 m | 185.3 m | 240.2 m | Not in domain | Not in domain | Not in domain | 100.00 % |
| KFM08D | 61.3 m – 942.3 m | PFL from 75.7 m | 39.9 m | 20.5 m | 189.6 m | 246.2 m | Not in domain | Not in domain | Not in domain | 99.50 % |
| KFM09A | 7.8 m – 799.7 m | No PFL | 40.3 m | 84.8 m | 117.5 m | 4.0 m | Not in domain | Not in domain | 245.2 m | 0.00 % |
| KFM09B | 9.3 m – 616.5 m | No PFL | 42.0 m | 83.7 m | 126.9 m | 261.6 m | Not in domain | Not in domain | Not in domain | 0.00 % |

| idcode | Fracture mapped interval | PFL-f | Length in FFM02U | Length in FFM02L | Length in FFM01 z > −200 m | Length in FFM01 −200 m > z > −400 m | Length outside lens z > −30 m | Length outside lens −30 m > z > −200 m | Length outside lens −200 m > z > −400 m | % with orientation data |
|---|---|---|---|---|---|---|---|---|---|---|
| KFM09C | No fracture log | No PFL | 9.1 m | Not in domain | Not in domain | Not in domain | Not in domain | Not in domain | Not in domain | No fracture log |
| KFM10A | 62.7 m – 500.2 m | PFL from 70.8 m | Not in domain | Not in domain | 81.0 m | 23.0 m | 45.6 m | 234.5 m | 197.2 m | 99.80 % |
| KFM11A | 71.6 m – 851.2 m | PFL from 73.8 m | Not in domain | Not in domain | Not in domain | Not in domain | 37.8 m | 192.4 m | 233.3 m | 0.00 % |
| KFM12A | 60.3 m – 601.0 m | No PFL | Not in domain | Not in domain | Not in domain | Not in domain | 47.1 m | 197.1 m | 234.8 m | 99.00 % |
| KFM13 | 8.3 m – 150.2 m | No PFL | 37.8 m | 14.4 m | 98.0 m | Not in domain | Not in domain | Not in domain | Not in domain | 81.60 % |
| KFM14 | 6.7 m – 60.2 m | PFL from 7.8 m | 32.2 m | 27.9 m | Not in domain | Not in domain | Not in domain | Not in domain | Not in domain | 73.80 % |
| KFM15 | 7.6 m – 62.3 m | PFL from 9.9 m | 33.8 m | 28.5 m | Not in domain | Not in domain | Not in domain | Not in domain | Not in domain | 81.50 % |
| KFM16 | 4.4 m – 60.4 m | PFL from 7.3 m | 36.7 m | 23.6 m | Not in domain | Not in domain | Not in domain | Not in domain | Not in domain | 86.10 % |
| KFM17 | 6.3 m – 60.5 m | No PFL | 33.9 m | 26.5 m | Not in domain | Not in domain | Not in domain | Not in domain | Not in domain | 89.00 % |
| KFM18 | 9.0 m – 60.5 m | No PFL | 33.7 m | 26.8 m | Not in domain | Not in domain | Not in domain | Not in domain | Not in domain | 82.10 % |
| KFM19 | 7.3 m – 102.4 m | No PFL | 36.3 m | 66.0 m | Not in domain | Not in domain | Not in domain | Not in domain | Not in domain | 84.80 % |
| KFM20 | 2.5 m – 60.5 m | PFL from 6.0 m | 33.1 m | 27.4 m | Not in domain | Not in domain | Not in domain | Not in domain | Not in domain | 86.30 % |
| KFM21 | 6.0 m – 101.1 m | PFL from 6.8 m | 34.7 m | 66.3 m | Not in domain | Not in domain | Not in domain | Not in domain | Not in domain | 81.30 % |
| KFM22 | 8.7 m – 60.3 m | PFL from 8.7 m | 33.0 m | 27.2 m | Not in domain | Not in domain | Not in domain | Not in domain | Not in domain | 73.00 % |
| KFM23 | 3.5 m – 100.6 m | PFL from 5.0 m | 33.9 m | 66.7 m | Not in domain | Not in domain | Not in domain | Not in domain | Not in domain | 86.30 % |
| KFM24 | 39.5 m – 550.2 m | PFL from 48.6 m | 31.4 m | 11.2 m | 159.9 m | 201.6 m | Not in domain | Not in domain | Not in domain | 100.00 % |
| KFM90A | No fracture log | No PFL | 24.2 m | Not in domain | Not in domain | Not in domain | Not in domain | Not in domain | Not in domain | No fracture log |
| KFM90B | 2.9 m – 18.2 m | No PFL | 18.2 m | Not in domain | Not in domain | Not in domain | Not in domain | Not in domain | Not in domain | 0.00 % |
| KFM90C | 1.9 m – 20.0 m | No PFL | 20.0 m | Not in domain | Not in domain | Not in domain | Not in domain | Not in domain | Not in domain | 0.00 % |
| KFM90D | 3.1 m – 20.4 m | No PFL | 20.4 m | Not in domain | Not in domain | Not in domain | Not in domain | Not in domain | Not in domain | 0.00 % |
| KFM90E | 1.8 m – 20.3 m | No PFL | 20.3 m | Not in domain | Not in domain | Not in domain | Not in domain | Not in domain | Not in domain | 0.00 % |
| KFM90F | 2.3 m – 20.1 m | No PFL | 20.1 m | Not in domain | Not in domain | Not in domain | Not in domain | Not in domain | Not in domain | 0.00 % |

**Table 2-2. List of HFM boreholes indicating the borehole length of fracture mapped interval, the borehole length inside and outside the Forsmark Lens, and the % of the logged fractures with sufficient orientation data to define a fracture set.**

| idcode | Fracture mapped interval | Length in FFM02U | Length in FFM02L | Length in FFM01 z > −200 m | Length in FFM01 −200 m > z > −400 m | Length outside lens z > −30 | Length outside lens −30 m > z > −200 m | Length outside lens −200 m > z > −400 m | % with orientation data |
|---|---|---|---|---|---|---|---|---|---|
| HFM01 | 32.8 m – 200.2 m | 21.7 m | 106.3 m | 178.5 m | Not in domain | Not in domain | Not in domain | Not in domain | 100.00 % |
| HFM02 | 25.6 m – 100.0 m | 10.0 m | 54.9 m | 35.0 m | Not in domain | Not in domain | Not in domain | Not in domain | 100.00 % |
| HFM03 | 13.8 m – 26.0 m | 10.6 m | Not in domain | 15.4 m | Not in domain | Not in domain | Not in domain | Not in domain | 0.00 % |
| HFM04 | 13.5 m – 221.7 m | Not in domain | Not in domain | Not in domain | Not in domain | 34.2 m | 172.7 m | 14.8 m | 100.00 % |
| HFM05 | 13.9 m – 200.1 m | Not in domain | Not in domain | Not in domain | Not in domain | 38.0 m | 162.1 m | Not in domain | 100.00 % |
| HFM06 | 12.9 m – 110.7 m | Not in domain | Not in domain | Not in domain | Not in domain | 37.0 m | 73.7 m | Not in domain | 100.00 % |
| HFM07 | 19.2 m – 122.5 m | Not in domain | Not in domain | Not in domain | Not in domain | 36.1 m | 86.4 m | Not in domain | 99.60 % |
| HFM08 | 18.2 m – 143.5 m | Not in domain | Not in domain | Not in domain | Not in domain | 37.4 m | 106.1 m | Not in domain | 100.00 % |
| HFM09 | 17.2 m – 50.3 m | Not in domain | Not in domain | 20.4 m | Not in domain | 17.6 m | 12.2 m | Not in domain | 100.00 % |
| HFM10 | 11.9 m – 150.0 m | Not in domain | Not in domain | Not in domain | Not in domain | 37.4 m | 112.6 m | Not in domain | 100.00 % |
| HFM11 | 13.1 m – 182.4 m | Not in domain | Not in domain | Not in domain | Not in domain | 50.6 m | 131.8 m | Not in domain | 99.80 % |
| HFM12 | 15.5 m – 209.6 m | Not in domain | Not in domain | Not in domain | Not in domain | 49.7 m | 159.8 m | Not in domain | 100.00 % |
| HFM13 | 15.6 m – 175.6 m | Not in domain | Not in domain | Not in domain | Not in domain | 41.3 m | 134.3 m | Not in domain | 100.00 % |
| HFM14 | 3.8 m – 150.5 m | 34.7 m | 111.5 m | 37.5 m | Not in domain | 4.3 m | Not in domain | Not in domain | 100.00 % |
| HFM14B | No fracture log | 1.7 m | Not in domain | Not in domain | Not in domain | 2.3 m | Not in domain | Not in domain | No fracture log |
| HFM15 | 6.6 m – 99.5 m | 43.3 m | 51.0 m | Not in domain | Not in domain | 5.1 m | Not in domain | Not in domain | 100.00 % |
| HFM16 | 12.1 m – 132.5 m | 33.5 m | 93.8 m | 5.2 m | Not in domain | Not in domain | Not in domain | Not in domain | 100.00 % |
| HFM17 | 8.7 m – 210.7 m | Not in domain | Not in domain | Not in domain | Not in domain | 34.1 m | 172.8 m | 3.8 m | 100.00 % |
| HFM18 | 9.9 m – 180.7 m | Not in domain | Not in domain | Not in domain | Not in domain | 41.6 m | 139.1 m | Not in domain | 100.00 % |
| HFM19 | 11.9 m – 185.2 m | Not in domain | Not in domain | 24.4 m | Not in domain | 40.1 m | 120.7 m | Not in domain | 100.00 % |
| HFM20 | 12.2 m – 301.0 m | 33.3 m | 47.6 m | 122.5 m | 97.6 m | Not in domain | Not in domain | Not in domain | 100.00 % |
| HFM21 | 12.6 m – 202.0 m | 40.6 m | 125.9 m | 35.5 m | Not in domain | Not in domain | Not in domain | Not in domain | 100.00 % |

| idcode | Fracture mapped interval | Length in FFM02U | Length in FFM02L | Length in FFM01 z > −200 m | Length in FFM01 −200 m > z > −400 m | Length outside lens z > −30 | Length outside lens −30 m > z > −200 m | Length outside lens −200 m > z > −400 m | % with orientation data |
|---|---|---|---|---|---|---|---|---|---|
| HFM22 | 12.1 m – 222.0 m | 37.7 m | 27.4 m | 156.9 m | Not in domain | Not in domain | Not in domain | Not in domain | 100.00 % |
| HFM23 | 20.9 m – 211.5 m | 42.3 m | 36.4 m | Not in domain | Not in domain | Not in domain | 132.8 m | Not in domain | 0.00 % |
| HFM24 | 18.1 m – 151.4 m | Not in domain | Not in domain | 100.6 m | Not in domain | 14.9 m | 35.8 m | Not in domain | 0.00 % |
| HFM25 | 9.8 m – 187.5 m | Not in domain | Not in domain | 46.4 m | Not in domain | 40.9 m | 100.2 m | Not in domain | 0.00 % |
| HFM26 | 12.5 m – 202.7 m | Not in domain | Not in domain | Not in domain | Not in domain | 41.9 m | 160.8 m | Not in domain | 100.00 % |
| HFM27 | 12.6 m – 127.5 m | 7.0 m | 86.6 m | 33.9 m | Not in domain | Not in domain | Not in domain | Not in domain | 0.00 % |
| HFM28 | 12.4 m – 151.2 m | 34.7 m | 72.2 m | 44.4 m | Not in domain | Not in domain | Not in domain | Not in domain | 100.00 % |
| HFM29 | 9.2 m – 199.7 m | Not in domain | Not in domain | Not in domain | Not in domain | 40.2 m | 159.5 m | Not in domain | 0.00 % |
| HFM30 | 18.9 m – 200.8 m | Not in domain | Not in domain | Not in domain | Not in domain | 40.3 m | 160.5 m | Not in domain | 100.00 % |
| HFM31 | 9.1 m – 200.8 m | Not in domain | Not in domain | Not in domain | Not in domain | 38.9 m | 161.8 m | Not in domain | 100.00 % |
| HFM32 | 6.0 m – 202.7 m | Not in domain | Not in domain | Not in domain | Not in domain | 31.3 m | 171.4 m | Not in domain | 0.00 % |
| HFM33 | 13.3 m – 140.2 m | Not in domain | Not in domain | Not in domain | Not in domain | 38.8 m | 101.4 m | Not in domain | 100.00 % |
| HFM34 | 12.8 m – 200.8 m | Not in domain | Not in domain | Not in domain | Not in domain | 38.1 m | 162.6 m | Not in domain | 100.00 % |
| HFM35 | 12.3 m – 200.8 m | Not in domain | Not in domain | Not in domain | Not in domain | 38.5 m | 162.3 m | Not in domain | 100.00 % |
| HFM36 | 12.2 m – 152.6 m | Not in domain | Not in domain | Not in domain | Not in domain | 46.6 m | 106.0 m | Not in domain | 0.00 % |
| HFM37 | 9.5 m – 191.8 m | Not in domain | Not in domain | Not in domain | Not in domain | 47.3 m | 144.4 m | Not in domain | 0.00 % |
| HFM38 | 10.0 m – 200.8 m | 40.4 m | 13.6 m | 146.7 m | Not in domain | Not in domain | Not in domain | Not in domain | 100.00 % |
| HFM39 | 6.8 m – 151.2 m | 34.6 m | 12.3 m | 104.3 m | Not in domain | Not in domain | Not in domain | Not in domain | 100.00 % |
| HFM40 | 7.8 m – 101.7 m | 32.7 m | 14.8 m | 54.3 m | Not in domain | Not in domain | Not in domain | Not in domain | 100.00 % |
| HFM41 | 6.8 m – 101.5 m | 33.8 m | 12.0 m | 55.7 m | Not in domain | Not in domain | Not in domain | Not in domain | 100.00 % |
| HFM42 | No fracture log | 34.2 m | 83.5 m | 77.6 m | Not in domain | Not in domain | Not in domain | Not in domain | No fracture log |
| HFM43 | No fracture log | 34.4 m | 51.0 m | 114.6 m | Not in domain | Not in domain | Not in domain | Not in domain | No fracture log |

**Table 2-3. Percentages of each rock type by fracture domain at different elevations.**

| | FFM01 z > −200 m | FFM01 −200 m > z > −400 m | FFM02L | FFM02U | Outside lens z > −30 m | Outside lens −30 m > z > −200 m | Outside lens −200 m > z > −400 m |
|---|---|---|---|---|---|---|---|
| **Amphibolite** | 2.6 | 1.9 | 2.7 | 2.3 | 5.1 | 4.0 | 8.7 |
| **Calc-silicate rock (skarn)** | 0.3 | | | | | 0.3 | 0.7 |
| **Cataclasite** | | | | | | 2.6 | |
| **Diorite, quartz diorite and gabbro, metamorphic** | 0.4 | 0.2 | | | | 0.8 | 1.5 |
| **Felsic to intermediate volcanic rock, metamorphic** | 0.4 | | 0.1 | | 26.3 | 11.9 | 9.2 |
| **Granite to granodiorite, metamorphic, medium-grained** | 85.8 | 85.1 | 84.8 | 89.1 | 42.9 | 43.8 | 49.4 |
| **Granite, fine- to medium-grained** | 0.7 | 0.7 | 0.7 | | | 6.1 | 1.9 |
| **Granite, granodiorite and tonalite, metamorphic, fine- to medium-grained** | 1.5 | 5.8 | 4.0 | 1.0 | 1.3 | 11.8 | 3.2 |
| **Granite, metamorphic, aplitic** | 2.5 | 0.2 | 0.1 | | | 0.6 | 0.3 |
| **Granodiorite, metamorphic** | | | 0.1 | | 9.5 | 7.3 | 20.4 |
| **Pegmatite, pegmatitic granite** | 5.9 | 6.2 | 7.6 | 7.6 | 14.9 | 8.7 | 4.5 |
| **Tonalite to granodiorite, metamorphic** | | | | | | 2.2 | 0.2 |

In order to make integrated interpretations of the borehole data, a composite log for each hole has been created to examine possible correlations and patterns. Some chosen examples of this are shown in Figure 2-3 to Figure 2-5. The columns show:

- Lithology.
- Fracture Dip plotted as “tadpoles” coloured by alteration with the head circled if aperture is large and crush zones superimposed as horizontal lines.
- P10 showing a moving average Terzaghi (Terzaghi 1965) weighted linear fracture intensity for all open fractures and gently dipping open fractures with single-hole interpreted possible deformation zones superimposed.
- Structural dip of foliation and ductile/semi-ductile shear zones (from the “p_rock_occur” property in the SICADA database) to identify foliation parallel fracturing.
- P-wave velocity as a potential indicator of more extensive fractures where the velocity is lower.
- Transmissivity data from impeller logging, PSS double-packer injection, PFL-s or PFL-f logging.

There are 274 crush zones recorded in HFM/KFM holes, with the majority (141) occurring above an elevation of −100 m.

It can be noted that all single-hole intercepts with damage zone (DZ) type properties are classified as possible deformation zones (PDZ). It is when a PDZ intercept is modelled in 3D it that it is elevated to becoming a DZ. Major DZs are numbered and termed ZFMs. Only the ZFM DZs are included in the current modelling, as these are the ones for which surfaces are available.

A key part of the methodology is to analyse fracture statistics outside deformation zones separately from inside. That is, the ZFM deformation zones are treated as separate fracture domains, and thereby avoid averaging fractured zones with the intervening good rock. PDZ remain part of the rock mass, FFM.

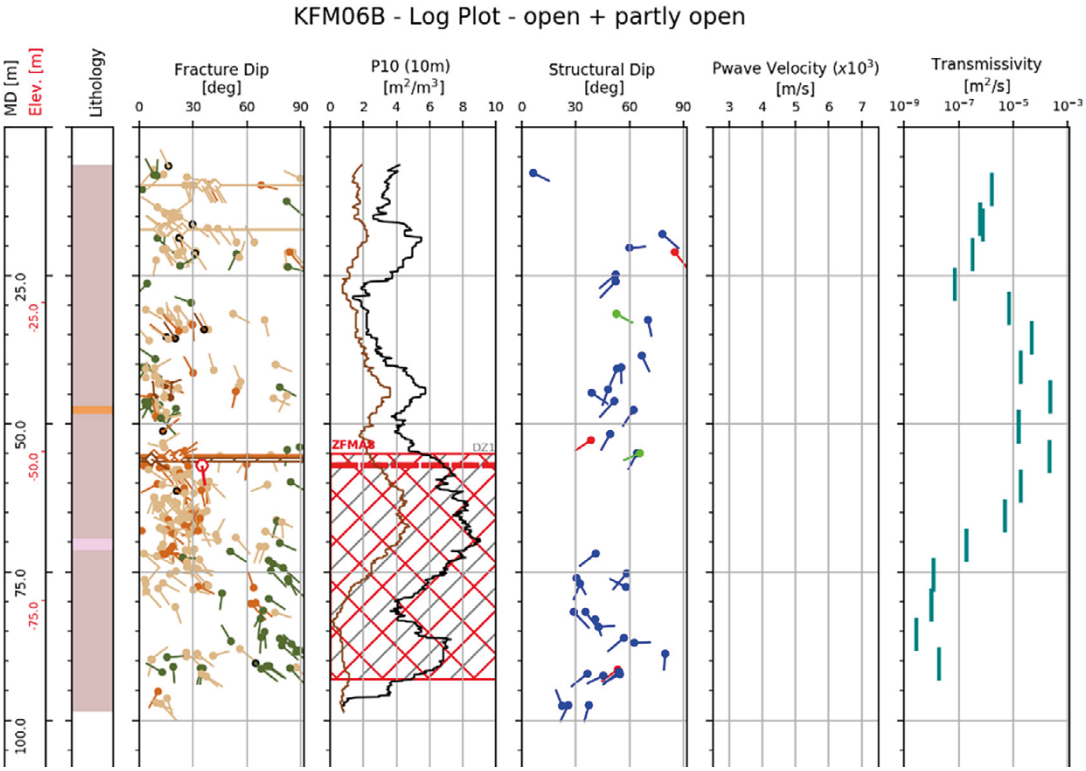


***Figure 2-3.*** *Borehole log of KFM06B, showing a SHI interpreted interval (ZFM06B). PSS 5-m double-packer hydraulic injection testing is available for this hole.*

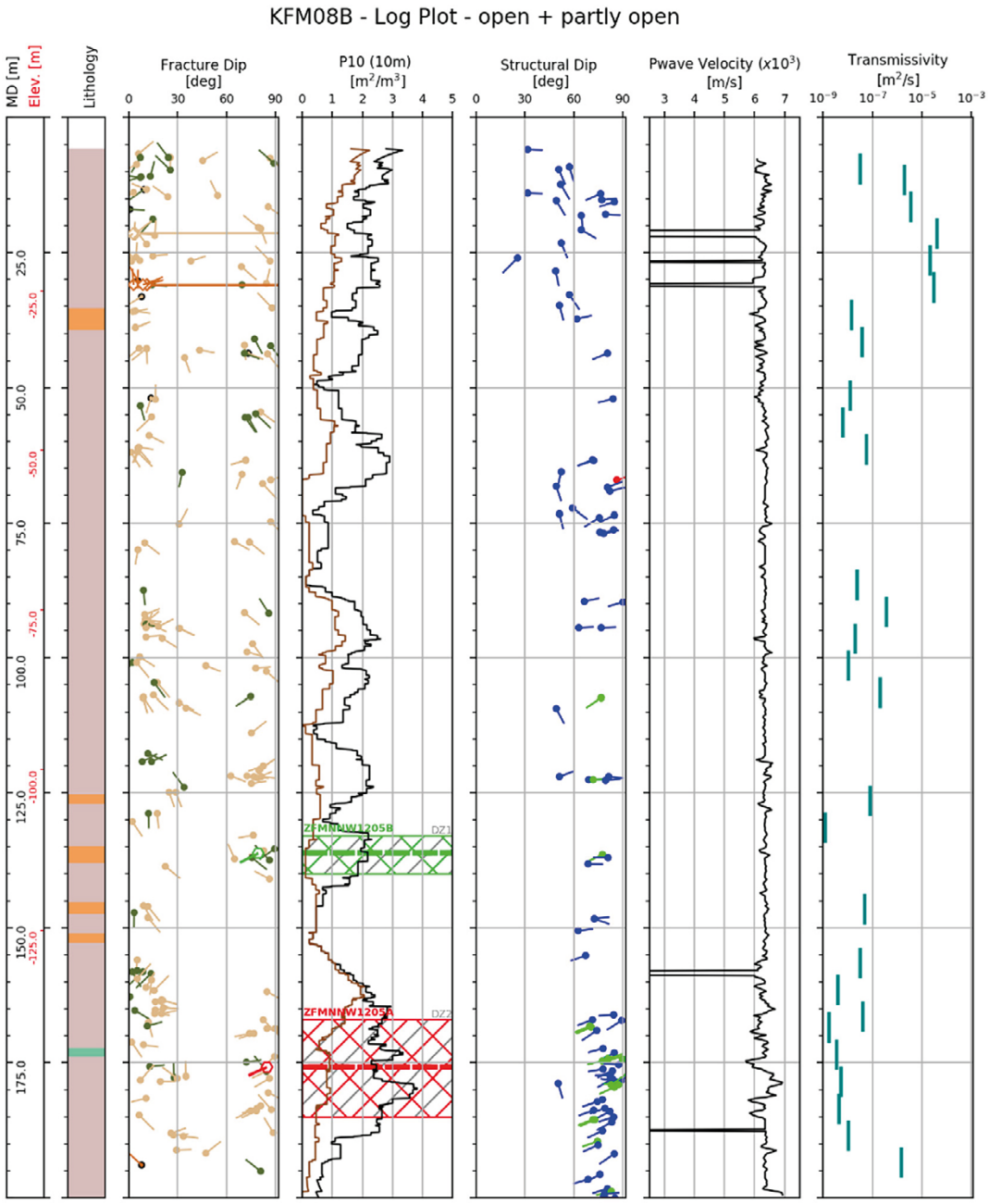


***Figure 2-4.*** *Borehole log of KFM08B, showing DZ intervals (ZFMNNW1205B and ZFMNNW1205A). PSS double-packer hydraulic injection is available for this hole.*

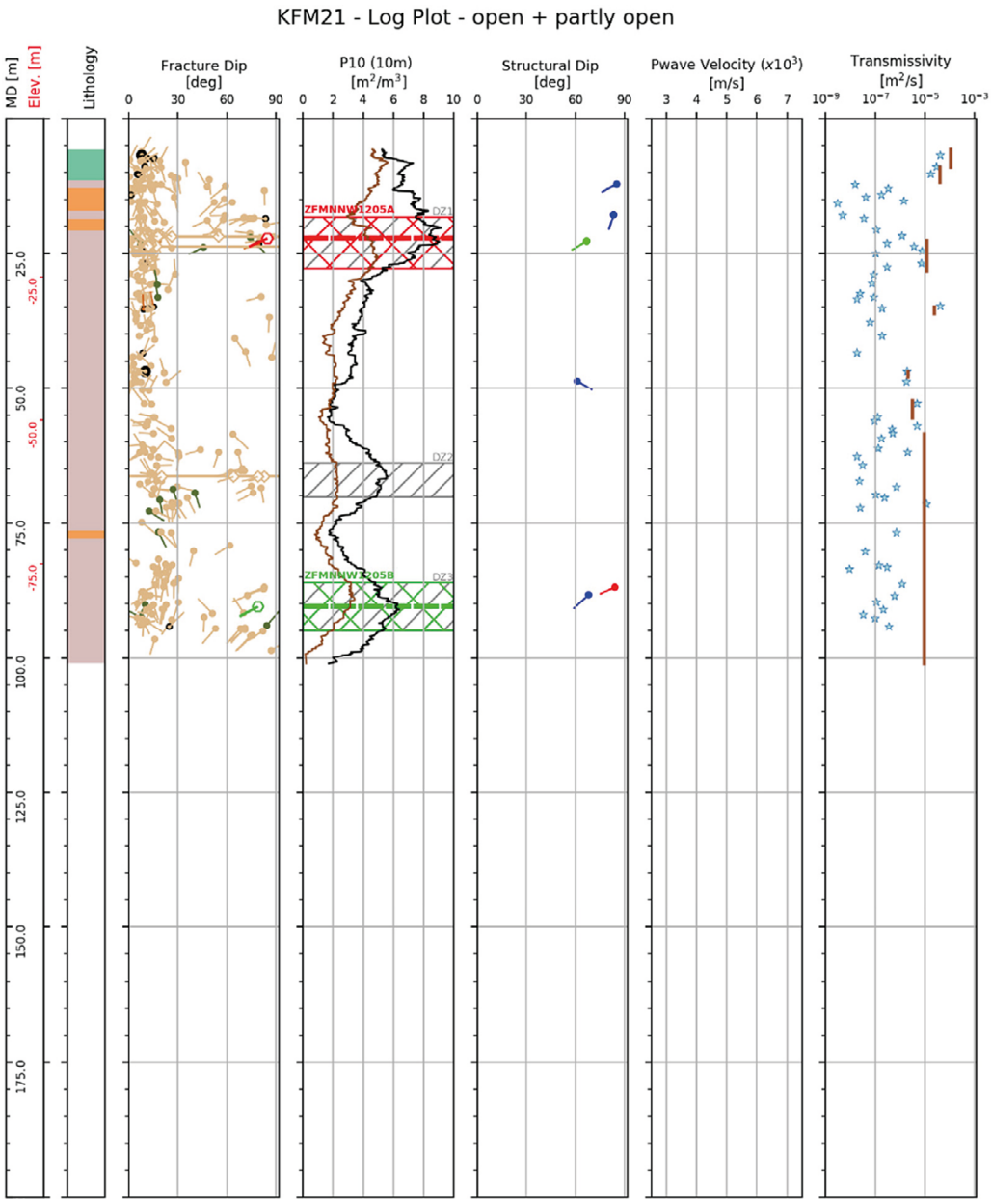


***Figure 2-5.*** *Borehole log of KFM21, showing DZ intervals (ZFMNNW1205B, ZFMNNW1205A and one zone not modelled). PFL-f hydraulic testing and impeller logging is available for this hole.*

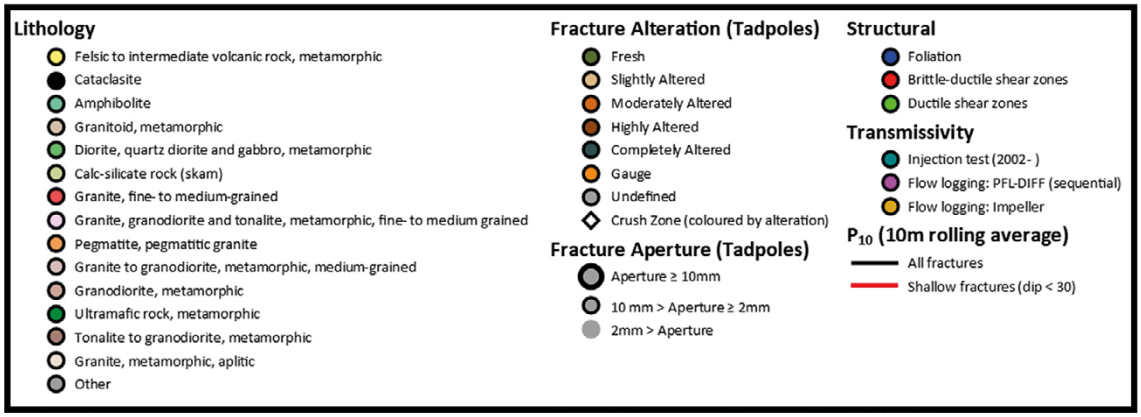


***Figure 2-6.*** *Legend used for the composite log plots shown in above.*

## 2.3 Geological models

The 3D geological models included in the database are the rock domain (RFMxx) model, the fracture domain model (FFMxx) and the deformation zone model (ZFM/-xx/-xxxxxxx). The rock domain and fracture domain models have not been changed since SDM-Site. In the work reported here FFM02 is split into FFM02L above an elevation of −30 m and FFM02U below. The volume of each geological model is deterministically modelled but the properties may vary depending on location and direction.

A distinct layer in the upper 20 – 30 m of bedrock was noted already during mapping of the power plant channel inlet (Carlsson 1979) and later in the geological DFN modelling for SDM-Site (Fox et al. 2007). In this study, review of the composite logs suggested a consistently higher intensity of sub-horizontal fracturing in this layer, often with some crush zones and high aperture fractures. Bands of high intensity and crush zones are found below this elevation but are less frequent and sporadic between boreholes. The geological modelling team working in parallel with this study also reviewed the occurrence of water conducting and large aperture sub-horizontal fractures on a projected section, see Figure 2-8, and agreed on the suitability of this subdivision. All analyses presented in this report therefore report statistic divided between FFM02U and FFM02L, see Figure 2-9.

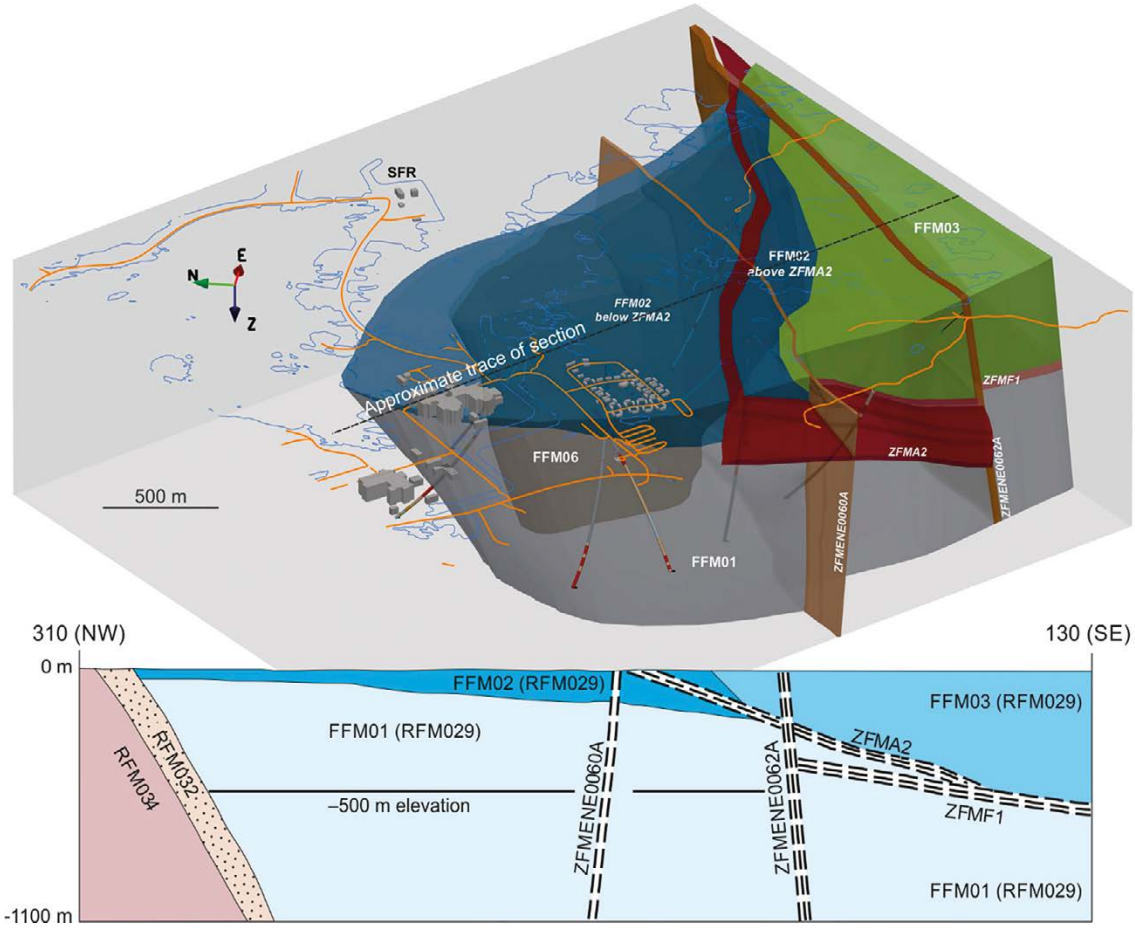


***Figure 2-7.*** *A) Facility-scale 3D geometric model for fracture domains FFM01, FFM02, FFM03 and FFM06 in the north–western part of the Forsmark tectonic lens, viewed towards the east–north–east; B) Simplified NW–SE trending profile showing the same fracture domains. Only high confidence deformation zones ZFMA2 (gently dipping), ZFMF1 (sub-horizontal), ZFMENE0060A (steeply dipping, longer than 3 000 m) and ZFMENE0062A (steeply dipping, longer than 3 000 m) are included in the images. Images and caption adapted from Olofsson et al. (2007).*

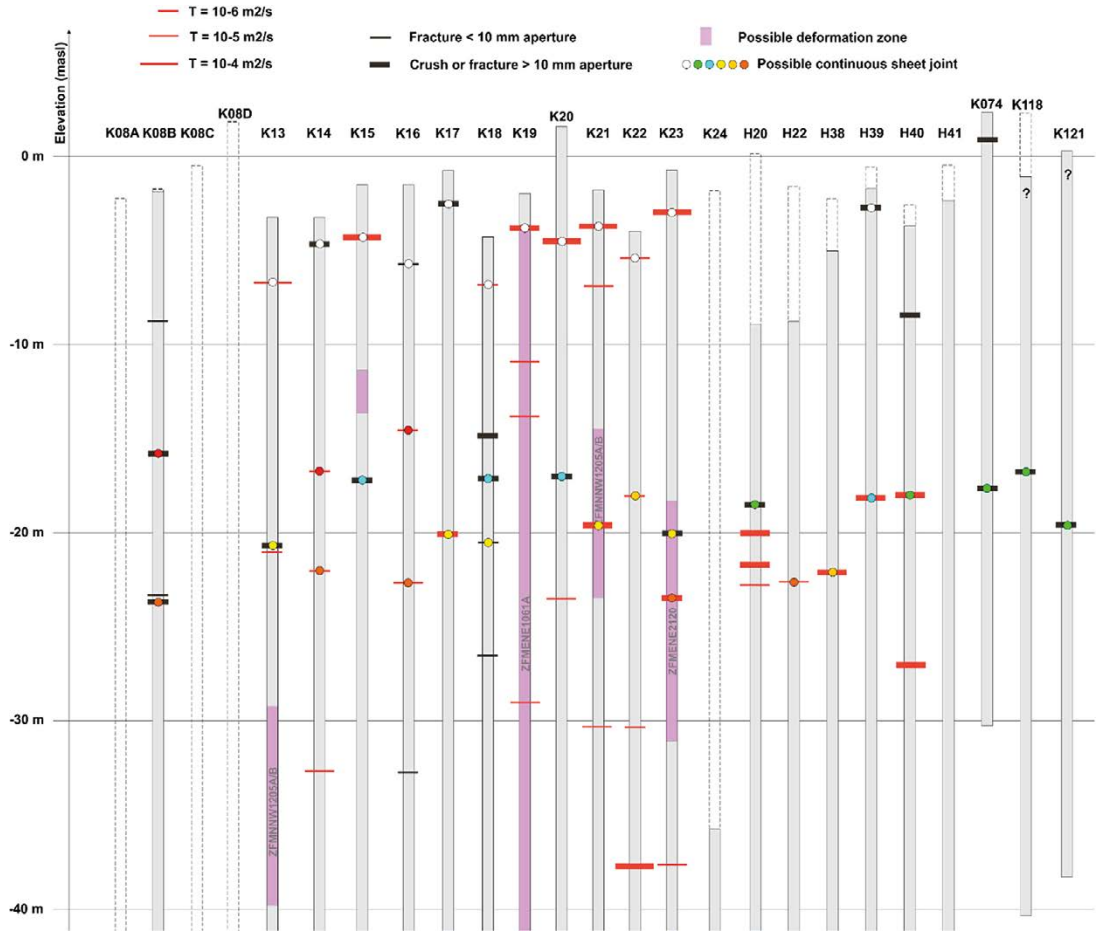


***Figure 2-8.*** *An illustration of borehole intersects with significant near-surface sub-horizontal structures in the array of relatively closely spaced shallow holes in the access area of the Forsmark tectonic lens (see Follin 2019 for details). The subset of structures shown are either crush zones (highly fractured, non-cohesive rock) or fractures of high transmissivity. Here, boreholes are projected on to a thick section, but spaced regularly.*

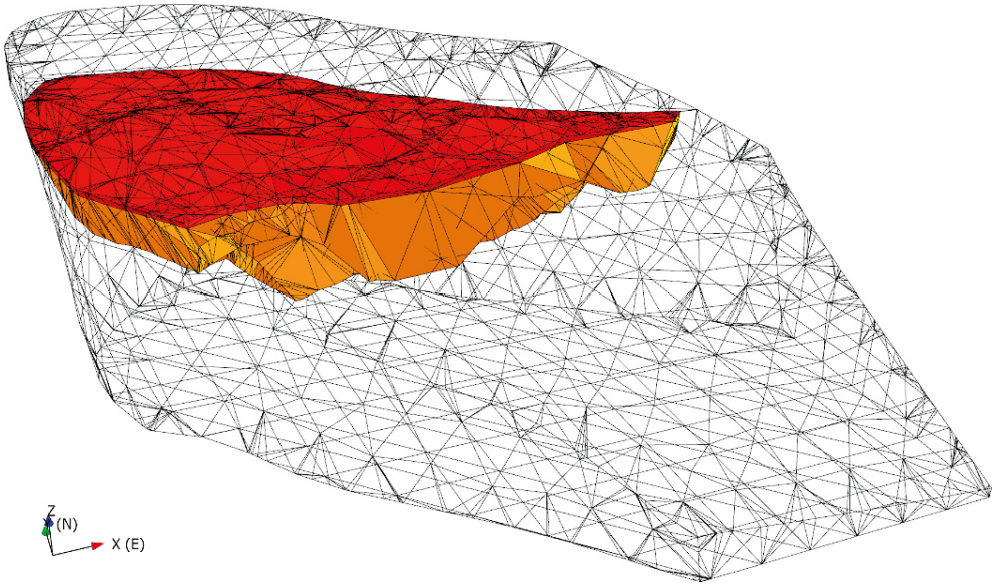


***Figure 2-9.*** *3D view of the different domains for which fractures were created; red is FFM02U, orange is FFM02L and transparent is the lens region (FFM01, FFM02, FFM06) extrapolated above ground and to 1 000 m depth. For scale and orientation, the surface trace of FFM02 is shown on Figure 2-1.*

The deformation zone model was updated by the geological modelling team using the new borehole data, which for reference is known as “DMS2018:2” (deterministically modelled structures version 2018:2). Here, the zones are modelled as mid planes through the central core of each structure with in-plane transmissivity and storativity represented as properties on each triangle discretising the zone. A fine triangulation is used to capture, e.g., modelled variations of transmissivity with depth as shown in Figure 2-10, see Subsection 4.1.1 for details.

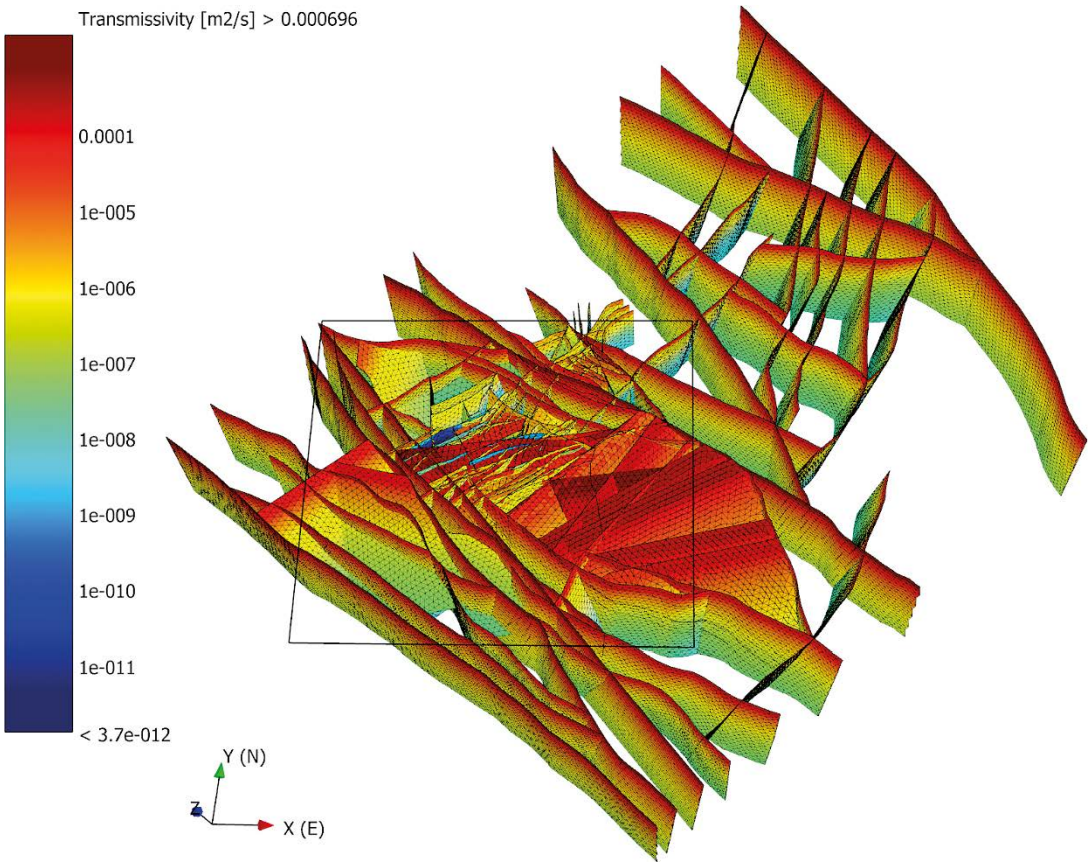


***Figure 2-10.*** *3D view of the ZFMs surfaces. The black box shows the outline of Figure 2-1.*

## 2.4 Single-hole hydraulic measurements

Single hole measurements of transmissivity have been performed using several hydraulic test procedures at Forsmark, including:

- Pumping tests (wire line and submersible pump); (transient).
- Flow logging – impeller; (steady flow).
- PFL-f – overlapping flow differencing; (steady flow).
- PFL-s – sequential flow differencing; (steady flow).
- Slug tests; (transient).
- Pulse tests; (transient).
- Injection tests; (transient).

The main procedure used here is PFL-f where measurements give a distribution of discrete specific capacities that can be linked to individual fractures and hence used to understand correlations between transmissivity and other fracture properties. PFL-s and impeller logging are also used to obtain total flows for borehole intervals where it is clear which fracture domain the flows can be associated to.

There are 765 PFL-f measurements in total that can be matched to discrete fractures. The number of PFL-f measurements in the intervals in the original delivery from SDM-Site are given in Table 2-4. There are no intervals in the top 50 m. The corresponding information for the second delivery for 2016 boreholes with PFL-f measurements in boreholes drilled in the access area is given in Table 2-5. These provide 7 holes with shallow data with 263 PFL-f measurements.

**Table 2-4. Summary of data from the original delivery of PFL-f. Adjusted secup is the corrected borehole depth for the top of the borehole intervals, while adjusted seclow is the equivalent depth of the bottom.**

| idcode | # of PFL | adjusted secup (m) | adjusted seclow (m) |
|---|---|---|---|
| KFM01A | 34 | 105.295 | 363.373 |
| KFM01D | 34 | 106.088 | 571.058 |
| KFM02A | 125 | 102.067 | 894.307 |
| KFM02B | 41 | 91.5 | 502.13 |
| KFM03A | 52 | 106.435 | 992.958 |
| KFM04A | 71 | 109.666 | 954.993 |
| KFM05A | 27 | 108.799 | 720.085 |
| KFM06A | 99 | 102.208 | 770.8 |
| KFM07A | 23 | 110.675 | 261.324 |
| KFM07C | 15 | 98.624 | 279.147 |
| KFM08A | 41 | 107.648 | 686.906 |
| KFM08C | 21 | 102.292 | 683.633 |
| KFM08D | 34 | 75.679 | 832.345 |
| KFM10A | 56 | 70.806 | 484.288 |
| KFM11A | 92 | 73.777 | 475.666 |

**Table 2-5. Second delivery of PFL-f measurements.**

| idcode | # of PFL | adjusted secup | adjusted seclow |
|---|---|---|---|
| KFM14 | 17 | 7.835 | 54.523 |
| KFM15 | 23 | 9.913 | 53.84 |
| KFM16 | 25 | 7.339 | 53.13 |
| KFM20 | 26 | 5.987 | 56.636 |
| KFM21 | 60 | 6.803 | 94.166 |
| KFM22 | 24 | 8.693 | 52.387 |
| KFM23 | 54 | 4.971 | 85.911 |
| KFM24 | 34 | 48.653 | 414.435 |

The latest PFL delivery required the transmissivity measurements to be matched to fractures using an automated method following the algorithm used in SDM-Site (Forssman et al. 2006, 2008):

- If the flow occurs inside a crush zone – assign the transmissivity to the crush zone;
- Else calculate the following and assign flow to the fracture with minimum value of depth offset:
- Depth offset between flow and crush zone *or* any Certain, Open or Partly Open fracture;
- Depth offset + 10 cm between flow and any Probable, Open or Partly Open fracture;
- Depth offset + 20 cm between flow and any other Open or Partly Open fracture (Confidence = Possible or Null); and
- Depth offset + 1 m between flow and any Sealed fracture.

This process ensured each PFL-f flow measurement was assigned to a unique fracture.

Because the PFL-f data is discrete it can be used to quantify both total flows in a domain, as well as distribution of flows for each orientation set. However, since measurements in the near surface are limited to only 7 boreholes, short interval impeller logging was used to augment analyses of differences in flow magnitudes between domains/depths. These measurements can be assigned to particular domains but not to individual fractures, so that they don't provide support for the transmissivity distributions of fractures. For example, HFM20, HFM21, HFM22, HFM38, HFM39, HFM40 provide magnitudes of total flows in FFM02L and FFM02U.

A collation of total transmissivities for holes in FFM02U using both PFL-f (orange) and impeller logging (blue) is shown in Figure 2-11. The 5-m injection test data could be used to augment these plots to give a few additional holes, such KFM06B. The upper figure is for holes inside the lens, the lower is for ones outside, including HFR holes north of the Singö deformation zone. Inside the lens the range varies between about $10^{-6}$ m$^2$/s and $3 \times 10^{-4}$ m$^2$/s. Many holes have a transmissivity of around $10^{-4}$ m$^2$/s in this domain. The numbers on top of the bars give an indication of the length of interval measured, although for some of the impeller logs, the numbers are just the length of interval which gave the most flow if all the flow was from one interval. Where there is both types of measurements, the impeller logging value can be higher than PFL-f, possibly due to some high flows exceeding the upper detection limit of PFL-f. The impeller logging value for KFM-15 is much higher than the PFL-f value because there is very high flow at the very top of the hole above where the PFL-f logging started. Where there is PFL-f data or impeller logging to identify the main flowing intervals, it is clear that the total flow results from 1 to 2 dominant flows.

Outside the lens, the range is similar, although some holes have transmissivity of nearly $10^{-3}$ m$^2$/s, toward SFR but south of the Singö deformation zone. The values for the HFR holes north of the Singö deformation zone are generally a bit lower. Together these results would suggest that relatively high near-surface flows are common throughout the area at least as far north as the Singö deformation zone, although the system is quite heterogeneous.

Figure 2-12 shows the equivalent plots for FFM02U and outside the lens between z = −30 m and z = −200 m. For FFM02U, transmissivities are also between$10^{-6}$ m$^2$/s and $3 \times 10^{-4}$ m$^2$/s but with perhaps more variability. This would imply that high transmissivity features also occur below z = −30 m, but at a lower intensity. The total transmissivity outside the lens is also similar magnitude, although this interval extends down to z = −200 m, while FFM02 rarely goes below z = −100 m. Therefore, the increased thickness compensates for any decrease in intensity of high transmissivity fractures with depth. The equivalent for FFM01 above z = −200 m is shown in Figure 2-13, which again has a similar transmissivity for this thicker interval.

The most dramatic change comes when looking at the total transmissivity in FFM01 below elevation −200 m in Figure 2-14 where the total transmissivity range falls to $10^{-8}$ to $10^{-5}$ m$^2$/s. Many holes have a total transmissivity below $10^{-7}$ m$^2$/s inside the lens, but above $10^{-6}$ m$^2$/s outside the lens. Possible reasons are examined in later chapters, but one important factor is the higher stress magnitudes inside the lens compared to Glamheden et al. (2007) and Hakala et al. (2019).

The PFL-f data and its linking to fractures demonstrates the relationship between flow and fracture orientation, revealing the anisotropy of the hydraulic system and the effects of anisotropy in the stress field. Figure 2-15 and Figure 2-16 show the distributions of transmissivity outside deformation

zones (the geological single hole interpretation of modelled deformation zones is used) by each of six global sets (SubH, NW, NS, NE, EW, ENE) for each domain. The very clear result is the flow is predominantly in sub-horizontal fractures in all domains. Flows in other sets are very sparse, with ENE being the secondary set for flow in FFM02, and a few sporadic flows in NW and EW sets. This would indicate a very anisotropic flow system outside deformation zones with strong horizontal flow but limited vertical flows (Follin et al. 2013).

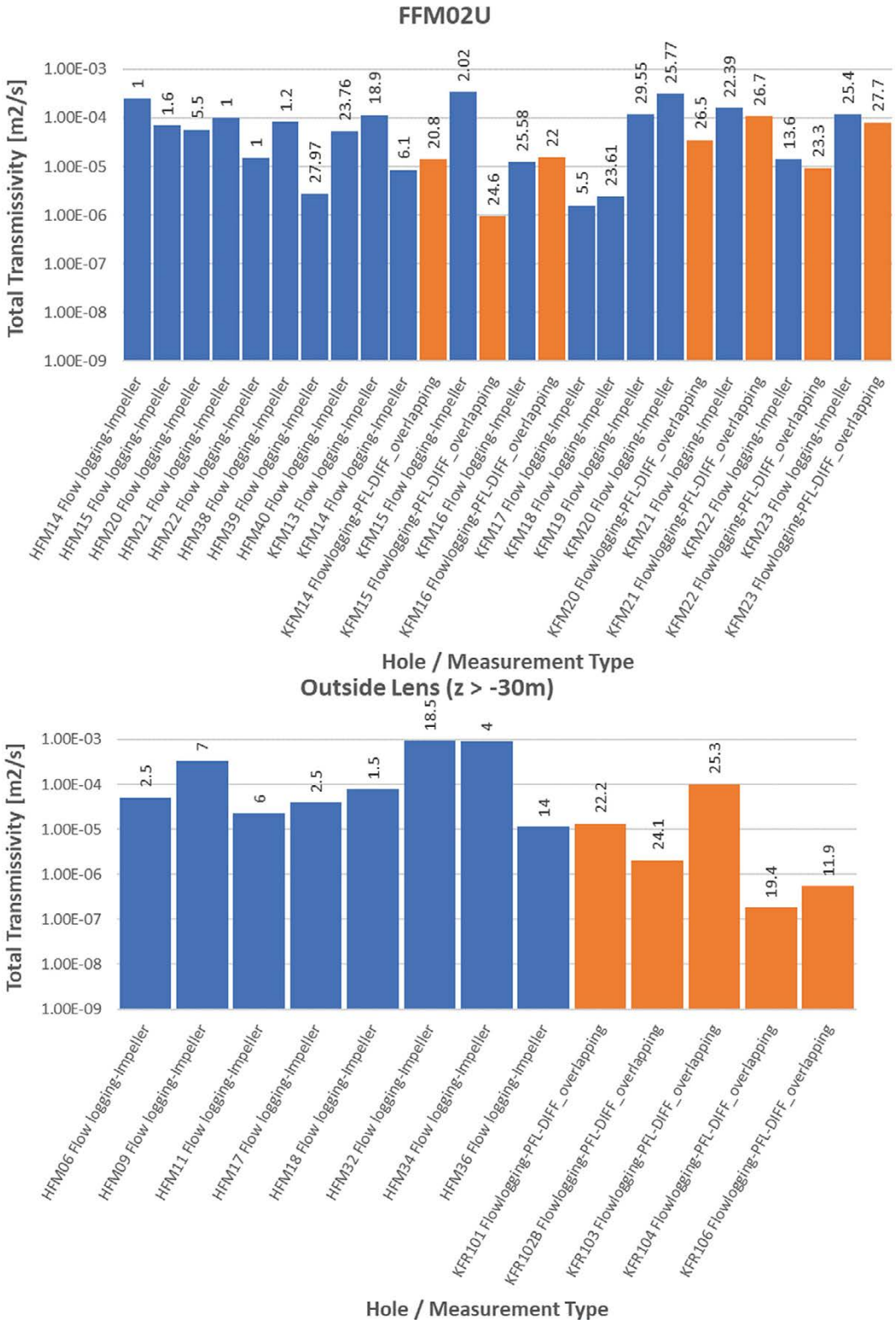


***Figure 2-11.*** *Total transmissivity, by drillhole, for FFM02U (top) and outside the lens, above z = −30 m (bottom).*

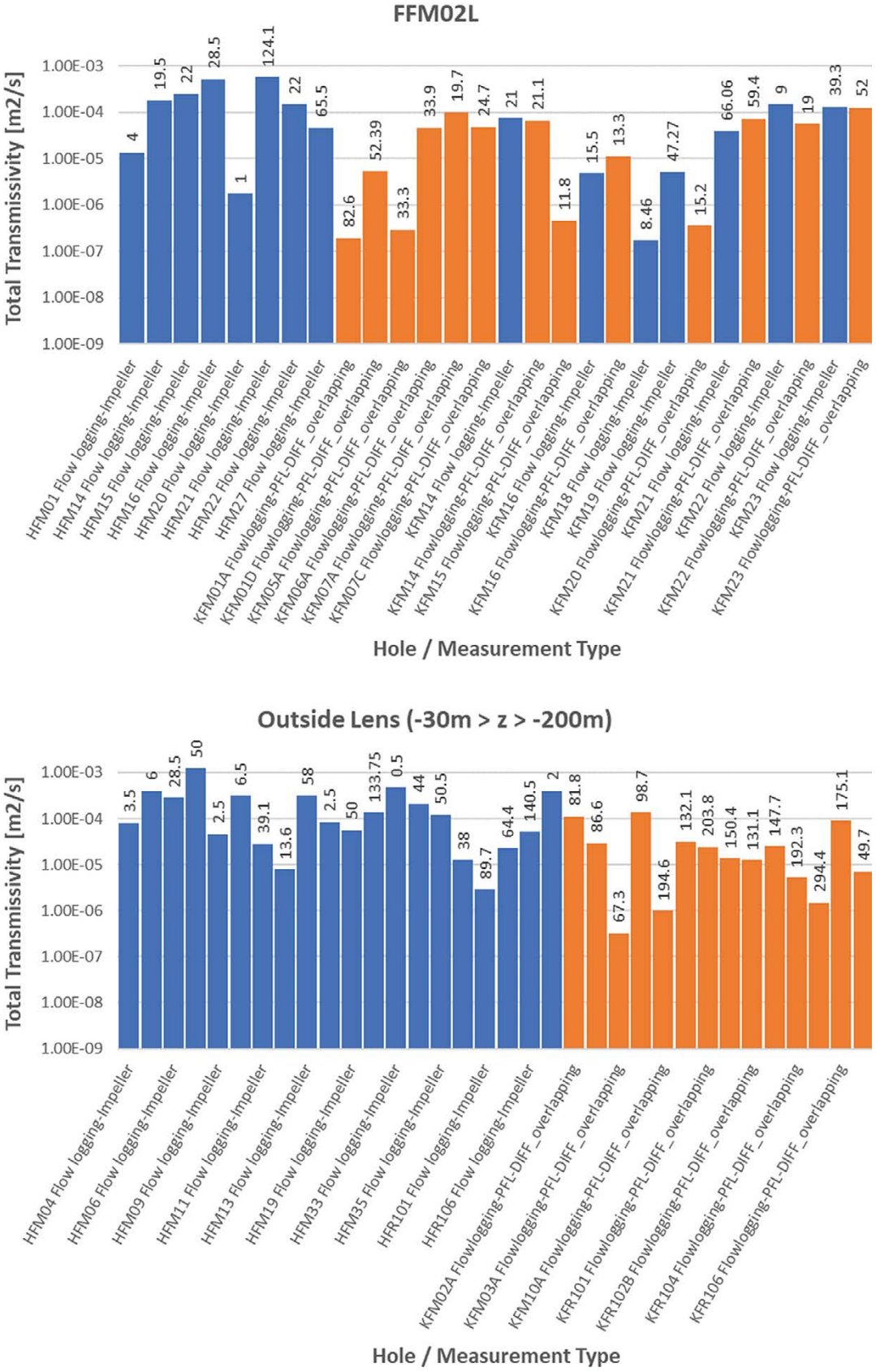


***Figure 2-12.*** *Total transmissivity, by drillhole, for FFM02L (top) and outside the lens between z = −30 m and z = −200 m (bottom).*

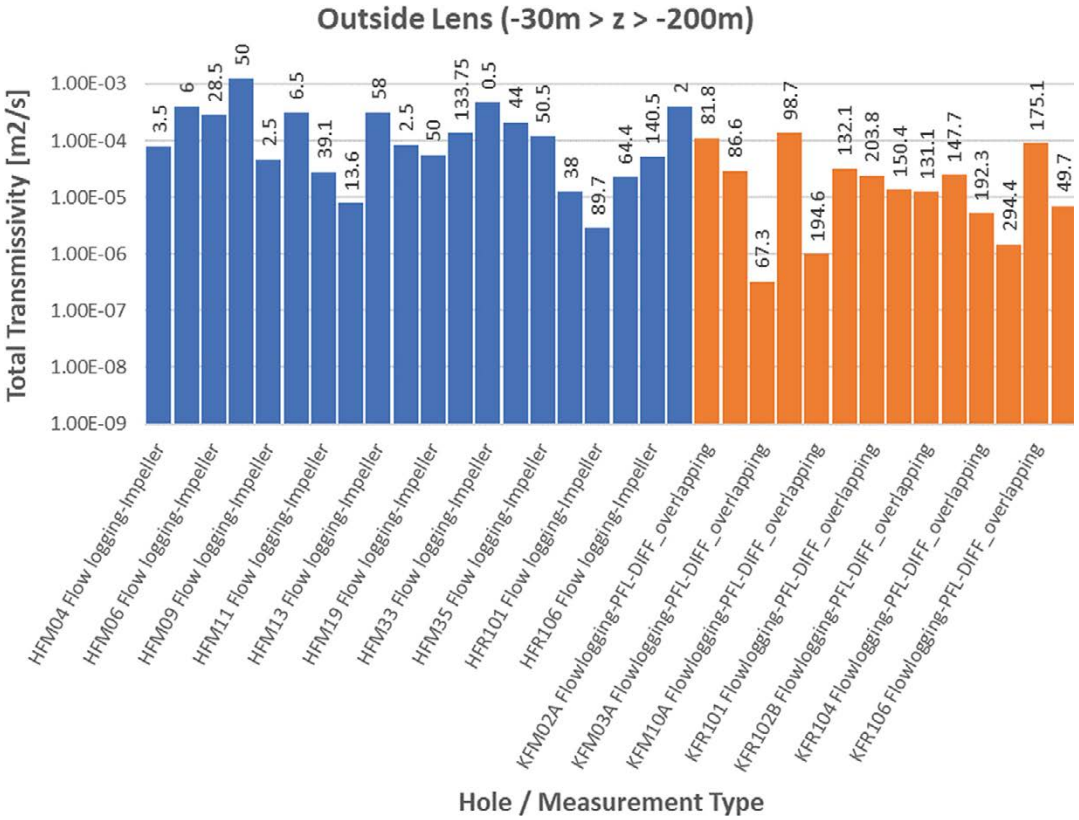


***Figure 2-13.*** *Total transmissivity, by drillhole, for FFM01 above and z = −200 m.*

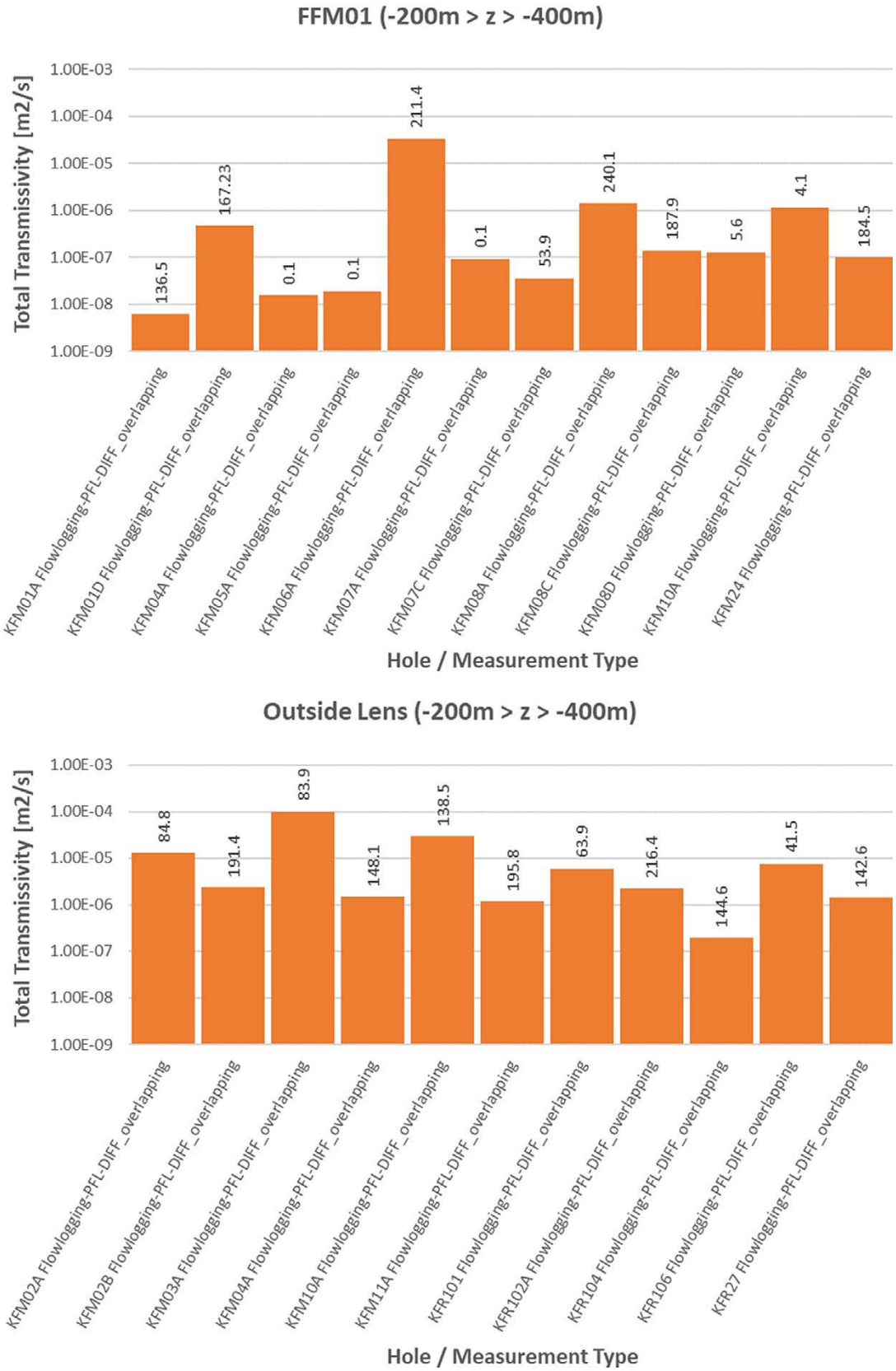


***Figure 2-14.*** *Total transmissivity, by drillhole, for FFM01 between z = −200 m and z = −400 m (top) and outside the lens, for the same elevations (bottom).*

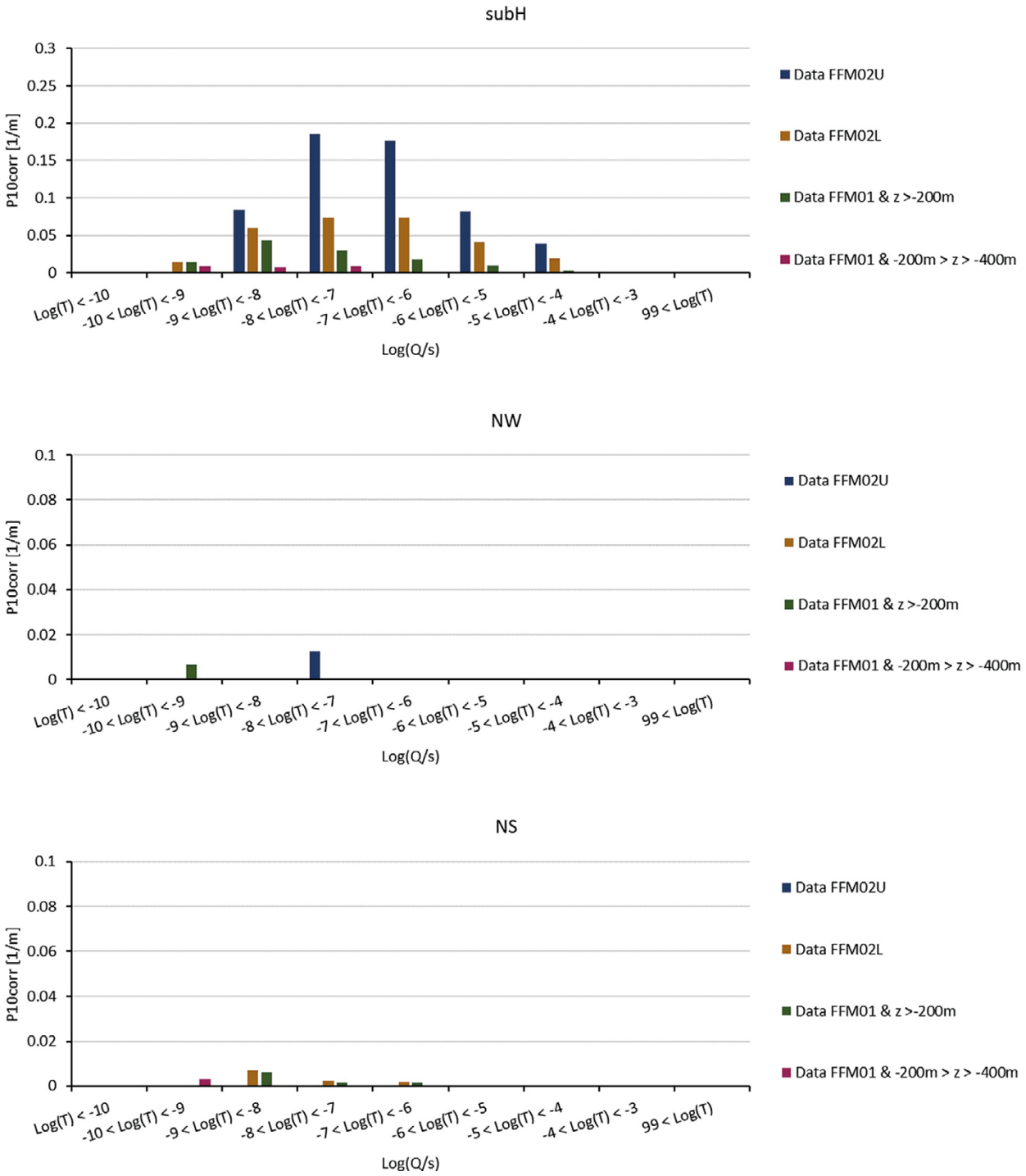


***Figure 2-15.*** *Histogram of PFL-f measurements in FFM02 and FFM01 outside deformation zones, for sub-horizontal, NW and NS fractures.*

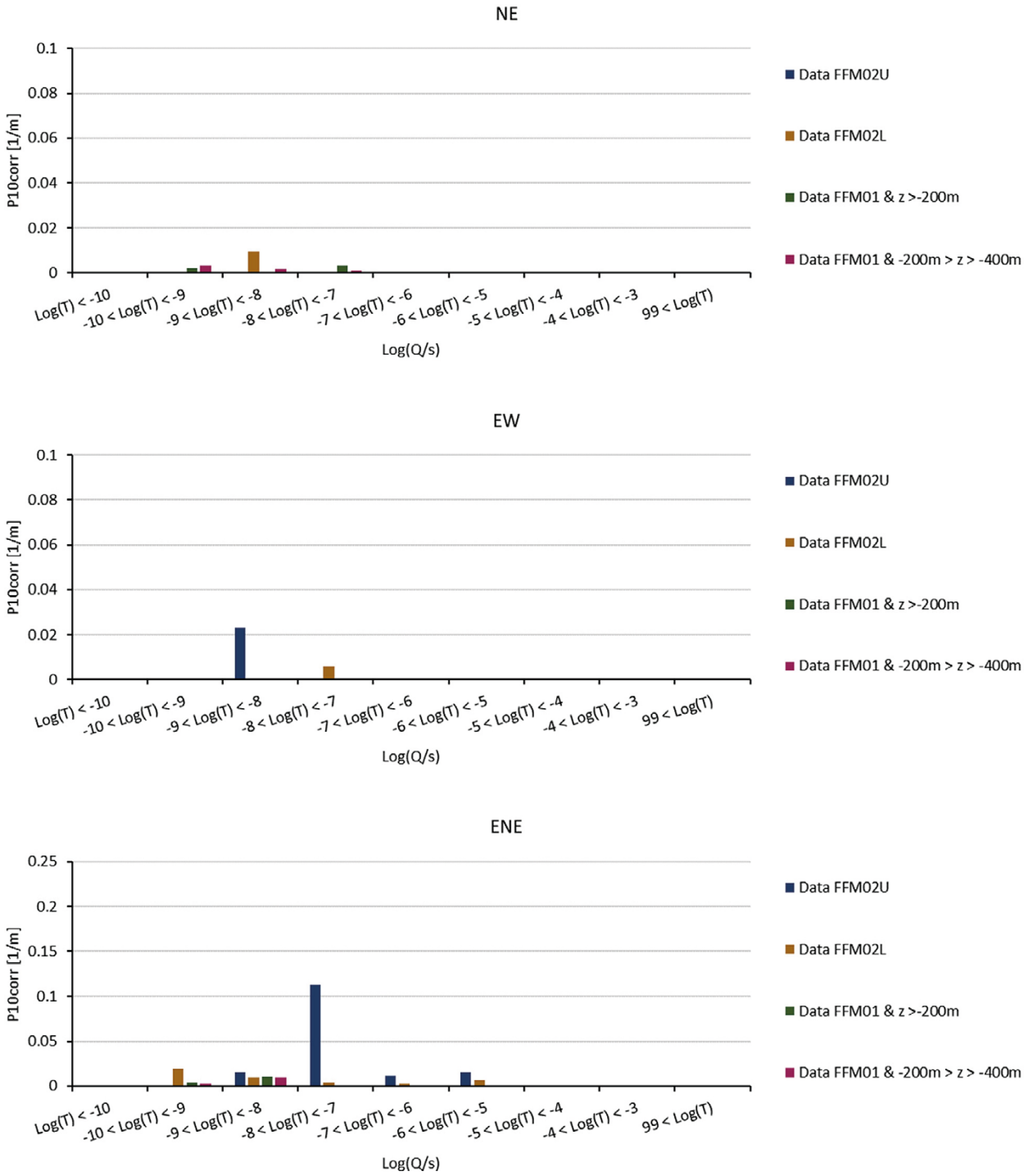


***Figure 2-16.*** *Histogram of PFL-f measurements in FFM02 and FFM01 outside deformation zones, for NE, EW and ENE fractures.*

The upper measurement limit for PFL-f tests is around a flow-rate of 300 L/h or order $10^{-4}$ $m^3/s$, implying a transmissivity $10^{-5}$ $m^2/s$ for a drawdown of 10 m in the pumped hole. The maximum measured specific capacities are around $10^{-4}$ $m^2/s$ and hence may be close to or exceeding the upper limit depending on how the tests were adapted for each hole. This might result in the highest specific capacities being under-estimated in the PFL-f tests. A way to examine the consequences of this is to compare specific measurements between PFL-f and impeller logging. Figure 2-17 provides an example from KFM22 where the Impeller logging has isolated four short intervals. Two of the transmissivities are very similar, while for the others (highest impeller logged values) the impeller logging gives values 2–3 higher than PFL-f. Therefore, this gives an indication of uncertainty in the very highest PFL-f values and the borehole total transmissivities.

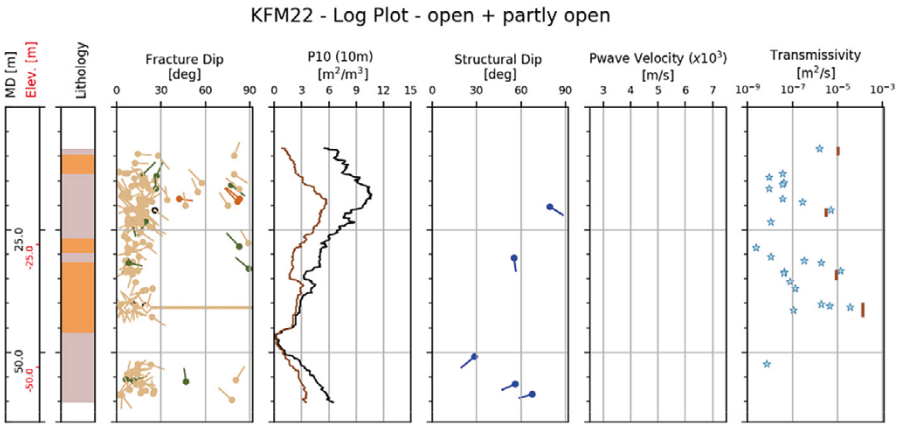


***Figure 2-17.*** *Log Plot for KFM22 showing latest PFL-f measurements (stars) and short-interval impeller logging.*

## 2.5 Interference tests

Five interference tests were performed in 2018 in one old and four new percussion drilled holes (HFM33 and HFM43–46 respectively), each pumped for 2 weeks or 3 weeks in the case of HFM43. The total transmissivity for each of these holes is around $5 \times 10^{-5}$ to $3 \times 10^{-4}$ $m^2/s$. Monitoring of the responses is available for the surrounding holes as exemplified for the longest test in HFM43 in Figure 2-19. The total transmissivity of HFM33 was c $4.7 \times 10^{-4}$ $m^2/s$.

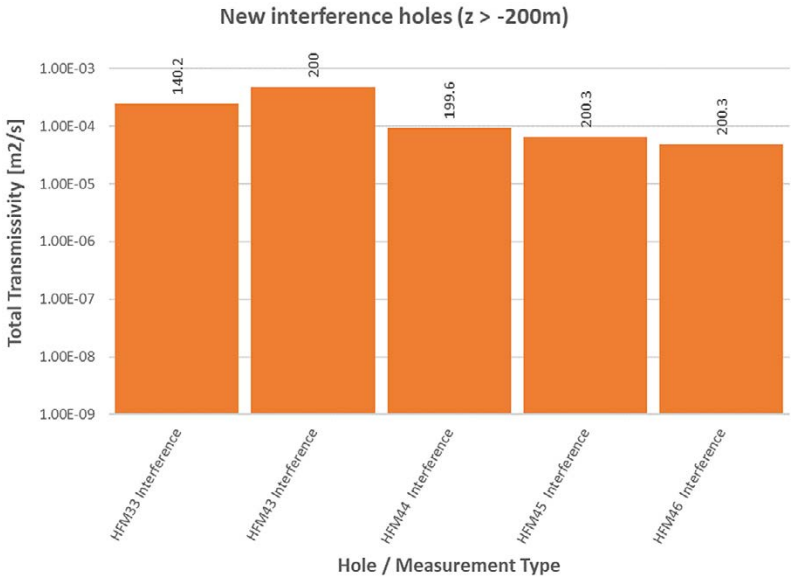


***Figure 2-18.*** *Total transmissivity for five new interference tests in percussion drilled holes.*

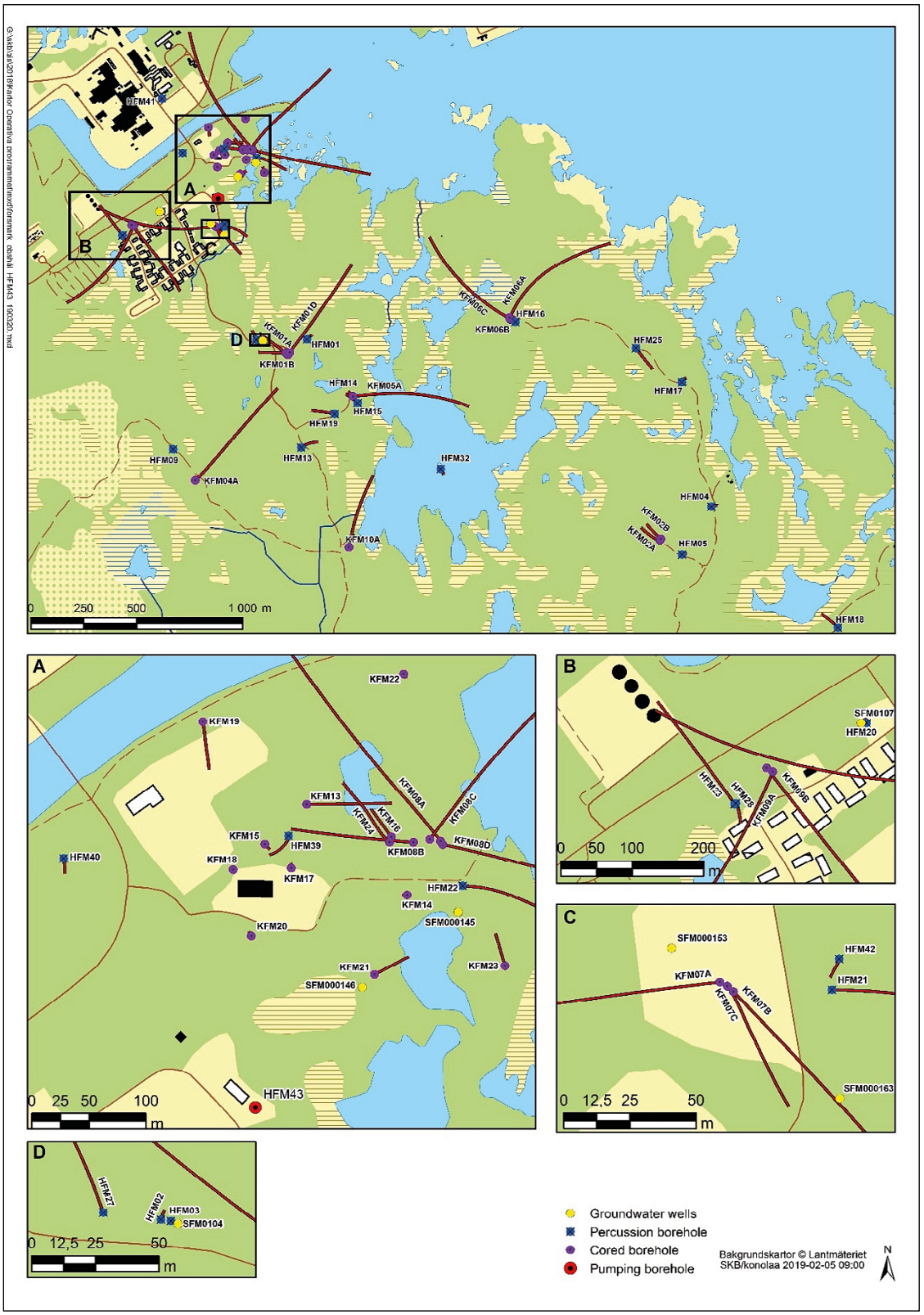


***Figure 2-19.*** *Configuration of boreholes involved in the HFM43 interference test.*

## 2.6 Data management

To manage and analyse the data summarised in Sections 2.1 through 2.5, a specific database has been developed to provide a basis for fracture conceptualisation and modelling, called FORSIDE (FORsmark Site Interpretative Database Environment). V0.1 is written in PostgreSQL (PostgreSQL 2017) with the PostGIS extension (PostGIS 2017) to provide spatial analysis functions supporting interpretative analyses and a links to Geological and DFN models. The main advantages of PostgreSQL for this application are:

- It is open source and hence is widely used in academia and industry.
- PostgreSQL has a geospatial extension (postGIS) which supports geometric data types (e.g., points, lines, surfaces) and supports geometric functions (e.g. distances from surfaces, translations between co-ordinate systems).

The intended end users of FORSIDE are SKB and its consultants and it is envisaged that it will form a secure shared data environment for use in data interpretation and analysis in support of modelling studies. In particular, FORSIDE is implemented to support a dynamic data acquisition framework capable of handling import, analysis and export of data on an ongoing basis and serve multiple user groups. Data flow and manipulations are traceable and reproduceable by storing functionality directly in the database, providing an easy to maintain, shared collaborative environment. The overarching philosophy is to streamline and accelerate the process of taking new data from SICADA into the database to produce updated interpretative analyses. The main benefits to modelling groups using FORSIDE are:

- It forms a single source of truth accessible to multiple users and promotes shared learning.
- It has QA and an audit trail.
- It is easy to update as new data becomes available.
- It can be interrogated with queries/scripts/functions including spatial analysis using postGIS functionality.
- It can be integrated into a wide range of post-processing software such as Python and Excel.

A schematic showing the role of FORSIDE in the information chain is presented in Figure 2-20. FORSIDE acts as a ‘hot storage’ system providing a dynamic and readily accessible link between ‘cold storage’ storage of SICADA and the end-users. FORSIDE is also capable of storing model outputs and interpretative geometries, such as domain volumes or geological surfaces and sharing these between user groups. It is emphasised here that although the hot-storage database set-up for this project has focused on DFN activities, other geological modelling activities could readily be integrated into the PostgreSQL database to broaden its remit and to remove the need for each end-user having separate versions of the data and duplicating analyses.

Data and analysis can be pulled from the database in multiple ways. Most simply, views and queries can be run, and their contents viewed and/or downloaded as .csv files. Alternatively, Excel can also be used to interface with the database directly, pulling query results straight into spreadsheets. For geometric data, an interactive tool for exporting ESRI shape files.

In addition to standard data I/O, a number of Python scripts have been developed to post-process and visualise the data. Python is a widely used high-level scripting/programming language and provides support for integrating with PostgreSQL, allowing data to be pushed and pulled from the database. Python has a huge range of libraries for data analysis including stereonet plotting, sophisticated graphing, statistical analysis and data manipulation. The Python library *psycopg2* allows Python to interface with PostgreSQL. Python scripts for producing stereonets (e.g., Figure 3-11) and or log plots (e.g., Figure 2-17) are available for FORSIDE.

The current version of FORSIDE v0.1 (see Figure 2-21) provides a strong foundation for future characterisation and modelling studies. It includes spatial data for borehole surveys and fracture logs (core, percussion logging, crush zones), rock properties, hydraulic data, deformation zones and FFM 3D models. A set of functions associated with this data permits spatial and statistical analyses of orientations, intensities, flow-fracture linking, and exports to GIS formats and Golder’s DFN modelling tool, FracMan.

The analysis and post-processing scripts are focused on the near surface but can readily be extended to depths.

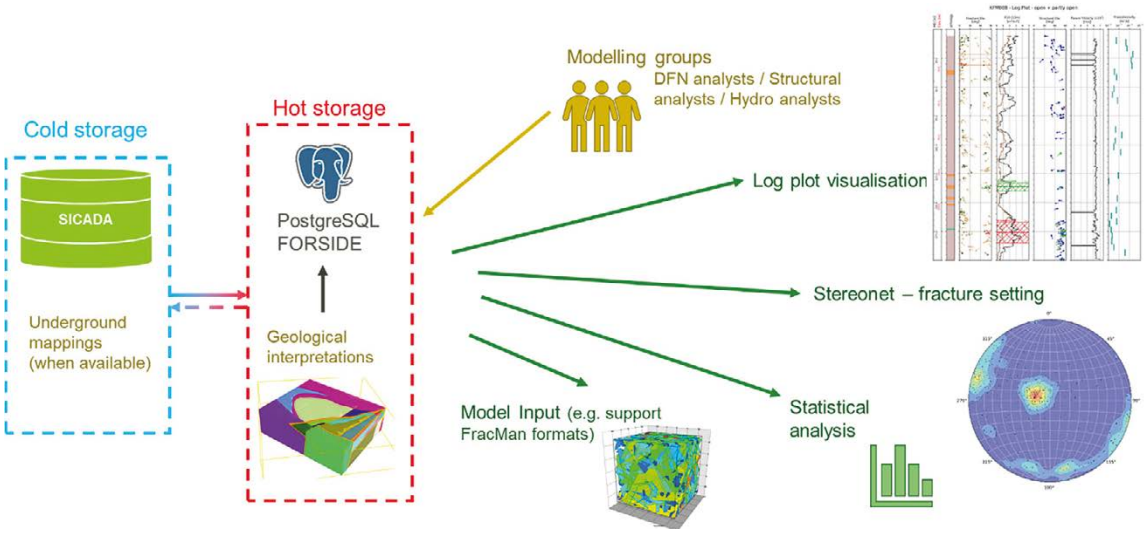


***Figure 2-20.*** *Flow of information and models between cold storage archives (e.g. SICADA) and modelling groups.*

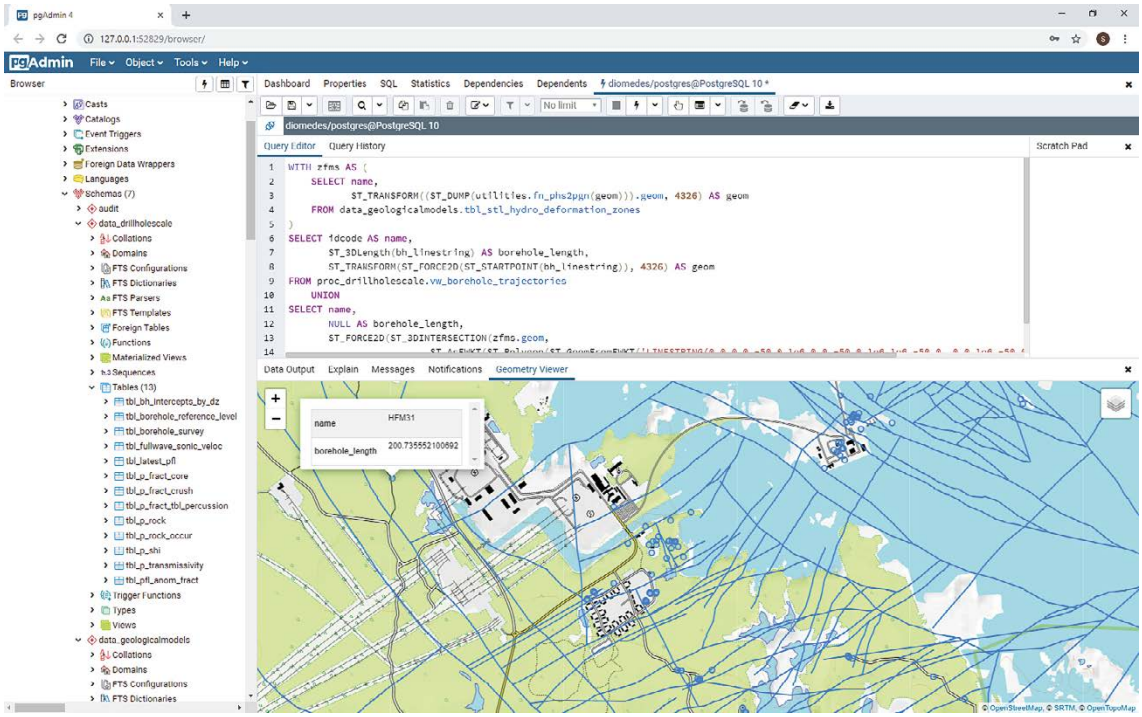


***Figure 2-21.*** *View of the FORSIDE SQL and GIS environment.*

# 3 Structural interpretations for DFN modelling

This chapter describes the new interpretations made of fracture and network geometrical properties.

## 3.1 General approach to DFN conceptualisation

This study does not represent a complete re-appraisal of the Forsmark v2.2 DFN model (Follin et al. 2007, Fox et al. 2007). Rather we build on those conceptual foundations, re-assessing the model parameterisation using the expanded dataset from boreholes KFM11–24 with their particular focus on characterising the top 100 m of bedrock inside the Forsmark tectonic lens.

New elements of the DFN methodology used here relative to DFN 2.2 include:

- Identification of sets for each borehole.
- Subdivision of FFM02 to include near-surface domain.
- Exploration of different intensity-size-transmissivity relationship for reactivated sub-horizontal fractures.
- Hydraulic properties of deformation zones linked to stress field with conditioning.
- Hydromechanical coupling of transmissivity and stress field.
- Simulating multiple realisations of single-hole hydraulic tests in many individual boreholes.
- Upscaling DFN to ECPM permeability tensor for DarcyTools and MIKE SHE models.

Notable elements *not* explored in the methodology used here:

- Modelling fractures as partially open over some part of their surface, rather than modelling a fraction of fractures as fully open (as here) and the rest as fully sealed.
- Modelling intra-fracture variability in openings and transmissivity.
- Modelling deformation zones as swarms of fractures.
- Creating DFN models by simulating genetic processes of nucleation, growth, termination and arrest.
- Conditioning fracture locations and properties on borehole logs.

### 3.1.1 Deformation history and mineralogical ages for Forsmark

A framework for describing the fracture patterns seen at Forsmark comes from the understanding of their genesis derived during SDM-Site from the patterns of deformation zones and radiometric dating of minerals. A summary is given below.

The rocks in the Forsmark area display evidence of a protracted ductile deformational history, with the development of a penetrative fabric under amphibolite-facies conditions followed by folding on different scales between 1.87 and 1.86 Ga (Figure 3-2) (Stephens 2010). The rocks inside the Forsmark tectonic lens display a predominantly linear grain-shape fabric and folds that plunge moderately to the south–east. In contrast, the rocks in the ductile high-strain belts that surround the Forsmark tectonic lens (Figure 3-1) show a generally more intense planar and linear grain-shape fabric.

Between 1.85 and 1.8 Ga uplift to the 500 °C geotherm occurred, which is inferred to contribute to focusing of strain along more spatially constrained zones. Regionally significant structures with a trace length greater than 10 km at the current ground surface, including the Forsmark (WNW), Eckarfjärden (NW) and Singö (WNW) deformation zones, formed during this time (Figure 3-2A).

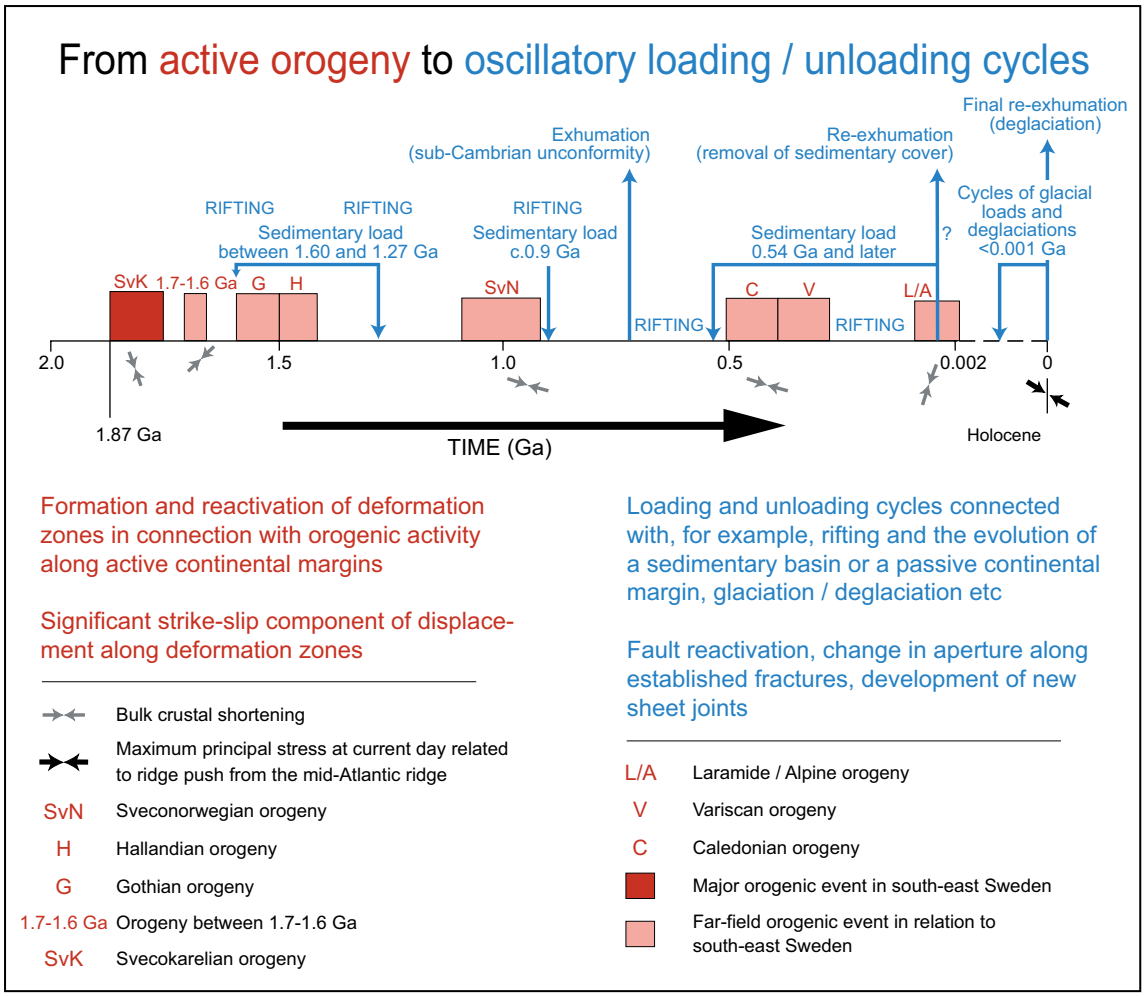


***Figure 3-1.*** *Tectonic activity (red) and oscillatory loading and unloading cycles (blue) from 1.9 Ga to the Holocene in the Fennoscandian Shield in the south–eastern part of Sweden (Stephens 2010).*

Cooling to the 300 °C geotherm occurred between 1.8 and 1.7 Ga, possibly initiating brittle deformation during the latest part of the Svecokarelian orogeny (Söderlund et al. 2009, Stephens 2010). Two more significant local structure sets inside the Forsmark tectonic lens formed during this time (Figure 3-2B). They strike ENE−WSW or NNE−SSE and are steeply or gently dipping fracture zones. Between 1.7 and 1.6 Ga the structures continued to develop (Figure 3-2C), possibly in response to the Gothian orogeny (Stephens et al. 2007). Cooling beneath the c 225−200 °C geotherm occurred between 1.6 and 1.5 Ga (Stephens 2010).

Brittle deformation continued as a far-field response to Sveconorwegian tectonic activity between 1 100–900 Ma (Figure 3-2D). There is evidence for several relatively minor brittle deformation events after the establishment of the sub-Cambrian peneplain, probably during the Phanerozoic (Stephens et al. 2007). Some reactivation of fractures is occurring under the current stress regime (Figure 3-2E) (Stephens et al. 2007).

A summary of palaeostress field reconstruction using site-by-site and merged data sets from outcrops and oriented drill cores is provided by Saintot et al. (2011) as follows:

Transpressive deformation with a regional NNW–SSE maximum stress axis, associated with clockwise stress deviation inside a tectonic lens, resulted in dextral slip along regionally significant, steep WNW–ESE and NW–SE deformation zones. The semi-brittle and most of the brittle structures, including specifically the epidote-bearing fractures, were established during this oldest regime around 1.8 Ga (latest Svecokarelian). A younger palaeostress field with a NE–SW maximum stress axis, which was also transpressive in character, is inferred to have been active at 1.7–1.6 Ga. The best defined

palaeostress field is transpressive in character with a WNW–ESE maximum stress axis that resulted in sinistral reactivation along the WNW–ESE and NW–SE zones. The main set of laumontite-stepped faults developed at this stage at 1.1 – 0.9 Ga (Sveconorwegian). It is impossible to exclude fully the influence of reactivation during even younger Phanerozoic tectonic events. A similar deformation history has been interpreted at Olkiluoto (Mattila and Viola 2014) across the Gulf of Bothnia.

This conceptualisation of the deformation history at the site provides context for interpretation of global fracture sets as NW and NS, ENE and NE, EW and SubH, and this order as a working assumption on relative ages. However, reactivation may have resulted in more complex relative age relationships. These same orientation sets were interpreted in outcrops as suitable for the near-surface domain FFM02 in Geo-DFN v2.2 (Fox et al. 2007).

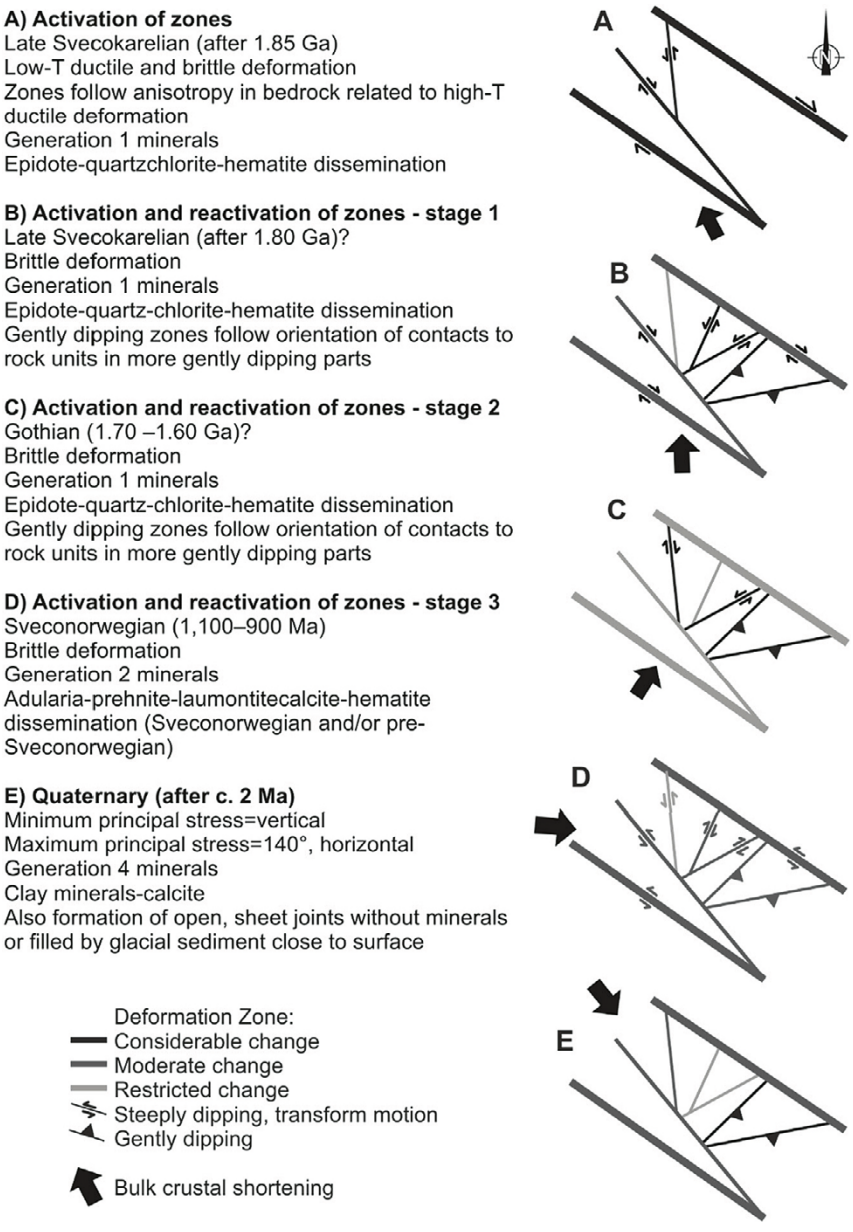


***Figure 3-2.*** *A series of cartoons showing the conceptual model for the activation and reactivation of regional scale deformation zones around Forsmark in response to far-field tectonic activity, and associated fracture fill minerology. The WNW and NW striking deformation zones correspond to the Forsmark, Singö, and Eckarfjärden deformation zones (Figure 4-2). The different generations of minerals are referred to in Section 6.4. Adapted from Stephens et al. (2007).*

Four generations of fracture minerals have been identified (Stephens 2010), see Table 3-1, that correspond with the stages of deformation and orientations as indicated in Figure 3-2, with Generation 3 between stages D and E. The presence of these minerals can be used to indicator of relative ages of fractures, e.g. epidote indicates stage 1 fractures, whereas clay minerals indicate either younger or reactivated fractures.

**Table 3-1. Summary of the paragenesis of mineralogy at Forsmark (Sandström et al. 2008b).**

| Generation | Dominant Minerals | Formation Temp. (°C) | Comments |
|---|---|---|---|
| 1 | Epidote, chlorite, quartz | > 200 | Dominated by fractures sealed with hydrothermally precipitated epidote, quartz and Fe-rich chlorite. This generation formed between 1.8 and 1.1 Ga and is possibly related to late Svecokarelian and/or Gothian tectonothermal events. |
| 2 | Adularia, prehnite, laumontite, chlorite, calcite, hematite | ~150 – 280 | Consists of a sequence of hydrothermal fracture minerals particularly common along steep, ENE–WSW to NNE–SSW and NNW–SSE fractures. Consists of both reactivation of older fractures and formation of new fractures. Gothian orogeny. |
| 3 | Quartz, calcite, pyrite, corrensite, adularia, analcime, asphaltite | ~50 – 190 | Consists of minerals precipitated under low-T conditions during the Palaeozoic. Stable isotopes in calcite and the presence of asphaltite indicate that the formation fluid was influenced by organic material. The orientation of fractures with Generation 3 minerals suggests reactivation of fractures filled with older minerals but new fractures were also formed. Variscan orogeny. |
| 4 | Clay minerals, chlorite, calcite, ± pyrite, ± FeOOH | < 50 | Dominated by chlorite/clay minerals and thin precipitates of calcite in predominantly hydraulically conductive fractures. These minerals are prominent along sub-horizontal and gently dipping fractures but are also present in different sets of steeply dipping fractures. Most of the hydraulically conductive fractures are ancient structures. |

The core description records up to four minerals on each fracture surface. In order to assign a mineral generation to each fracture, the following logic is applied to the list of minerals on each fracture:

- Generation 2: if (laumontite) or (prehnite) or (hematite) present;
- Generation 3: if (Not G2) and ((analcime) or (asphalt) or (adularia) or (calcite with quartz and/or pyrite));
- Generation 1: if (Not G2) and (Not G3) and ((epidote) or (quartz) or (chlorite without clay, calcite or pyrite));
- Generation 4: if (Not G2) and (Not G3) and (Not G1) and ((clay) or (chlorite) or (calcite) or (pyrite)).

This relative age classification system is important to the conceptualisation of fracturing as an indicator of ancient versus potentially younger or reactivated fractures, especially in the near-surface, and as a basis for describing transport properties of fractures, i.e. what minerals are present for reactive transport processes. In this study, it is used to estimate the fraction of fracture surface area that may have been affected by processes since the original fracturing of the rock, and how that varies with depth.

The above rules classify about 80 % of fractures to a mineral generation. Note that by determining Generation 4 last it becomes a bit of a catch all, but it also means that complex mineral assemblages with older minerals get assigned to earlier generations. Fractures with only Generation 1 and 2 minerals might be expected to be ancient and undergone limited reactivation and relatively recent alteration, while Generation 4 might have been relatively recently reactivated and altered. Some examples of stereonets with poles coloured by mineral age are shown in Figure 3-3 and Figure 3-4. It may be observed that sub-horizontal fractures tend to be mostly a mix of Generation 1 and Generation 4, indicating that many of these fractures are ancient, but there are some younger or reactivated fractures. Hence, sub-horizontal fractures are in fact a superposition of two different ages of fractures. Generation 2 fractures tend to be mostly ENE and NE subvertical fractures, consistent with stage 3 deformation. Generation 3 is mostly sub-vertical NE subvertical and some sub-horizontal fracturing.

In summary, mineralogy and mineralogical generation has potential to differentiate between fractures that have been open and hosted circulation of hydrothermal fluid in ancient times and fractures in which minerals have formed in more recent times as a result of new fracturing or reactivation/extension of ancient fractures. Hence, if there is evidence of over-printing of fractures with different properties with different properties, such as size and transmissivity, then mineralogy potentially provides a basis to subset fractures belonging to the same orientation set.

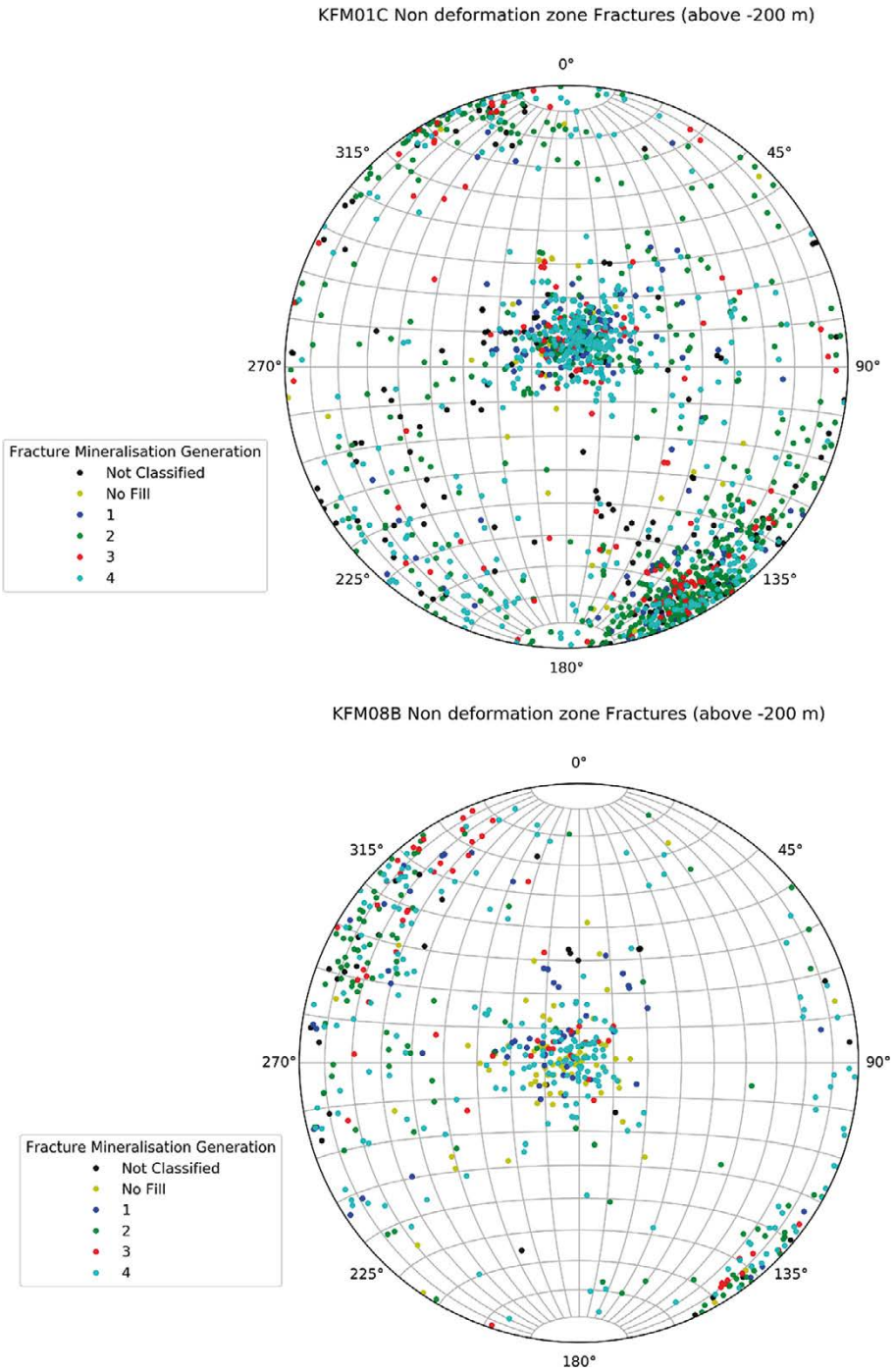


***Figure 3-3.*** *Stereonet showing fracture age generation as categorised by mineralisation of fractures in: Top) KFM01C from elevation c −5 m to −200 m; Bottom) KFM08B from elevation c 0 m to −200 m.*

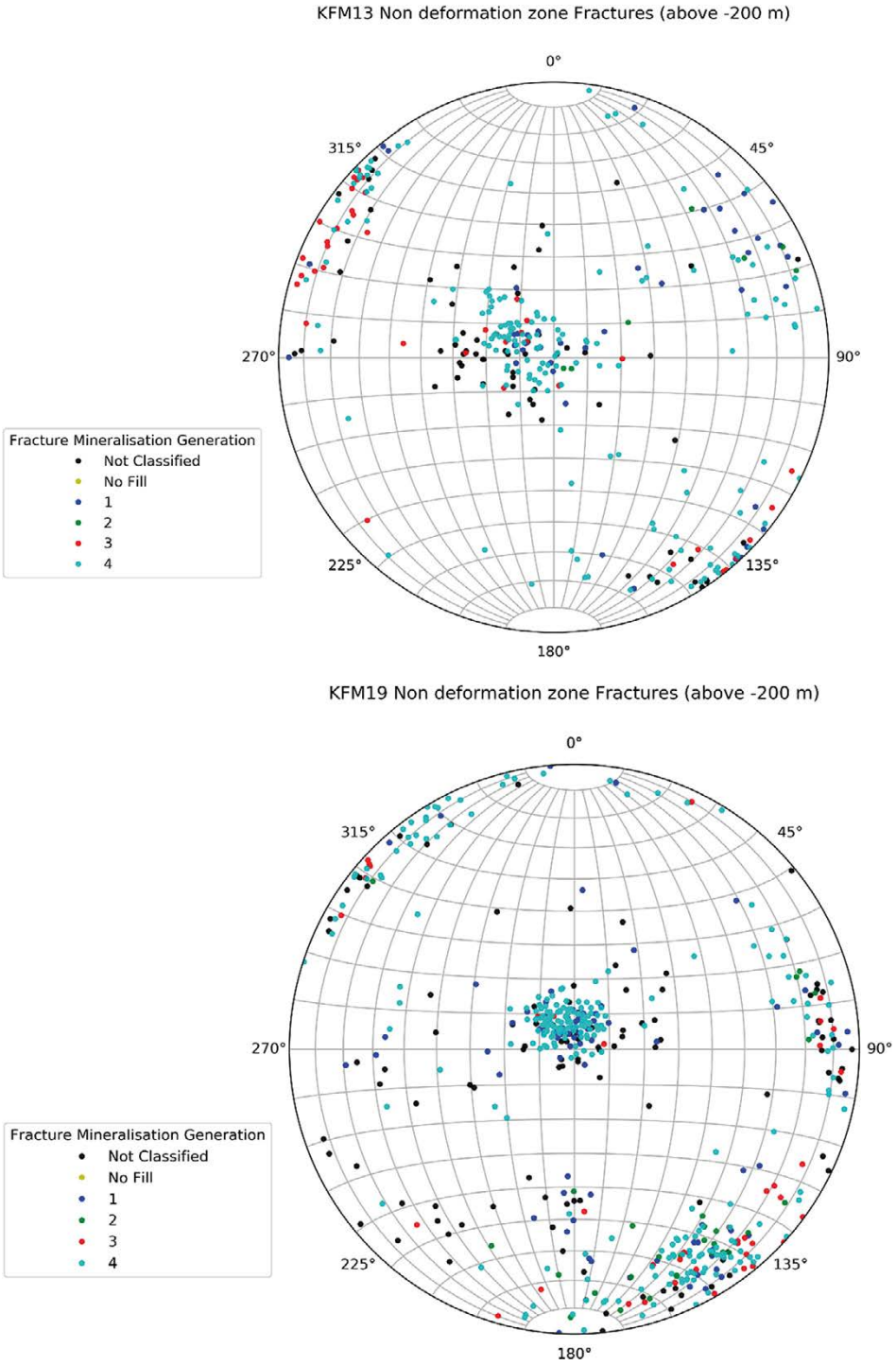


***Figure 3-4.*** *Stereonet showing fracture age generation as categorised by mineralisation of fractures in: Top) KFM13 from elevation c −5 m to −125 m; Bottom) KFM19 from elevation c 0 m to −85 m.*

### 3.1.2 Fracture orientations

The subdivision of the rock into fracture domains was used as the only control on fracture orientations in the F2.2 DFN models (Fox et al. 2007). However, there are variations of orientations between holes within a fracture domain relating to the fold structure of the Forsmark tectonic lens forming a dome like structure at the north end. Figure 3-5 and Figure 3-6 illustrate the variability of fracture and foliation orientations, respectively, across the area. Foliation has a strong NW component related to Stage A deformation of Figure 3-2, but with more gently dipping ductile deformation in the centre and south of the lens. Some of the fracturing tends to follow this pattern of foliation orientations, but there is significant ENE and NE oriented fracturing not seen in the foliations. Therefore, foliation is only an indication for some subsets of fractures; NW and some sub-horizontal. Sub-horizontal and ENE fractures seem to be the most consistent and important sets. Due to the variability in fracture orientations between even nearby boreholes, for this study it was decided to divide fractures into the same six orientation sets across all boreholes, but to adjust the boundaries of these sets (hard sectors) to suit the orientations seen in individual holes. Conceptually, it is assumed that all parts of the bedrock have subject to the same tectonic deformation, but local conditions have resulted in some rotation of fracturing (and palaeostress) and the relative intensities between sets.

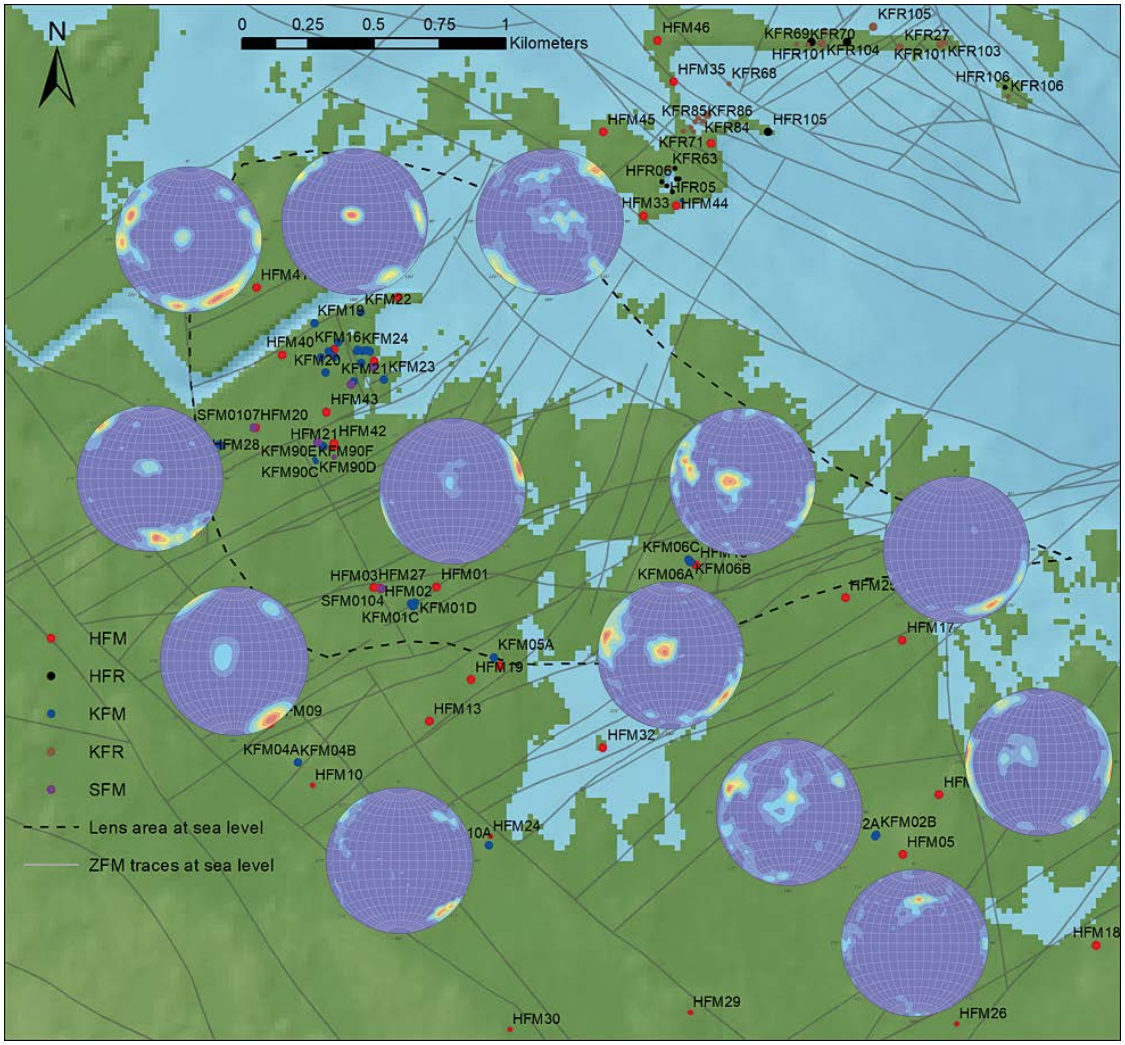


***Figure 3-5.*** *Fracture orientations shown as stereonets from selected boreholes across the Forsmark tectonic lens superimposed on a map showing the locations of boreholes and modelled deformation zones.*

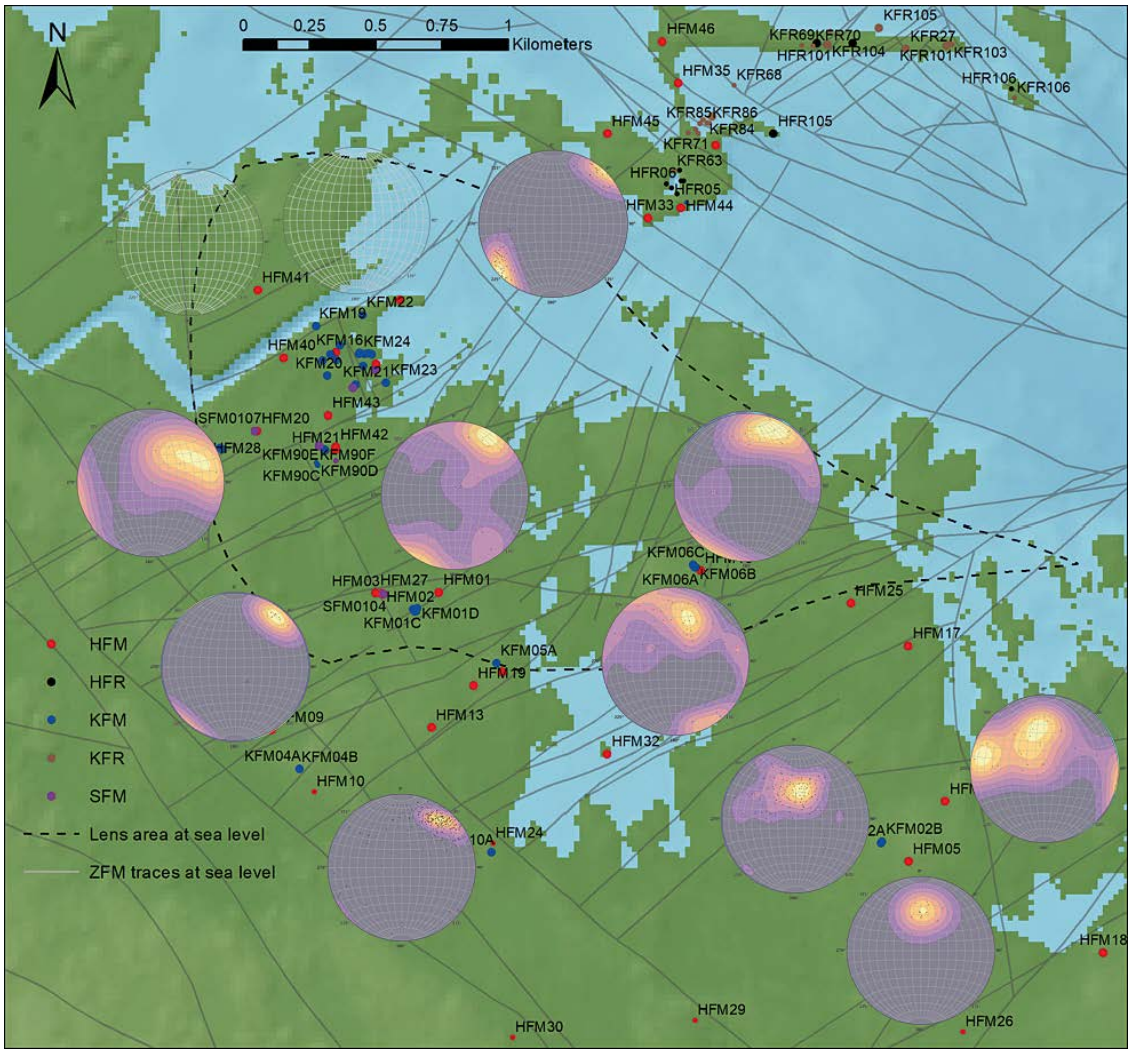


***Figure 3-6.*** *Foliation orientations shown as stereonets from selected boreholes across the Forsmark tectonic lens superimposed on a map showing the locations of boreholes and modelled deformation zones.*

Because of the focus on the near surface, orientations were only analysed for fractures above an elevation of −200 m. Figure 3-7 through Figure 3-10 show examples of the assignment of fractures to the six global sets for four boreholes through FFM02 and FFM01. The fracture poles associated to each set are coloured by the set. Some moderately dipping fractures also appear with diffuse orientations difficult to assign to a set and inconsistent between boreholes. It is not clear if these orientations are a genuine part of the distribution or a result of image quality and interpretation (see Stigsson 2008, 2016). Here, these moderately dipping fractures are described as local sets, not included in the DFN model, but with the intensities of the six global sets scale so that the total fracture intensity is maintained. Mean poles and Fisher distribution functions (i.e. Fisher concentration parameters) were fitted to each set for each borehole. The spread of mean poles across all boreholes is shown in Figure 3-11. There is considerable rotation in the mean poles subvertical sets resulting from a mix of genuine variability and the sometimes subjective partitioning of fractures between sets. In a more comprehensive study, 3D interpolation of mean poles could have been used to model these rotations. Here, however, the mean of mean poles within a fracture domain has been used, along with the median Fisher concentration to represent variability within a set.

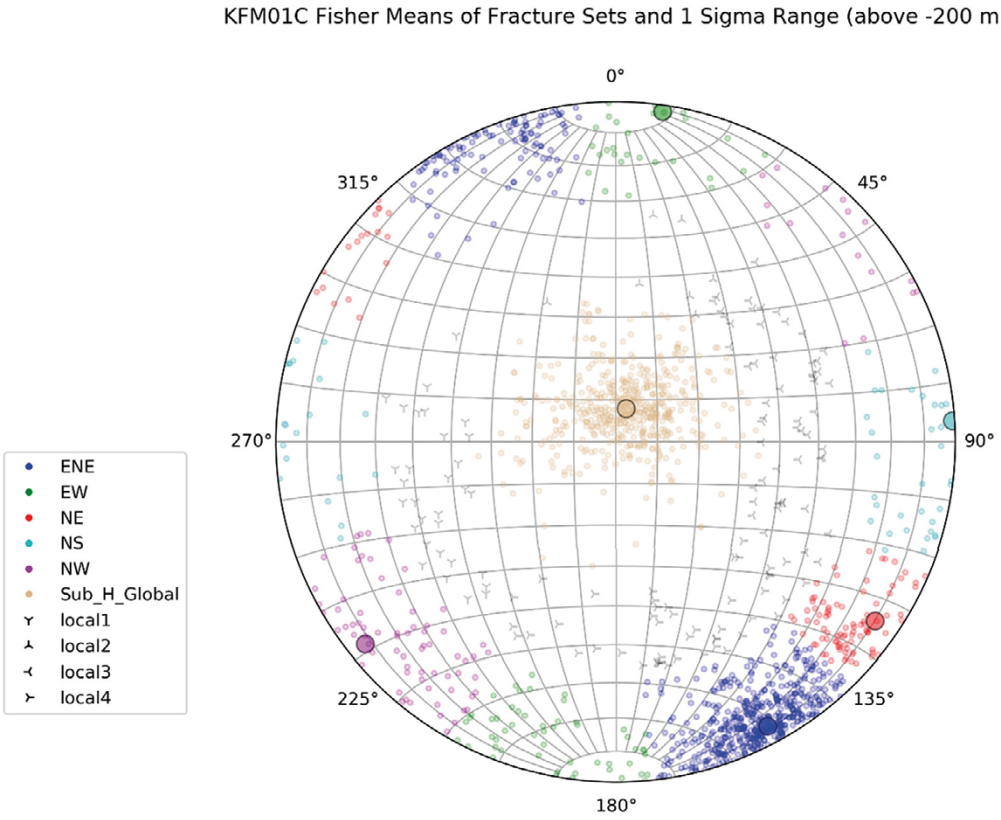


***Figure 3-7.*** *Orientation sets for fractures within KFM01C above z = −200 m. Mean pole of the orientation sets are shown as large circles.*

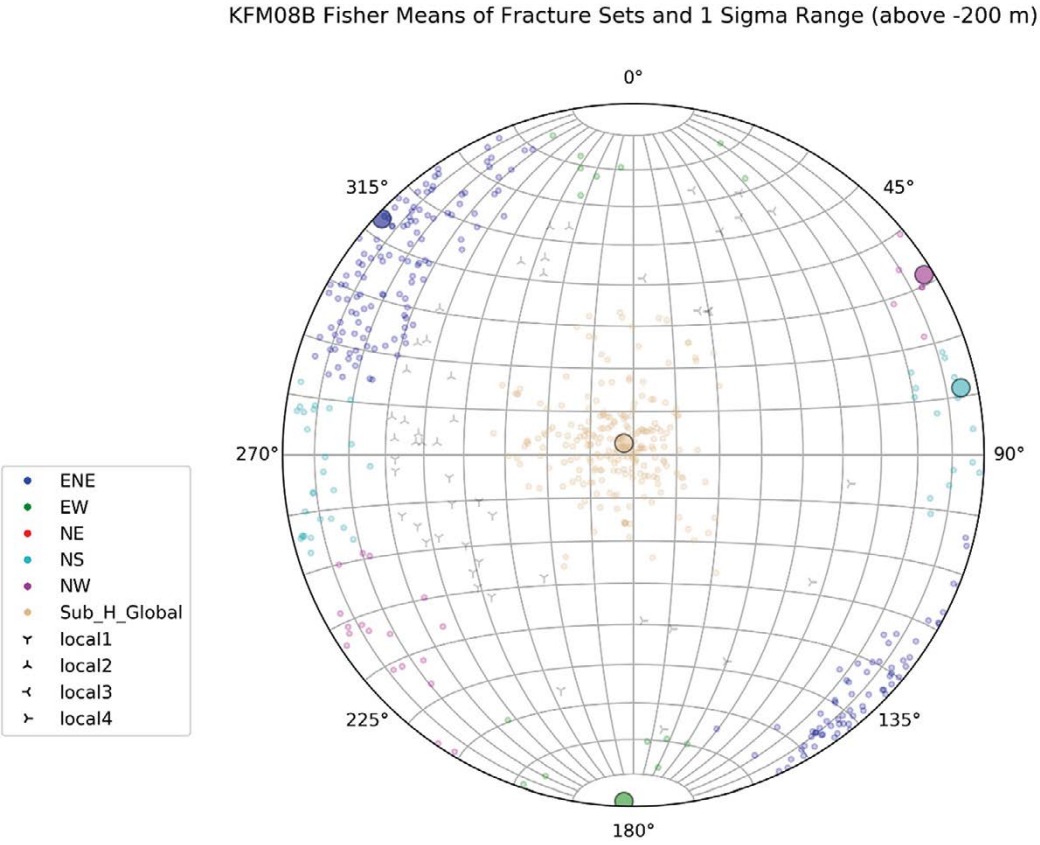


***Figure 3-8.*** *Orientation sets for fractures within KFM08B above z = −200 m. Mean pole of the orientation sets are shown as large circles.*

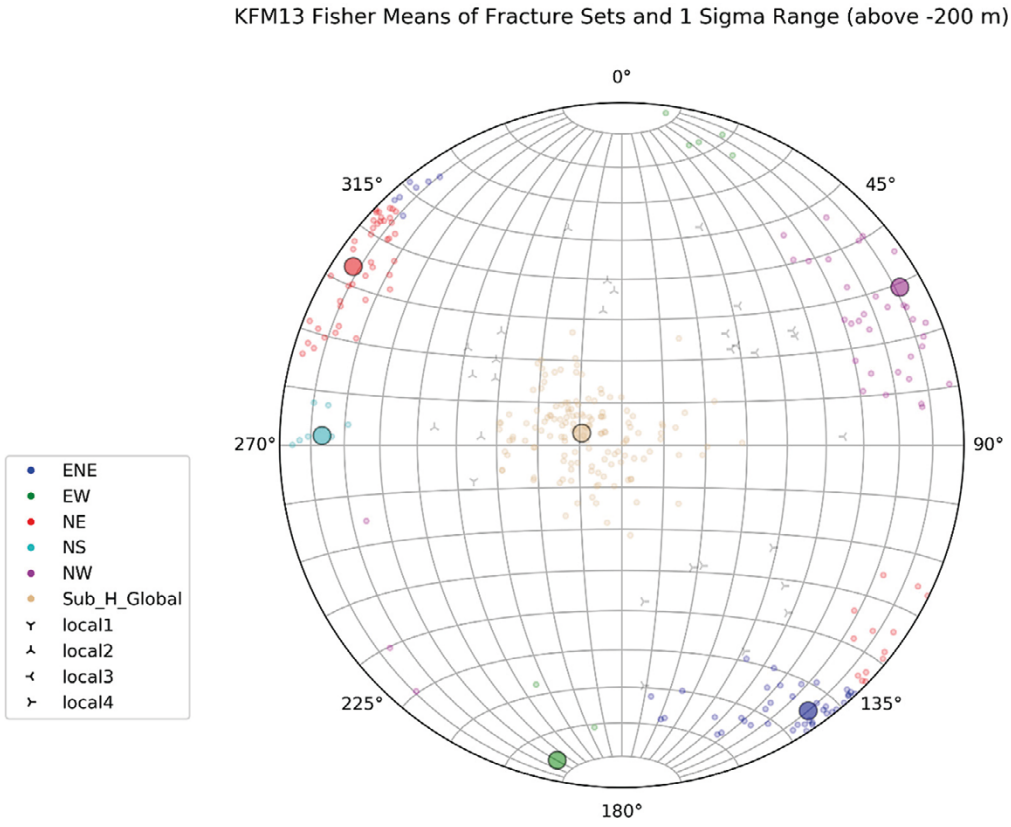


***Figure 3-9.*** *Orientation sets for fractures within KFM13 above z = −200 m. Mean pole of the orientation sets are shown as large circles.*

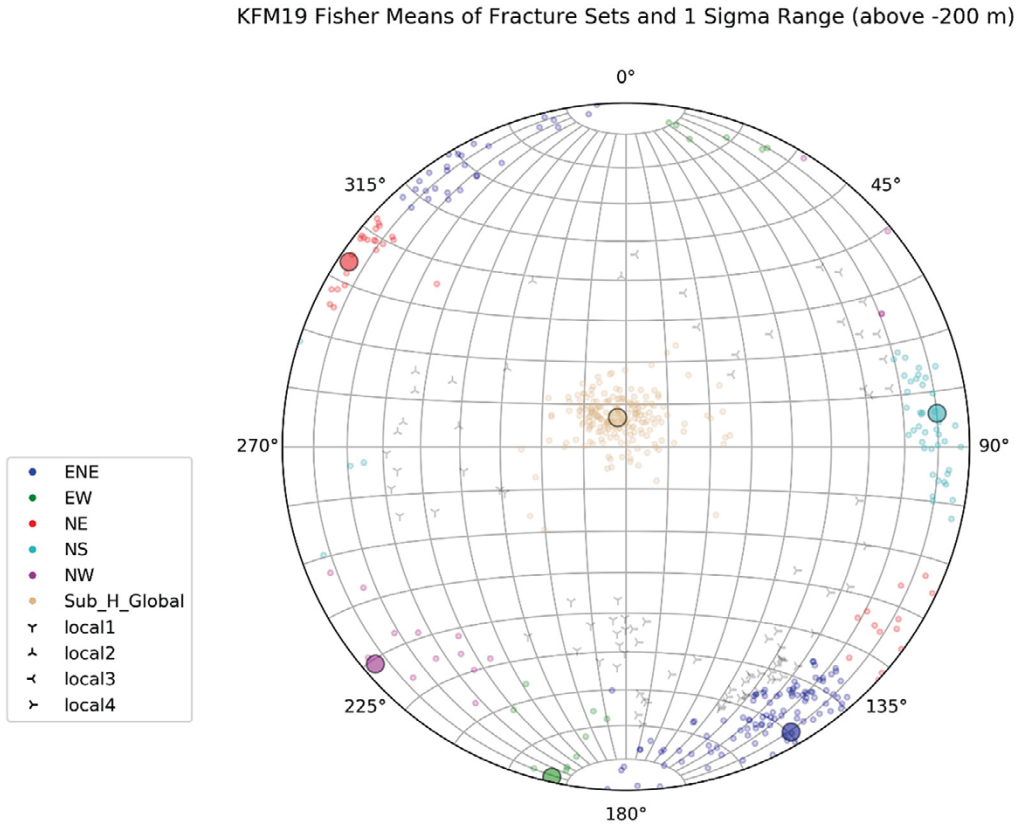


***Figure 3-10.*** *Orientation sets for fractures within KFM19 above z = −200 m. Mean pole of the orientation sets are shown as large circles.*

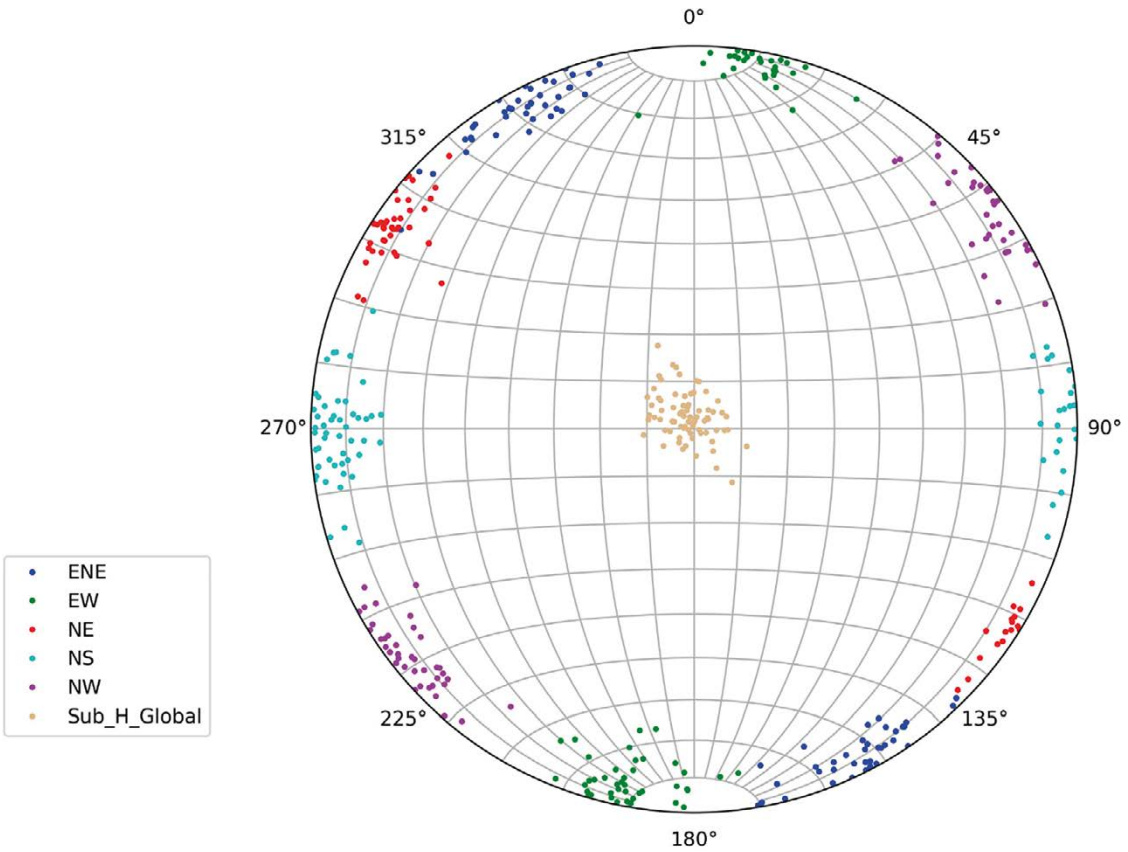


***Figure 3-11.*** *Stereonet of mean poles for each global set in each borehole.*

### 3.1.3 Fracture domains and elevation regions

The fracture domains are largely unchanged from F2.2 modelling, except that FFM02 is split into FFM02U and FFM02L at −30 m elevation, see Section 2.3. Geo-DFN F2.2 (Fox et al. 2007) noted that fracture density is a function of depth and interpreted a gradual depth for FFM01 and FFM02 in Section 4.4.5 of that report. In the Hydro-DFN (Follin et al. 2007) proposed a split into three elevation regions at −200 m and −400 m for FFM01 in Table 11-20. Here, we use four elevation regions with divides at −30 m, −200 m and −400 m to represent changes in intensity and potentially size parameters with elevation.

The modelled domains are: FFM02U, FFM02L, FFM01 ($z > -200$ m, $-200$ m $> z > -400$ m, $z < -400$ m). Outside these ($z > -30$ m, $-30$ m $> z > -200$ m, $-200$ m $> z > -400$ m, $z < -400$ m).

### 3.1.4 Intensity and size

The intensity of all fractures and open/partly open fractures is calculated for each the above domains for use in the model, but here only the open/partly open intensity is used because only the potentially hydraulically active fractures are modelled. Intensities are calculated by set and aggregated over all borehole intervals within a domain. The fractures and associated borehole length within the geological single hole interpreted thicknesses of modelled deformation zones, ZFM, are removed from this calculation.

There are few outcrops from which to interpret fracture size distributions, and therefore there was considered little value in re-interpreting the size model. Because the focus is near surface hydrogeology, the starting point for the size model was taken as the power-law size model used for the Hydro-DFN model of FFM02 in Table 11-22 of Follin et al. (2007). Following the methodology of Follin et al. (2007) the size model for open was calibrated in order to give a connectivity of each set consistent with the measured intensity of water conducting fractures within each set. Because the subvertical sets are relatively sparse and boreholes near vertical, few subvertical water conducting fractures were found so

it was unnecessary to adjust the size model for the subvertical fractures. Instead, attention was focused on calibrating the size model of the sub-horizontal set. Some additional information was considered for the size distribution of sheet joints in the near surface using digitised maps of fractures in the channel inlet for the Nuclear power plant (Carlsson 1979).

## 3.2 Orientations of structures

The methodology for defining a fracture orientation model is described in Subsection 3.1.2. In order to illustrate the relative importance of the different sets, Table 3-2 and Table 3-3 give the percentages of each set by HFM and KFM holes, respectively. It may be observed that the sub-horizontal set is ubiquitous and often the dominant set. Each of the global sets makes up more than 5 % of fractures in most holes, with ENE being the second most important set. The EW set can be sporadic, as can the NS set. The moderately dipping local sets are mostly a minority (less than 5 %), except local3 which is a NW set with a moderate dip to the SW.

**Table 3-2. % of Terzaghi corrected open fracture inside the Forsmark lens by HFM hole. Numbers in red are those with less than 5 % of the total fracture count, green text those with more than 20 %.**

| idcode | ENE | EW | local1 | local2 | local3 | local4 | NE | NS | NW | SubH | Not Set |
|---|---|---|---|---|---|---|---|---|---|---|---|
| HFM01 | 4.6 | 6.0 | 1.5 | 3.9 | 13.9 | 2.8 | 1.0 | 7.6 | 49.8 | 8.9 | 0.0 |
| HFM02 | 16.5 | 28.3 | 0.0 | 3.6 | 3.0 | 0.0 | 23.2 | 4.0 | 4.0 | 17.5 | 0.0 |
| HFM09 | 72.2 | 0.0 | 0.0 | 0.0 | 0.0 | 0.0 | 0.0 | 0.0 | 0.0 | 27.8 | 0.0 |
| HFM14 | 28.0 | 1.0 | 1.4 | 3.1 | 6.1 | 2.2 | 0.0 | 21.2 | 4.1 | 33.0 | 0.0 |
| HFM15 | 22.6 | 3.0 | 0.0 | 0.8 | 7.3 | 7.9 | 0.4 | 2.2 | 6.5 | 49.2 | 0.0 |
| HFM16 | 0.0 | 2.7 | 1.3 | 0.7 | 1.4 | 0.0 | 70.0 | 0.0 | 0.0 | 23.9 | 0.0 |
| HFM19 | 27.8 | 4.1 | 0.4 | 4.0 | 7.2 | 2.1 | 0.0 | 4.8 | 9.4 | 40.1 | 0.0 |
| HFM20 | 49.7 | 27.5 | 0.0 | 0.0 | 0.0 | 0.0 | 0.0 | 0.0 | 0.0 | 22.8 | 0.0 |
| HFM21 | 53.8 | 0.0 | 0.0 | 0.0 | 30.3 | 0.0 | 0.0 | 0.0 | 0.0 | 15.9 | 0.0 |
| HFM22 | 67.6 | 6.7 | 0.0 | 2.5 | 0.0 | 0.5 | 0.0 | 3.3 | 1.9 | 17.6 | 0.0 |
| HFM28 | 34.3 | 14.3 | 2.6 | 1.4 | 9.6 | 3.3 | 0.0 | 0.0 | 14.8 | 19.7 | 0.0 |
| HFM38 | 11.2 | 7.8 | 0.0 | 1.7 | 2.5 | 1.2 | 15.9 | 17.8 | 9.4 | 32.5 | 0.0 |
| HFM39 | 40.7 | 1.7 | 0.0 | 6.2 | 0.7 | 1.7 | 0.0 | 3.5 | 0.0 | 45.5 | 0.0 |
| HFM40 | 0.0 | 0.0 | 0.0 | 0.0 | 67.0 | 0.0 | 0.0 | 0.0 | 0.0 | 33.0 | 0.0 |
| HFM41 | 10.7 | 0.0 | 13.0 | 6.2 | 0.0 | 0.0 | 14.4 | 4.0 | 8.0 | 43.8 | 0.0 |

**Table 3-3. % of Terzaghi corrected open fracture inside the Forsmark lens by KFM hole. Numbers in red are those with less than 5 % of the total fracture count, green text those with more than 20 %.**

| idcode | ENE | EW | local1 | local2 | local3 | local4 | NE | NS | NW | SubH | Not Set |
|---|---|---|---|---|---|---|---|---|---|---|---|
| KFM01A | 26.1 | 2.8 | 2.6 | 2.3 | 5.6 | 1.5 | 4.1 | 12.5 | 6.1 | 34.4 | 2.0 |
| KFM01B | 0.0 | 2.5 | 1.3 | 2.1 | 5.1 | 0.0 | 7.8 | 5.8 | 8.9 | 59.5 | 6.9 |
| KFM01C | 34.3 | 8.2 | 0.9 | 1.7 | 3.0 | 1.1 | 3.9 | 3.2 | 6.8 | 36.1 | 0.8 |
| KFM01D | 3.8 | 4.1 | 0.3 | 3.5 | 5.2 | 1.3 | 0.0 | 11.5 | 24.3 | 45.7 | 0.3 |
| KFM04A | 11.7 | 3.1 | 1.2 | 1.7 | 5.3 | 1.6 | 4.8 | 8.4 | 30.7 | 30.0 | 1.5 |
| KFM05A | 19.6 | 3.2 | 0.4 | 3.3 | 5.4 | 1.7 | 10.3 | 13.5 | 15.4 | 26.3 | 1.1 |
| KFM06A | 8.1 | 3.8 | 2.3 | 3.7 | 1.2 | 0.7 | 15.4 | 27.0 | 7.7 | 29.8 | 0.5 |
| KFM06B | 2.9 | 12.7 | 1.0 | 4.1 | 4.1 | 4.5 | 7.8 | 11.5 | 0.0 | 51.5 | 0.0 |
| KFM06C | 5.5 | 3.0 | 2.2 | 7.5 | 8.6 | 1.3 | 27.6 | 2.9 | 9.1 | 32.3 | 0.0 |
| KFM07A | 40.6 | 3.6 | 1.4 | 1.3 | 2.1 | 0.0 | 9.7 | 14.3 | 9.9 | 17.2 | 0.0 |
| KFM07C | 43.0 | 5.1 | 2.6 | 2.4 | 2.7 | 1.8 | 3.4 | 7.9 | 3.1 | 22.7 | 5.3 |
| KFM08A | 8.2 | 15.1 | 2.7 | 10.2 | 3.1 | 1.6 | 18.5 | 6.5 | 10.9 | 23.3 | 0.0 |
| KFM08B | 27.2 | 3.3 | 1.3 | 0.8 | 2.2 | 1.3 | 0.0 | 9.6 | 4.7 | 49.7 | 0.0 |
| KFM08C | 9.7 | 14.2 | 1.7 | 3.0 | 11.5 | 9.1 | 18.4 | 6.8 | 11.9 | 13.2 | 0.5 |
| KFM08D | 12.5 | 2.3 | 1.2 | 4.1 | 2.1 | 1.2 | 31.0 | 12.9 | 11.0 | 21.7 | 0.1 |
| KFM10A | 4.6 | 2.3 | 1.7 | 0.8 | 5.3 | 4.6 | 22.6 | 1.0 | 22.0 | 34.4 | 0.8 |

| idcode | ENE | EW | local1 | local2 | local3 | local4 | NE | NS | NW | SubH | Not Set |
|---|---|---|---|---|---|---|---|---|---|---|---|
| KFM13 | 10.8 | 5.0 | 0.0 | 2.8 | 2.1 | 2.2 | 10.2 | 2.0 | 14.9 | 38.5 | 11.4 |
| KFM14 | 9.5 | 5.2 | 0.0 | 0.0 | 0.0 | 0.0 | 3.3 | 2.8 | 3.6 | 63.2 | 12.3 |
| KFM15 | 9.8 | 0.0 | 1.7 | 1.0 | 9.3 | 0.8 | 0.0 | 0.0 | 9.6 | 53.7 | 14.1 |
| KFM16 | 32.0 | 11.4 | 0.0 | 0.8 | 1.0 | 1.5 | 0.0 | 0.6 | 6.5 | 39.2 | 7.1 |
| KFM17 | 7.8 | 7.6 | 0.0 | 0.8 | 5.1 | 0.9 | 0.0 | 4.6 | 3.9 | 55.4 | 14.0 |
| KFM18 | 3.4 | 17.3 | 5.0 | 0.0 | 14.1 | 2.9 | 3.8 | 0.0 | 0.0 | 43.6 | 9.9 |
| KFM19 | 20.0 | 5.8 | 0.6 | 0.5 | 4.0 | 3.7 | 4.6 | 6.0 | 0.8 | 44.1 | 10.0 |
| KFM20 | 17.9 | 2.1 | 2.7 | 3.4 | 3.4 | 8.0 | 0.0 | 1.7 | 8.9 | 39.7 | 12.2 |
| KFM21 | 5.0 | 4.6 | 0.0 | 0.9 | 5.3 | 1.0 | 0.0 | 0.0 | 7.1 | 62.0 | 14.1 |
| KFM22 | 18.8 | 1.6 | 0.0 | 0.5 | 0.0 | 2.7 | 0.0 | 0.0 | 1.9 | 52.3 | 22.2 |
| KFM23 | 22.5 | 13.9 | 0.3 | 3.5 | 2.2 | 1.4 | 0.0 | 0.8 | 2.6 | 42.1 | 10.6 |
| KFM24 | 21.1 | 5.1 | 2.7 | 2.2 | 7.5 | 0.7 | 19.9 | 6.7 | 8.2 | 26.0 | 0.0 |

Having subdivided fractures into sets, analyses of orientation models and differences in properties between the sets can be made. The mean pole of poles and median Fisher concentrations for fractures over all fracture domains above −200 m elevation are presented in Table 3-4. The percentages of open/closed fractures by domain and elevation regions are given in Table 3-5. The percentages of open fractures decrease with depth for all sets. The percentages are between 41 and 66 % in FFM02U, falling to 9–33 % in FFM01 −200 m > z > −400 m. The proportion of open fractures is consistently highest in SubH, which is subject to the least normal stress. NE and NS have the lowest percentages as they are subject to the highest normal stress (maximum horizontal stress is NW). EW fracturing is closest to the maximum horizontal stress direction and has the highest open proportion, but there are relatively few fractures with this orientation. Likewise, SubH and EW have the most gradual reduction of open fraction with depth, while NE and NS have the most dramatic reductions.

Figure 3-12 and Figure 3-13 show the distribution of mineral ages across each set and each domain for all and open fractures, respectively. See comments below.

**Table 3-4. Orientation parameters for the Fisher model used for each set.**

| | ENE | EW | NE | NS | NW | SubH |
|---|---|---|---|---|---|---|
| **Trend/Plunge** | 149.7/2.58 | 188.4/0.98 | 302.3/2.57 | 267.1/1.34 | 53.91/1.69 | 357.4/86.1 |
| **Fisher concentration** | 21.8 | 24.0 | 25.8 | 18.3 | 17.7 | 24.5 |

**Table 3-5. Percentages of open/closed fractures in each orientation set by domain.**

| | ENE | EW | NE | NS | NW | SubH |
|---|---|---|---|---|---|---|
| **FFM02U** | 42.6 %/57.4 % | 55.6 %/44.4 % | 40.8 %/59.2 % | 51.4 %/48.6 % | 46.9 %/53.1 % | 66.3 %/33.7 % |
| **FFM02L** | 27.4 %/72.6 % | 45.2 %/54.8 % | 32.6 %/67.4 % | 25.6 %/74.4 % | 21.7 %/78.3 % | 62.2 %/37.8 % |
| **FFM01 (z > −200 m)** | 28.3 %/71.7 % | 26.4 %/73.6 % | 18.0 %/82.0 % | 15.9 %/84.1 % | 35.0 %/65.0 % | 49.9 %/50.1 % |
| **FFM01 (−200 m > z > −400 m)** | 17.4 %/82.6 % | 20.6 %/79.4 % | 14.9 %/85.1 % | 9.3 %/90.7 % | 17.1 %/82.9 % | 32.7 %/67.3 % |

For all fractures, Figure 3-12 shows that Generation 4 fractures are most dominant in EW, SubH and ENE sets in FFM02U, which again are the sets with least normal stress. All sets see increased Generation 4 minerals in FFM02U. At depth the distribution of mineral generations is similar between each set with significant presence of Generation 2 minerals, corresponding to the Sveconorwegian orogeny. Generation 3 minerals have highest relative presence in the NE set. In open fractures Figure 3-13 shows these same patterns, but the dominance of Generation 4 minerals in EW, SubH and ENE sets is even more obvious, and there is a higher proportion of Generation 4 at depth. The relative increase of fractures with Generation 4 minerals provides a means to quantify the fraction of relatively young reactivated fractures in the near surface.

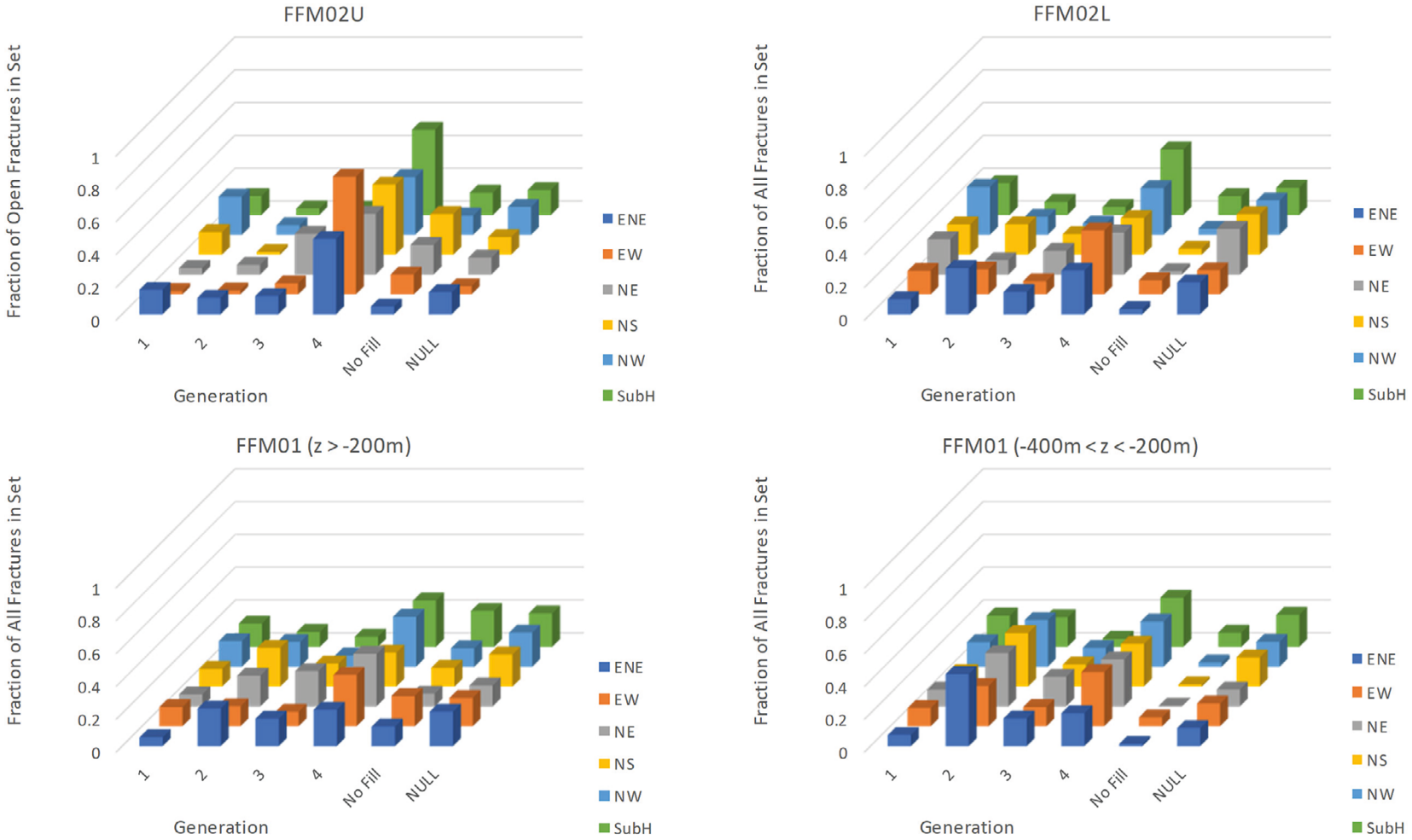


***Figure 3-12.*** *Fraction of all fractures with each mineral generation assignment in each orientation set. Fractures are taken outside deformation zones for each FFM domain.*

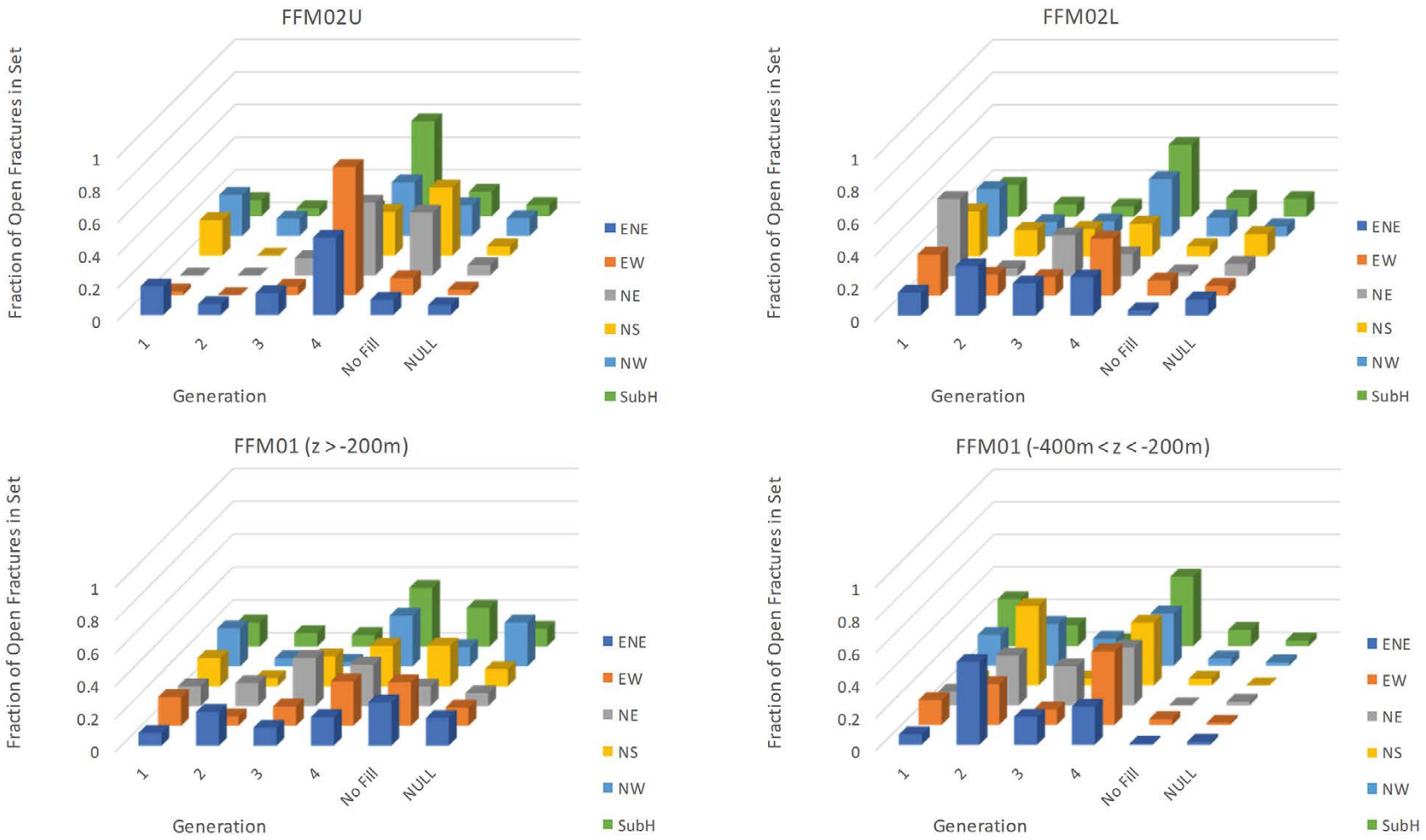


***Figure 3-13.*** *Fraction of open fractures with each mineral generation assignment in each orientation set. Fractures are taken outside deformation zones for each FFM domain.*

## 3.3 Fracture intensities

A key input to the DFN model is the fracture intensity since this has a strong control on connectivity. Figure 3-14 shows the fracture intensities by domain and set. This shows that EW, NE, NS and NW do not appear to have any obvious depth trend, while SubH has a very significant one (c 4 times higher in FFM02U compared to the lower part of FFM01) and ENE has a moderate one (c 2 times higher in FFM02U compared to the lower part of FFM01). The SubH set includes sheet joints. This would suggest that climate processes have had significant effects on the SubH and ENE fracturing in the near surface, leading to formation or extension of some fractures in these sets in relatively recent times. Fracture intensity can be enhanced both by creating new fractures or extending/changing the length of existing ones, requiring additional information to model the balance of these two effects.

Taken together Figure 3-14 and Figure 3-13 suggest that the SubH orientation set within FFM02U/L needs to be conceptualised as a superposition of ancient fractures with essentially uniform intensity with depth and younger or reactivated fractures potentially having different parameters. In particular, it is likely that the younger/reactivated sub-horizontal fractures will contain more long fractures and have larger apertures. Hence, the focus for calibrating the preliminary updated DFN model is on the size and transmissivity distributions of the sub-horizontal sets. Consequently, in the remainder of this document the older set is still termed "SubH", while the younger/reactivated sub-horizontal set is termed "Sheet joints".

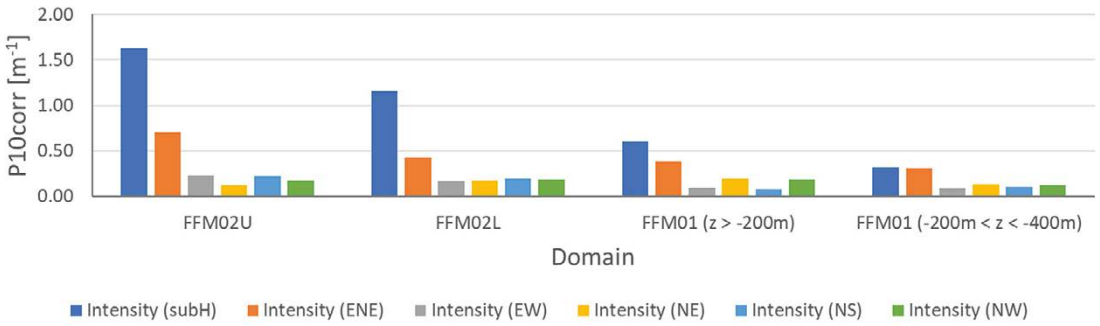


***Figure 3-14.*** *Average Terzaghi corrected fracture intensity $P_{10,corr}$ for each fracture domain outside modelled deformation zones aggregated over all boreholes. The subH set shown here contains both the ancient and reactivated (sheet joint) fractures.*

It is also interesting to review the variability in intensity between borehole intervals in the same domain. Figure 3-15 shows the variability in FFM02U and FFM02L. For FFM02U, there are some KFM holes with twice average intensity, and several HFM holes have significantly lower intensity. The HFM holes with lower intensity are to the west and south of FFM02, so may indicate regions of lower sub-horizontal fracturing, but may also be due to differences in determining open/sealed from image logs only in HFM boreholes compared to KFM holes where core can also be used. Likewise, the results for the cased part of some KFM, such as KFM06A, can be misleading because the shallow data lacks support from core. In FFM02L, the intensity also varies between about half and double the average. The intensity in FFM02U is consistently higher than that in FFM02L.

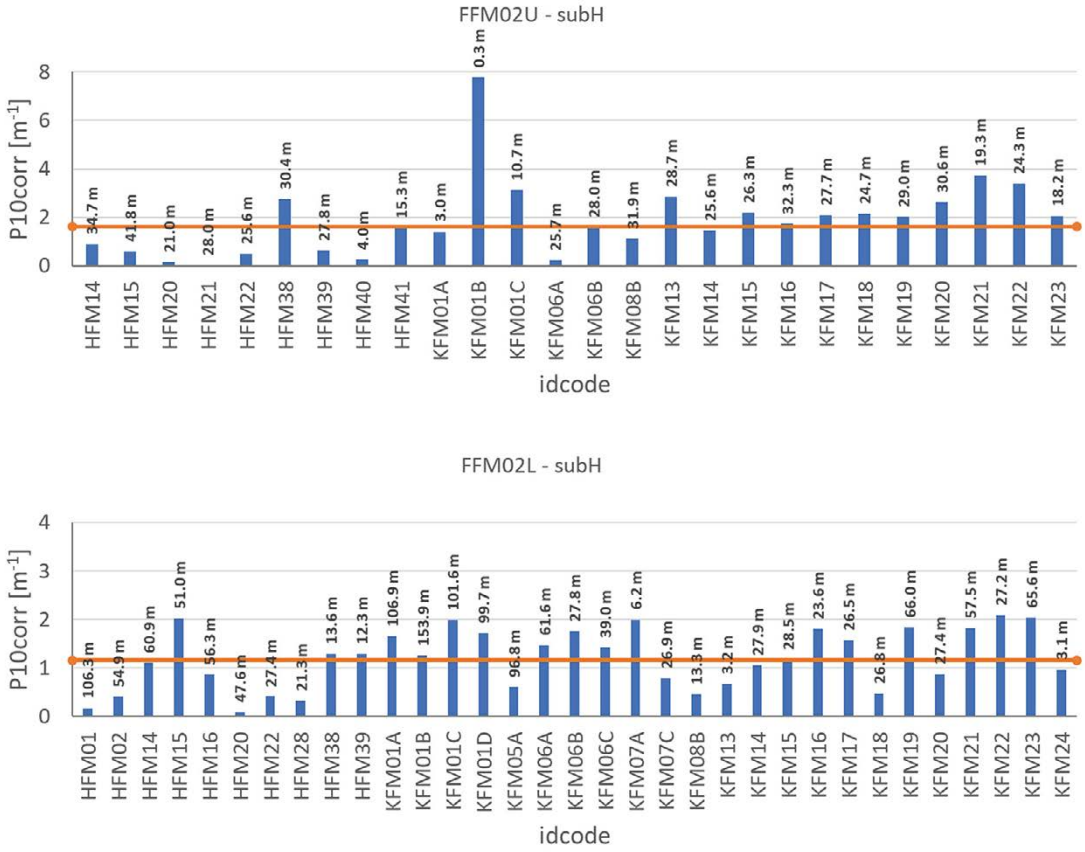


***Figure 3-15.*** *Variability between boreholes of Terzaghi corrected fracture intensity $P_{10,corr}$ of SubH open fractures in FFM02U and FFM02L outside modelled deformation zones. The orange line is the overall mean and the numbers show the length of interval.*

No analyses of possible correlations with this variability has been attempted here. Possible correlations include the curvature of the topography (Martel 2006, 2011, 2016, 2017), lithology, 3D stress distribution, or distance to deformation zones. It would be difficult to determine any potential correlation with any certainty because there are few holes across the wider area with data for the near surface of similar quality to the new data in the access area.

Figure 3-16 shows the consistently lower intensities in FFM01. The exceptions are the upper part of KFM01C, which is affected by intersection with the major zone ZFMA2, and the upper parts of KFM06A and KFM06A which are crossed by an unmodelled zone identified in the single hole interpretations. Hence, the main correlation of variability in intensity in the deeper sections is expected to be with proximity to deformation zones.

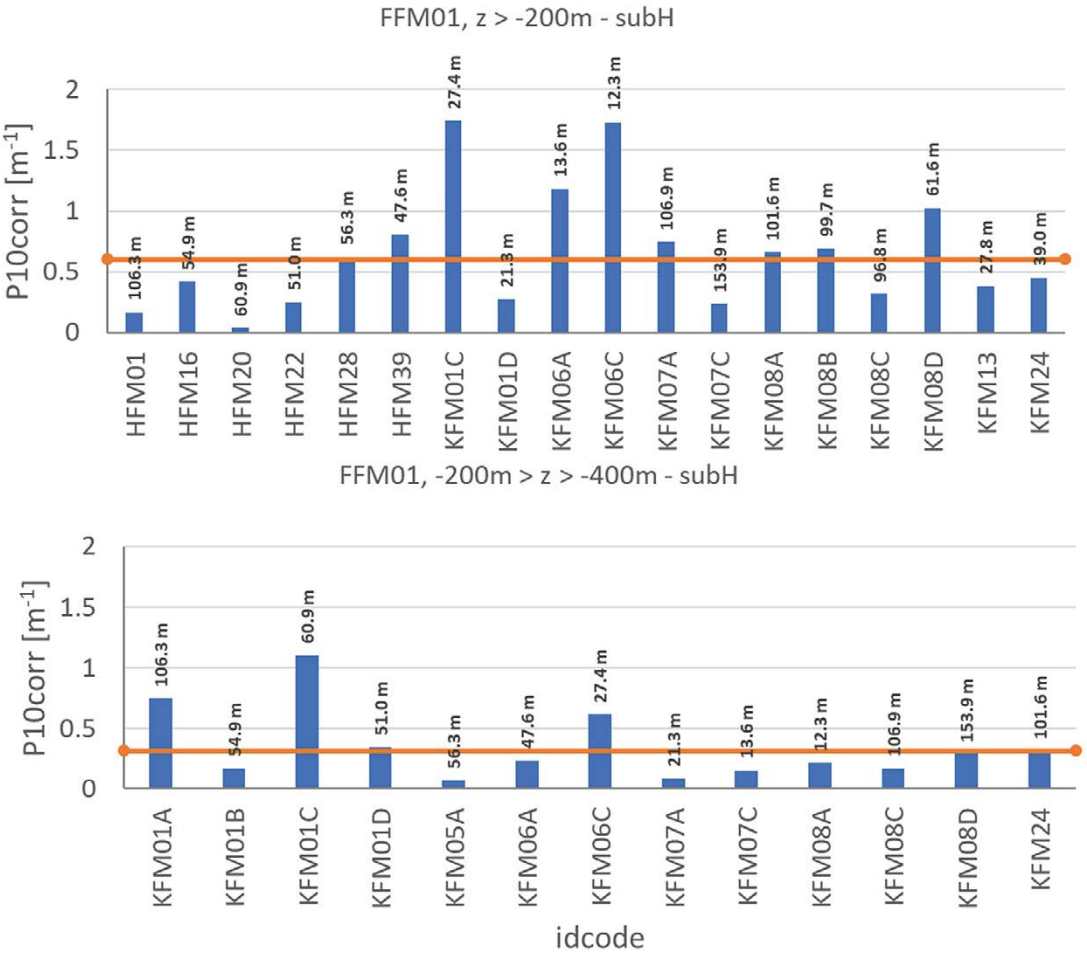


***Figure 3-16.*** *Variability between boreholes of Terzaghi corrected fracture intensity $P_{10,corr}$ of SubH open fractures in FFM01 outside modelled deformation zones. The orange line is the overall mean and the numbers show the length of interval.*

## 3.4 Proposed DFN recipe and alternatives for hydraulic simulations

To summarise, the following features of the preliminary updated DFN model can be noted:

- The rock inside the Forsmark lens is split into four domains inside FFM02U, FFM02L, FFM01/06 ($z > -200$ m), FFM01/06 ($-200$ m $> z > -400$ m), assuming FFM01 and FFM06 are statistically equivalent as in Follin et al. (2007).
- The rock outside the Forsmark lens is split into three domains inside: $z > -30$ m, $-30$ m $> z > -200$ m; $-200$ m $> z > -400$ m.
- Seven sets are modelled in FFM02 and the Outside domain ($z > -30$ m): Sheet joints, SubH, NW, NS, ENE, NE, NW, EW. With Sheet joints absent in the other domains.
- The same orientation model is used in all domains, see Table 3-4.
- The same size model is used for the subvertical sets as used for FFM02 in the F2.2 Hydro-DFN for all domains and depths.
- The size model for Sheet joints and SubH sets are calibrated against hydraulic measurements and varied between elevation region.
- Alternative size-transmissivity models for the Sheet joints and SubH sets to illustrate sensitivities.

The following subsections give further details.

### 3.4.1 Fracture domains and open fracture intensities

The fracture domains used are shown in Figure 3-17.

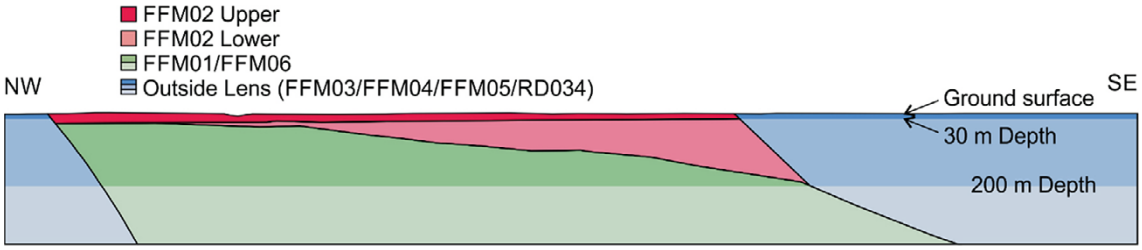


***Figure 3-17.*** *Example cross-section along the lens region showing the different fracture domains.*

The open fracture intensities are calculated for each set for each of these domains by approximating $P_{32}$ as the Terzaghi weighted linear density from the borehole data as described in Table 3-6. These provide an update of the recipe in Table C-1 of Follin (2008). The intensity for ancient SubH open fractures in FFM02 is assumed to equal to that in the upper part of FFM01/06 with the remaining total intensity for sub-horizontal fracturing assigned to the Sheet joints set. In FFM02U the intensity of open Sheet joint fractures is nearly twice that of SubH open fractures. The intensities of Sheet joints and SubH sets are similar and lower outside FFM02. The ENE set also has a strong depth trend outside FFM02, while the NW set has a high open fracture intensity at all depths outside FFM02/FFM01 compared to inside. Hence, the higher intensity of open NW fractures and lower intensity of open SubH and Sheet joints outside FFM02/FFM01 are the main structural differences between the focus volume for the repository and outside it.

**Table 3-6. Observed and modelled open fracture intensities in the SubH and Sheet joint sets. The regions are illustrated graphically on Figure 3-17.**

| | Total intensities from boreholes $P_{32}$ ($m^2/m^3$) | | | | | | | |
|---|---|---|---|---|---|---|---|---|
| **Domain** | **Total SubH** | **Ancient SubH** | **Sheet joint** | **NW** | **NS** | **ENE** | **NE** | **EW** |
| Outside Lens (z > −30 m) | 0.73 | 0.35 | 0.38 | 0.56 | 0.45 | 1.05 | 0.43 | 0.36 |
| Outside Lens (−30 > z > −200 m) | 0.65 | 0.65 | | 0.56 | 0.26 | 0.58 | 0.25 | 0.28 |
| Outside Lens (z < −200 m) | 0.38 | 0.38 | | 0.53 | 0.12 | 0.16 | 0.16 | 0.05 |
| FFM02 Upper | 2.00 | 0.78 | 1.23 | 0.21 | 0.27 | 0.87 | 0.15 | 0.28 |
| FFM02 Lower | 1.35 | 0.78 | 0.57 | 0.21 | 0.23 | 0.50 | 0.21 | 0.20 |
| FFM01/FFM06 (−30 > z > −200 m) | 0.78 | 0.78 | | 0.21 | 0.11 | 0.46 | 0.24 | 0.11 |
| FFM01/FFM06 (z < −200 m) | 0.34 | 0.34 | | 0.16 | 0.12 | 0.34 | 0.19 | 0.10 |

### 3.4.2 Fracture sizes

The starting point for the fracture size model is the power-law models of Table 11-22 in Follin et al. (2007). Initial tests indicated that the intensities given in Table 3-6 result in a fracture system with a lower number of connected flowing fractures than that observed. This indicates that more long fractures were needed to achieve sufficient connectivity. That is, a lower exponent to the power-law is required, and that the exponent should decrease with increasing elevation. The size distribution for the reactivated sub-horizontal fractures will be different to that of ancient sub-horizontal fractures at depth, the fractures having been extended, and that will affect the connectivity and hydraulic scaling behaviour in the near surface. One basis for determining an appropriate size distribution is from analysing the size distribution of sheet joints mapped on the wall of the inlet channel for the Forsmark power plant during its construction (Carlsson 1979), see Figure 3-20. The geological team digitised this old mapping data and produced a geological model of these sheet joints as discs centre of the inlet wall, see Figure 3-18 (blue). The geological team also manually interpreted a set of polygons joining borehole intersects with sheet joints, see Figure 3-18 (green).

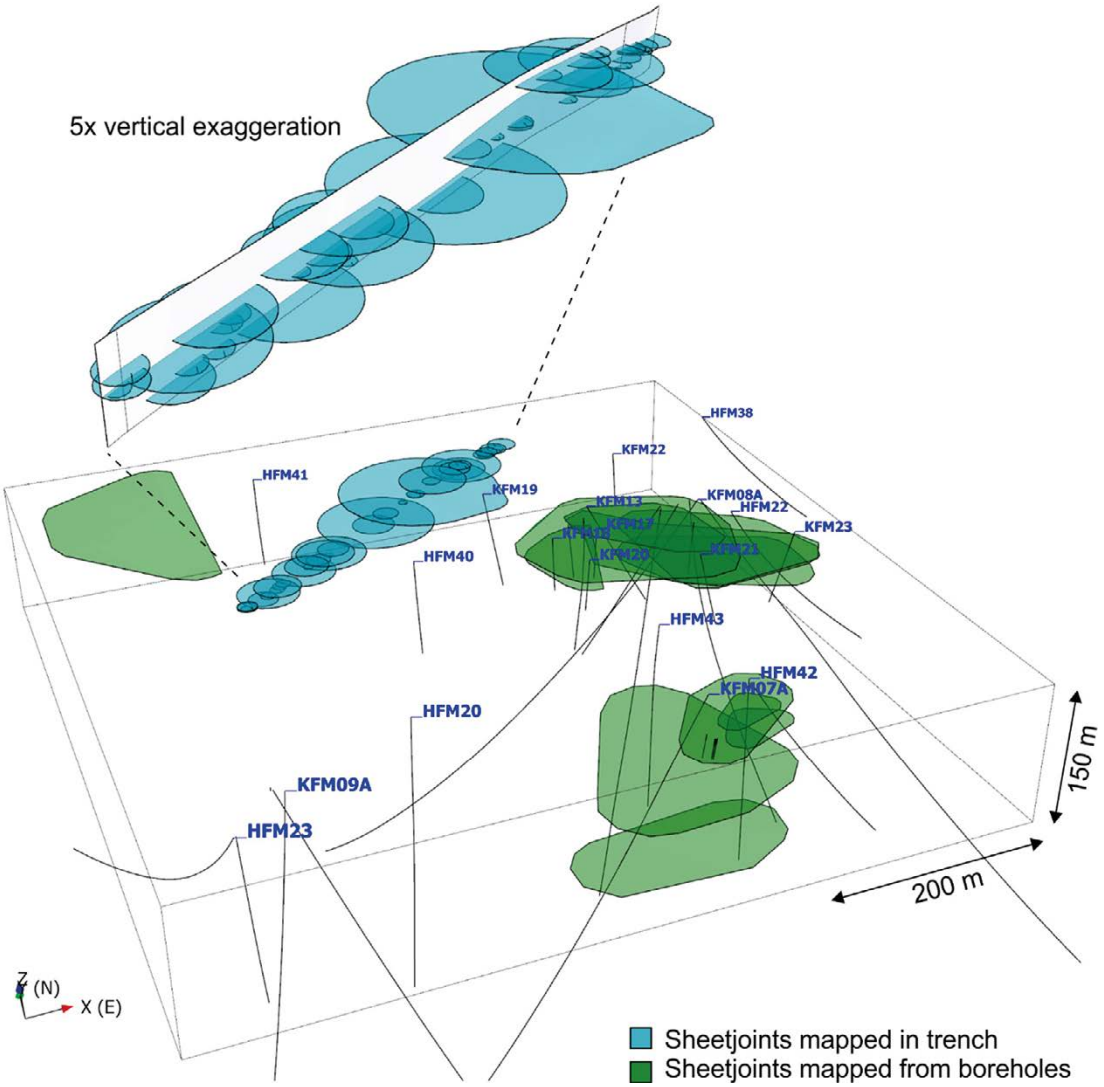


***Figure 3-18.*** *3D view of the deterministically modelled sheet joints used to provide the size distribution shown in Figure 3-20.*

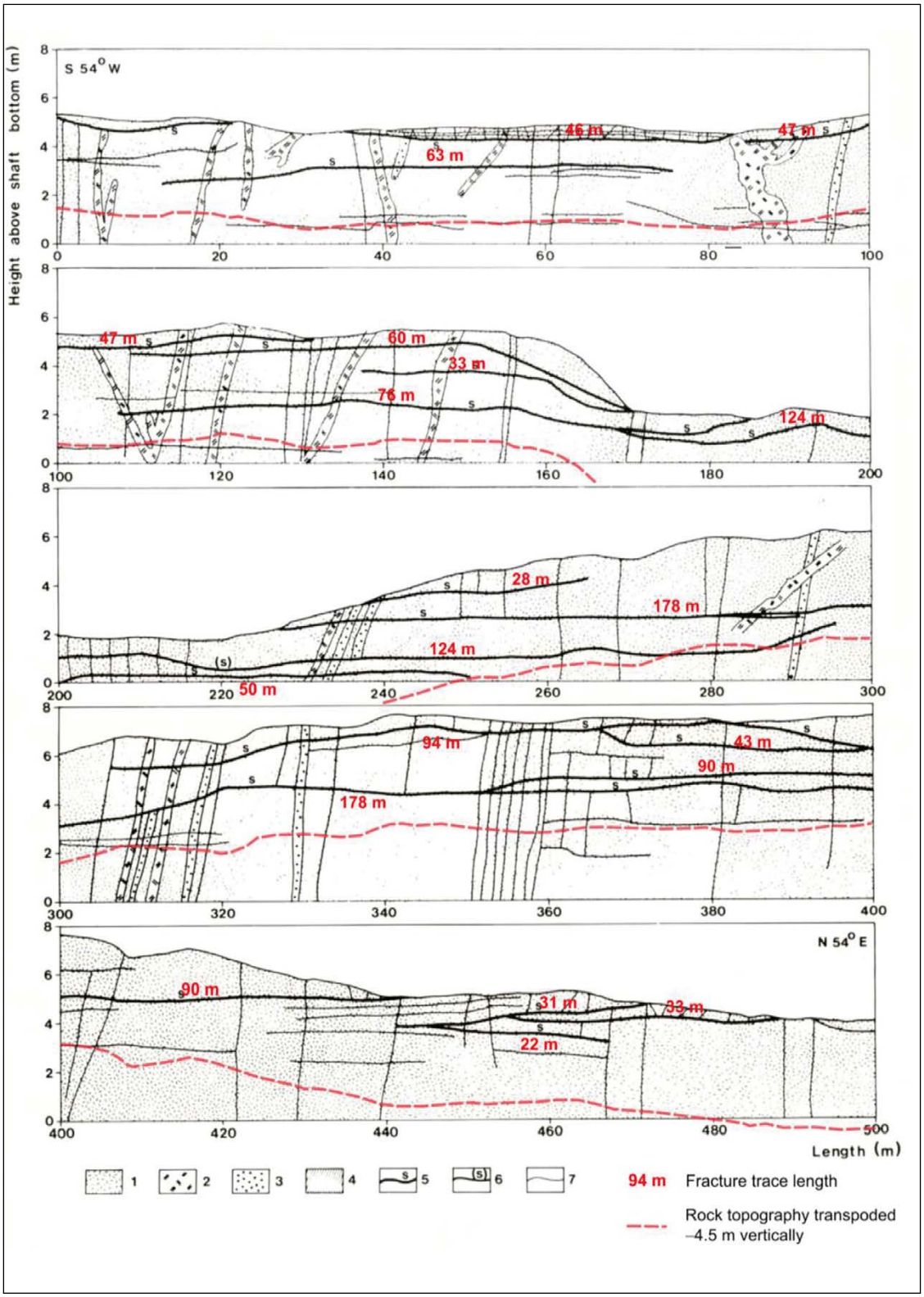


***Figure 3-19.*** *Cross-sections from the inlet water channel at Forsmark (Carlsson 1979) with mapped sheet joints used to digitise a geological model of sheet joints in this area.*

The inlet channel provides the larger of these two datasets, so this was used to fit size distributions to the trace map as either a power-law or lognormal distribution, see Figure 3-20. Both distributions provide a reasonable fit, with the lognormal giving the closer statistical match, but the power-law match is also considered given the inlet mapping is subject to censoring effects (La Pointe et al. 1993). The derived parameters are given in Table 3-7 with three possible cases interpreted: the two fitted models and a sensitivity case with a log-normal distribution of higher mean and spread. These different cases are termed variants. The fracture size models used for each set are given in Table 3-8. When generating the DFN model over the facility-scale area, fractures are generated everywhere with $r_{min}$ = 10 m and $r_{max}$ = 300 m, and then additional fractures are created within a cylinder of radius 20 m around every borehole with fracture radii in the range $r_{min}$ = 0.56 m to 10 m, so as not to under-predict connectivity around the boreholes.

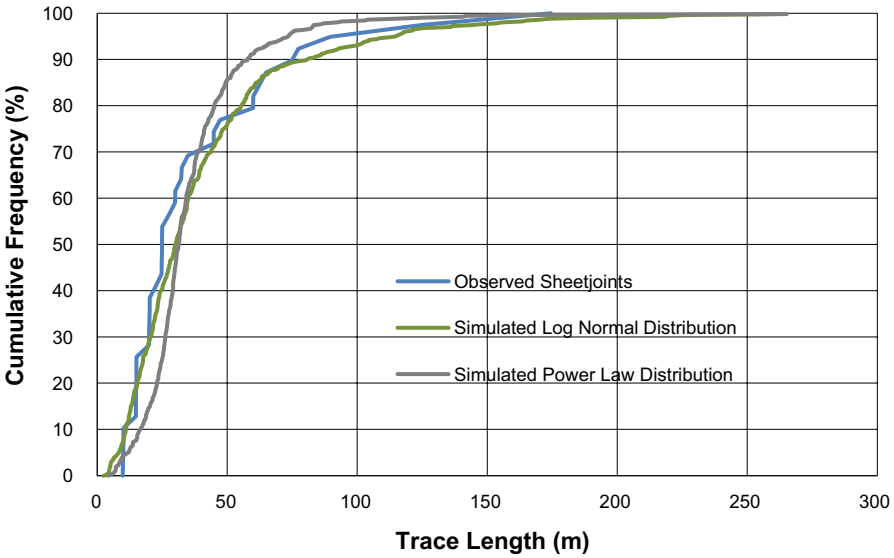


***Figure 3-20.*** *Graph showing the observed and fitted size distributions of the traces in the inlet.*

**Table 3-7. Parameters for the three difference fracture size models. The calibration parameters were calculated using the fits shown in Figure 3-20.**

| | Parameters used | Based on |
|---|---|---|
| Variant 1 | Log-normal<br>Mean: 14.7<br>Std: 11.9 | The best fit for the sheet joints observed in the inlet. |
| Variant 2 | Power-law<br>$r_0$: 14.6<br>$k_r$: 2.2 | $r_0$ fitted for the sheet joints observed in the trench, $k_r$ adjusted (from 2.5) to produce large fractures. |
| Variant 3 | Log-normal<br>Mean: 38.2<br>Std: 33.9 | Using the best fit for the sheet joints observed in the inlet but using the trace length values as inputs for the equivalent radius i.e. approximately doubled. This aims to simulate the coalesce of sheet joints to form longer structures, as shown in green in Figure 3-18. |

**Table 3-8. Fracture size models used for each set across all domains.**

| Set | Distribution | Parameter 1 | Parameter 2 |
|---|---|---|---|
| Sheet joint | V1: Log-normal | $\mu = 14.7$ | $\sigma = 11.9$ |
| | V2: Power-law | $r_0 = 14.6$ | $k_r = 2.2$ |
| | V3: Log-normal | $\mu = 38.2$ | $\sigma = 33.9$ |
| Ancient SubH | Power-law | $r_0 = 0.038$ | $k_r = 2.5$ |
| NW | Power-law | $r_0 = 0.038$ | $k_r = 3.2$ |
| NS | Power-law | $r_0 = 0.038$ | $k_r = 2.75$ |
| ENE | Power-law | $r_0 = 0.038$ | $k_r = 2.62$ |
| NE | Power-law | $r_0 = 0.038$ | $k_r = 2.62$ |
| EW | Power-law | $r_0 = 0.038$ | $k_r = 3.4$ |

### 3.4.3 Model visualisations

The DFN model was created using FracMan 7.8. Visualisation of the Variant 1 model (Log-normal sheet joints) on a NW–SE slice (coloured by set and transmissivity, see Chapter 4) and NE–SW slice (coloured by transmissivity) is shown in Figure 3-21 for fractures with radius > 10 m. The high intensity sub-horizontal fracturing of sheet joints in FFM02 is very apparent and continues across the upper 30 m of bedrock. Fracturing is much sparser below this and sub-vertical fractures have decreasing transmissivity with depth.

The three variants of fracture size models for sheet joints are compared in Figure 3-22. The lower exponent used for the power-law by chance produces some longer sheet joints, whereas the log-normal has a narrower range of medium size structures. The third variant creates fewer, but longer sheet joints distributed as a log-normal.

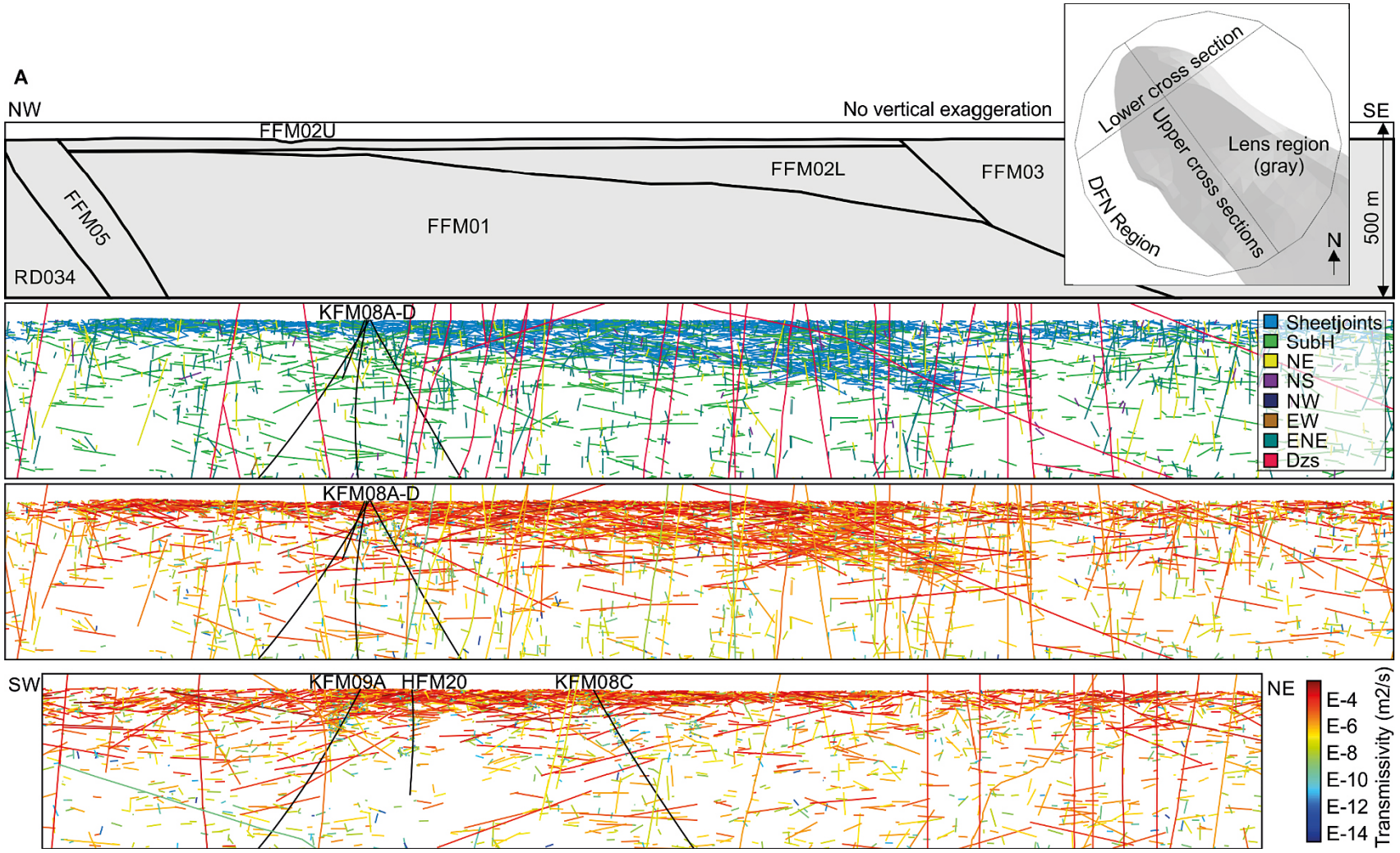


***Figure 3-21.*** *Cross-sections across the DFN region for the Variant 1 model showing fracture traces coloured by set and transmissivity.*

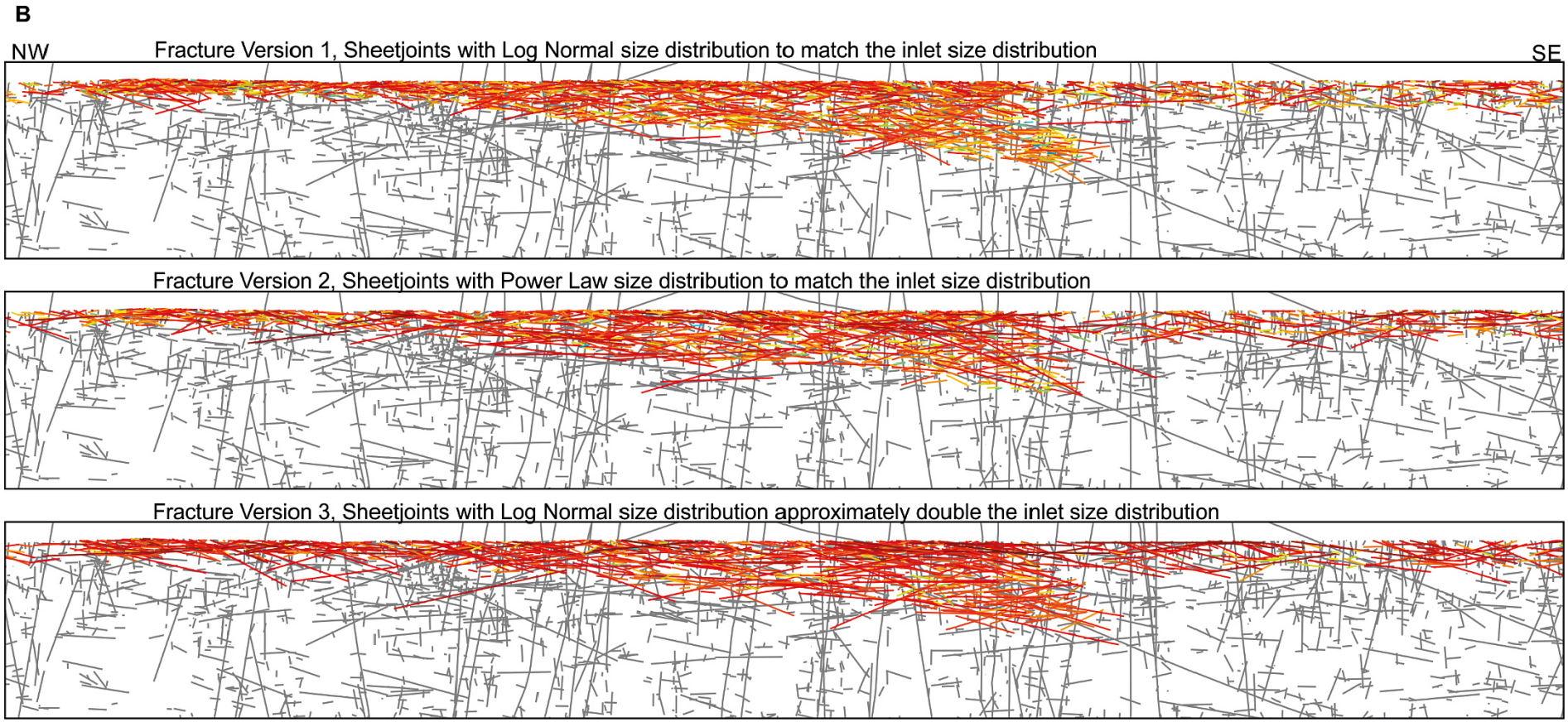


***Figure 3-22.*** *Cross-sections comparing the three DFN variant of sheet joints with the sheet joints coloured by transmissivity.*

# 4 Calibration of hydraulic properties and hydrogeological property model

This chapter describes the hydraulic parameterisation of the DFN model and how these parameters are calibrated against the combined hydraulic data from PFL-f and impeller flow logging. It also explains how these parameters are extrapolated over the catchment-scale model and upscaled to provide an ECPM hydrogeological property model.

## 4.1 Methodology for fracture hydraulic description

In Hydro-DFN F2.2 (Follin et al. 2007) a semi-correlated model between fracture transmissivity was assumed with the parameters of coefficient and exponent fitted for each set, domain and elevation region adjusted empirically until the simulated distribution of specific capacity within each category matched the observed distribution. The data support for the parameterisation of some of these categories is limited and hence uncertain.

An alternative approach is to use a hydromechanical coupling relationship to predict variations in transmissivity with depth, orientation and domain through its relationship to variations in the effective stress apparent on each fracture plane. Such relationships have been considered to explain variations in transmissivity of deformation zones since SDM-Site (Follin and Stigsson 2013), and used in recent DFN modelling of Olkiluoto (Hartley et al. 2018). It is therefore appropriate to prototype this approach here for parameterising the transmissivity of fractures as mechanistic model for extrapolating transmissivity distributions to depth and domains outside the focused investigation area where rock stresses are lower in magnitude.

Hydromechanical coupling models generally work in terms of aperture, since it is the compliance of fracture aperture that is measured in laboratory rock mechanics tests. The first building block of the model is the scaling of aperture with fracture size.

The scaling of aperture with the size of a fracture can be expected on mechanical grounds, elastic theory, with greater dilation for a larger size of opening. A power-law scaling for mechanical aperture is a suitable working assumption:

$$e_m = aL^b \qquad \text{Equation (4-1)}$$

with $b$ around 0.5 (Olson 2003, Schultz et al. 2008a, b, Klimczak et al. 2010) but can be 1.0 for fractures with shear displacement (see Eshelby 1957, Schultz et al. 2008a, b). The exponent can be inferred from simulating the shape of distribution of specific capacity of water conducting fractures against that measured, although in that case shape of flow distribution is also affected by other parameters such as fracture size scaling.

The aperture also changes with normal and shear loads, whether that be with the orientation of a fracture relative to an anisotropic stress field, with depth, or with temporal changes due to construction of the repository or the advance and retreat of ice sheets. The stress on a fracture is defined in terms of the normal stress, $\sigma_n$, and shear stress, $\tau$, incident on the plane calculated from the direction cosines ($l$, $m$, and $n$) normal to the plane for a stress field with $\sigma_H$ as the major principal stress (horizontal), $\sigma_h$ as the intermediate principal stress (horizontal), and $\sigma_v$ as the minimum principal stress (vertical),

$$\sigma_n = l^2\sigma_H + m^2\sigma_{h+} n^2\sigma_v \qquad \text{Equation (4-2)}$$

$$\tau = [(\sigma_H - \sigma_h)^2 l^2 m^2 + (\sigma_h - \sigma_v)^2 m^2 n^2 + (\sigma_H - \sigma_v)^2 l^2 n^2]^{\frac{1}{2}} \qquad \text{Equation (4-3)}$$

$$\begin{aligned} l &= \sin(dip)\cdot\sin(\text{azimuth to maximum stress}) \\ m &= \sin(dip)\cdot\cos(\text{azimuth to maximum stress}) \\ n &= \cos(dip) \end{aligned} \qquad \text{Equation (4-4)}$$

The effective normal stress, $\sigma'_n$, is then given by the

$$\sigma'_n = \sigma_n - P \qquad \text{Equation (4-5)}$$

where P is the hydrostatic pressure. Fractures oriented orthogonal to the maximum horizontal stress experience highest normal stress, and those oriented horizontal to it experience the least normal stress. All three principal stresses and pressure generally increase with depth, so that fractures experience increasing normal stress with depth. Gently dipping fractures near ground surface experience the highest shear to normal stress ratios, making them more susceptible to shear displacement.

A suitable hydromechanical model for hydraulic aperture with a hyperbolic dependence on effective normal stress (Goodman et al. 1968, Willis-Richards et al. 1996) is:

$$e_h = e_{hr} + \frac{1}{f}\left(\frac{Ae_{m0}}{1 + \frac{9\sigma'_n}{B}} + e_s\right) \qquad \text{Equation (4-6)}$$

Where $A$ is scaling factor, $e_{m0}$ is the unstressed mechanical aperture, $\sigma'_n$ is the effective normal stress, $B$ is the 90 % closure stress, which can be related to fracture normal stiffness, $f$ is a fracture surface roughness factor, and $e_s$ is the shear slip induced dilation. The change in aperture due to shear is a function of the shear displacement, $u_s$, and effective dilation angle $\phi'$:

$$e_s = u_s \tan \phi' \qquad \text{Equation (4-7)}$$

$A$ can be set to 1 for the majority of fractures but increased for some subset of fractures with a distinctly high transmissivity, such as those in highly transmissive deformation zones, or at high shear stress/low normal stress in the near surface. Here, the coefficients are simplified and equivalent radius, $r$, of fracture discs used rather than length, with $b = 0.5$:

$$\frac{Ae_{m0}}{f} = A' r^{0.5} \qquad \text{Equation (4-8)}$$

The appropriateness of such a model can be tested by plotting the expected shear and normal stress on each observed fracture plane on a Mohr diagram given its orientation and location, along with a spatial model for the stress tensor, and examining the stress conditions on the water conducting fractures detected by PFL-f tests, see Figure 4-1.

The stress field used in this study is the 1D stress profile developed for SDM-Site inside FFM02/ FFM01/FFM06 and that for FFM03 outside the Forsmark tectonic lens, see Table 4-1. The stress field used in FFM03 is similar to that used in SDM-PSU for the SFR area (SKB 2013). The maximum horizontal stress orientations are consistent (NW) but the magnitudes are much higher inside the lens. Recently, an updated 3D stress field has been derived for Forsmark using the F2.3 deformation zone model (Hakala et al. 2019). In these prototyping tests, the simple 1D stress fields were used.

Figure 4-1 demonstrates that the majority of flow occurs in fractures under relatively low normal stress, typically where the effective normal stress is below $(\sigma_{v+} \sigma_h)/2$. In FFM01, i.e. at depth it is low normal stress that is the most useful in predicting a fracture possibility to flow, while near the surface whether a fracture is likely critically stressed could also be considered. That is not to say that all fractures subject to low normal stress flow, many do not likely because they are not connected. There are some anomalous flowing fractures at seemingly higher normal stress. However, this might be an artefact of the linking process where a measured flow has been linked to the nearest open fracture, whereas they maybe alternative candidates also within the window of possibilities with an orientation giving lower stress. It would be a worthwhile process to review how many of these anomalies would be removed if the linking were carefully re-examined for these few anomalies.

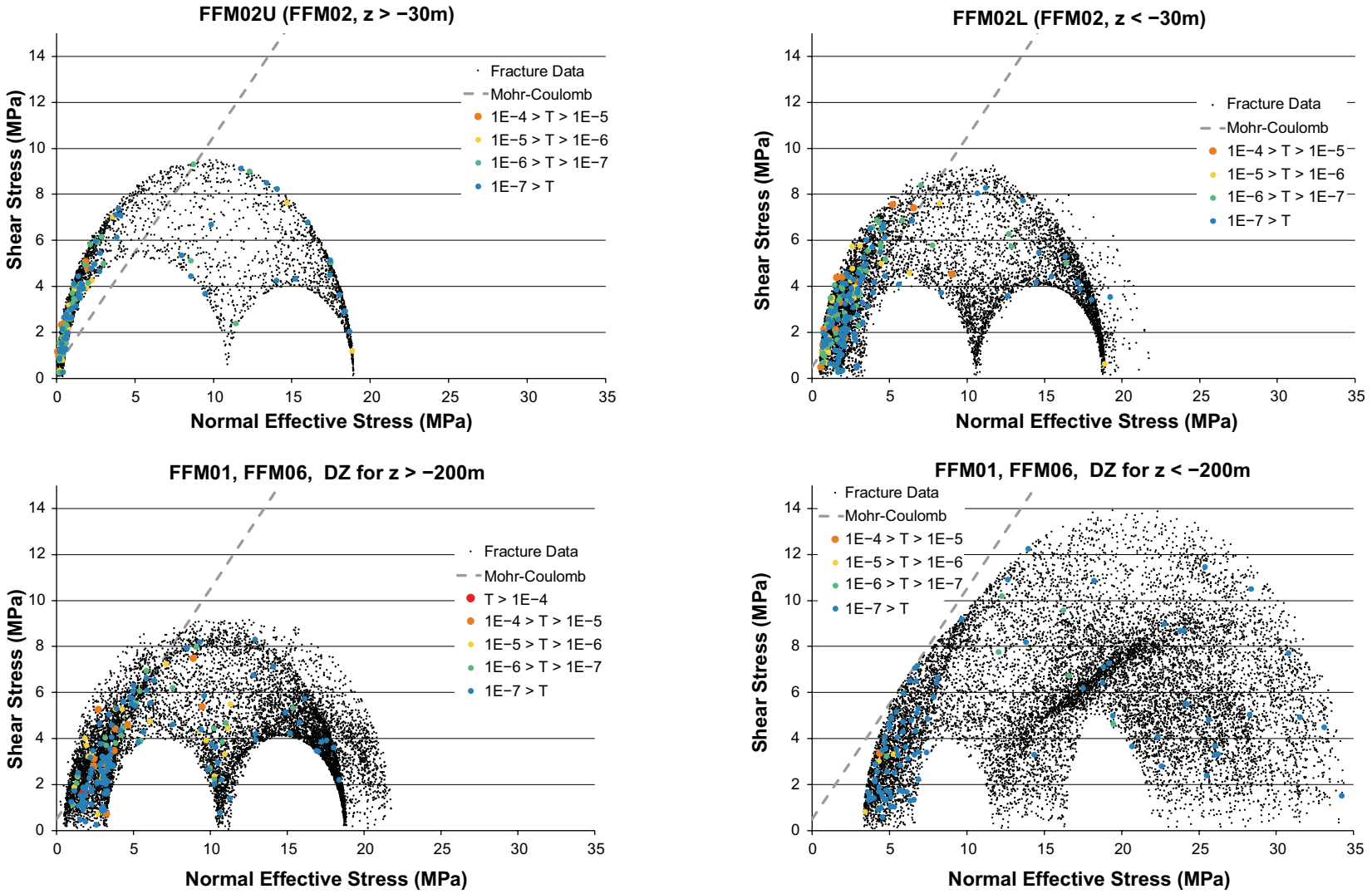


***Figure 4-1.*** *Mohr plots for each observed fracture in FFM02U, FFM02L, FFM01/FFM06, outside deformation zones with transmissive fractures overlain. A Mohr-Coulomb envelope with coefficient of sliding friction = 1 and cohesion of 0.5 MPa is shown for illustration.*

**Table 4-1. Stress field used from Tables 6-7 to 6-9 in Glamheden et al. (2007), and Table 6-10 for outside.**

| FFM02/FFM01/FFM06 | z > −150 m | −150 > z > −400 m | z < −400 m |
|---|---|---|---|
| Major horizontal stress, $\sigma_H$ | 19 − 0.008z MPa | 9.1 − 0.074z MPa | 29.5 − 0.023z MPa |
| Minor horizontal stress, $\sigma_h$ | 11 − 0.006z MPa | 6.8 − 0.034z MPa | 9.2 − 0.028z MPa |
| Vertical stress, $\sigma_h$ | −0.0265z MPa | −0.0265z MPa | −0.0265z MPa |
| Major horizontal stress trend | 145º | 145º | 145º |
| **Outside Lens** | **z > −250 m** | | |
| Major horizontal stress, $\sigma_H$ | 5 − 0.075z MPa | | |
| Minor horizontal stress, $\sigma_h$ | 2.5 − 0.0375z MPa | | |
| Vertical stress, $\sigma_h$ | −0.0265z MPa | | |
| Major horizontal stress trend | 145º | | |

Given that low normal stress appears more important for transmissivity than shear stress, the shear component Equation (4-7) is neglected, and the coefficient of hydraulic aperture is formulated as:

$$\log_{10}(A') = \log_{10}(2 \cdot 10^{-5}) + 0.6N(0,1,-2,2) \quad \text{Equation (4-9)}$$

In-plane Transmissivity is then calculated as:

$$T = \frac{\rho g}{12\mu} e_h^3 \quad \text{Equation (4-10)}$$

(Witherspoon et al. 1980), where $\rho$ is fluid density, $g$ is gravitational acceleration, is $\mu$ if the fluid viscosity.

This results in a semi-correlated model between transmissivity and fracture size, $r$. The coefficient in Equation (4-9) is chosen to give the correct magnitude of flows, while the spread given by the normal distribution gives some additional spread beyond that provided by the square root dependence on size, Equation (4-8). The dependence on stress comes from the hyperbolic function Equation (4-6), with the 90 % closure stress $B$ being set to 30 MPa to give the observed string depth dependence in transmissivity.

Storativity follows a relationship from (Hartley and Roberts 2013):

$$S = 0.001\sqrt{T} \quad \text{Equation (4-11)}$$

### 4.1.1 Modelling hydraulics of deformation zones

The methodology used to assign transmissivities to the deformation zone surfaces is a combination of that used in F2.2 (Follin et al. 2007, Follin and Stigsson 2013) as follows:

- Determine the borehole intersects of each deformation zone;
- Aggregate all transmissivity measurements within the intersect;
- If there are more than 1 measurements:
  - Calculate the effective normal stress on the plane at the intersect depth from the compliance model given above and calculate the equivalent hydraulic aperture at z = 0. This essentially removes the expected depth trend.
  - Interpolate the reference hydraulic aperture over plane using inverse distance weighting (power 2) across the ZFM;
  - Reapply the compliance model with stress to calculate the reduction in transmissivity with depth.
- If zero or 1 intersections: as above but with a constant reference hydraulic aperture.

This method provides a mechanistic method for including depth variations but conditioned to the measured values where available.

Figure 4-2 shows the depth variations in transmissivity for each ZFM drawn as a separate curve. This shows that transmissivity decreases by about 2 to 2.5 orders of magnitude in the top 1 000 m and another order of magnitude in the next 1 000 m (there is no data below −1 000 m, so this part is extrapolated). The variations between zones comes from the different orientations relative to the stress field and the variations in measurements. A visualisation of how this implemented on the 3D model is shown in Figure 4-3. It is seen that NW and gently dipping zones have higher transmissivity due to the low normal stress and some zones have a low transmissivity due to low transmissivity measurements in the shallow bedrock.

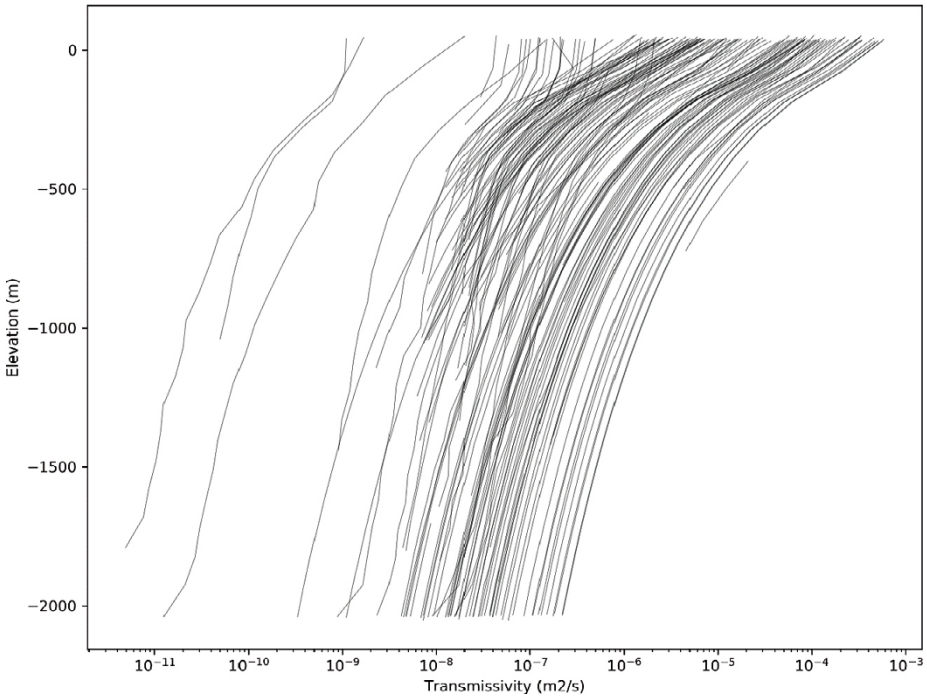


***Figure 4-2.*** *Graph showing elevation versus transmissivity (mean per 100 m depth interval) for the deformation zones.*

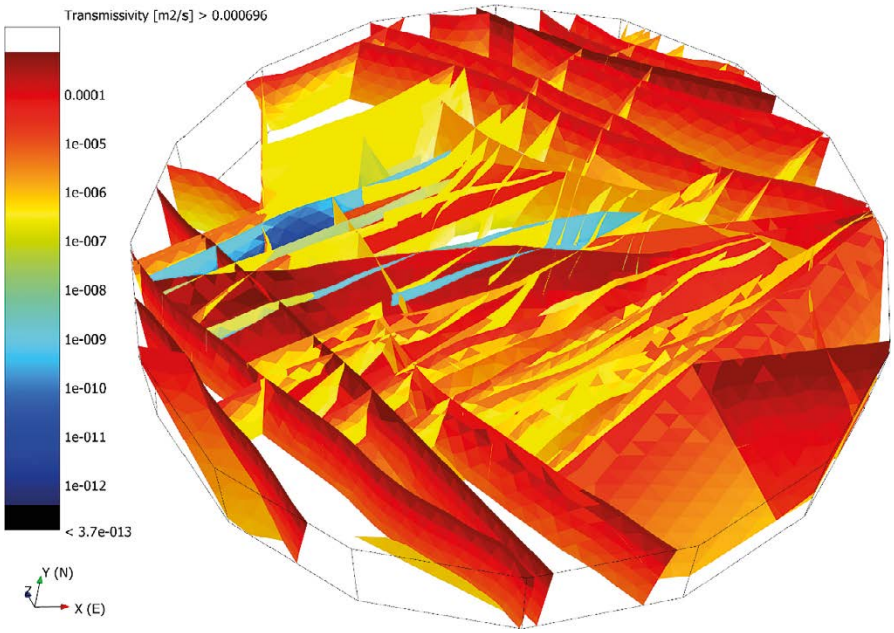


***Figure 4-3.*** *3D view of the ZFM surfaces coloured by transmissivity within the DFN facility-scale model down to −440 m elevation. The location of this region is shown on Figure 2-1.*

## 4.2 Modelling of single-hole hydraulic tests

### 4.2.2 DFN simulations and calibration

The workflow for the hydraulic calibration of the Forsmark DFN model is made as follows using FracMan 7.7, see Figure 4-4:

1. Create the DFN in the facility-scale region shown in Figure 2-1 down to −440 m elevation including deformation zones and fractures.
2. Open fractures are generated between radius 10 m and 300 m throughout the region according to the scaling model Table 3-8 and intensity for this size range.
3. Extra small-scale fractures radius 0.56 m to 10 m are generated in cylinders of radius 20 m around the simulated boreholes.
   - Percussion holes: HFM20, HFM21, HFM22, HFM38, HFM39, HFM40.
   - Cored holes: KFM01A, KFM01D, KFM05A, KFM06A, KFM07A, KFM07C, KFM08A, KFM08C, KFM08D, KFM14, KFM15, KFM16, KFM20, KFM21, KFM22, KFM23, KFM24.
4. Cylindrical “cut-out” models around each borehole of radius 250 around the horizontal footprint of the hole are created to simulate steady-state drawdowns and inflows to each hole.
5. The simulations are performed by gridding the fractures in each borehole DFN and steady-state constant-density flow calculated. The boundary conditions are zero head on the sides, 10 m of drawdown in the hole. No flow on top and bottom. The inflows at each fracture intersecting the borehole and total flow are calculated.
6. 10 realisations of the DFN models are considered for 23 holes simulated, yielding 230 flow simulations per model iteration.
7. The ensemble of flows over the 230 simulations are collated by domain or hole and compare with metrics of the measurements.
8. Parameters are adjusted until a match is achieved. The main parameters adjusted are those of the size distribution and the transmissivity parameterisation.
9. Many iterations were tried resulting in the given parameters. Three alternative size models for the sheet joints are presented here to illustrate some of the main sensitivities to model assumptions.

The metrics used to compare the modelled are simulated flow distributions are:

- The magnitudes of total flows for each borehole for each domain (FFM02U, FFM02L, FFM01 ($z > -200$ m), FFM01 ($-200 > z > -400$ m)).
- The distribution of specific capacities for each orientation set (SubH, NW, NS, ENE, NE, EW) for each domain (FFM02U, FFM02L, FFM01 ($z > -200$ m), FFM01 ($-200 > z > -400$ m)) as ensembles over the cored holes with PFL-f tests.

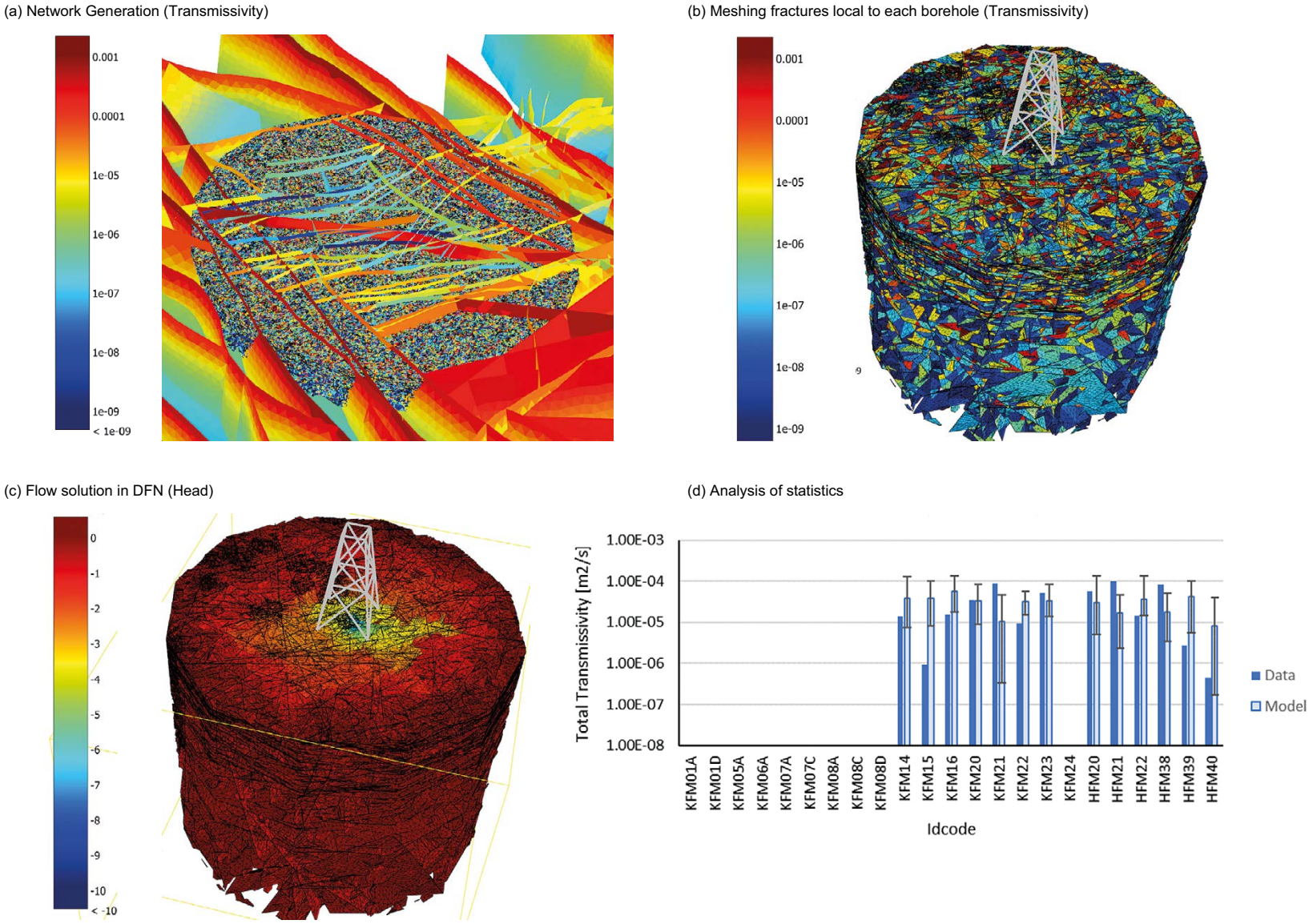


***Figure 4-4.*** *Workflow of performed PFL simulations: generation of local-scale model; gridding of borehole-scale model; inflow simulation; and calibration.*

Figure 4-5 and Figure 4-6 show example comparisons of the total flows across each hole and domain for the Variant 1 size model for sheet joints. The spread over ten realisations often captures the measured flow, and the pattern of reduction in total flow with depth is well captured. This three to four orders of magnitude change in total flows with depth was difficult to achieve using an integrated hydro-structural model. The ingredients necessary to achieve it are:

- The dominance of sub-horizontal fracturing and the two components of ancient fractures and sheet joints with different size models and hence sufficient connectivity.
- The hydromechanical effects of the high stress and stress anisotropy giving a depth trend and anisotropy in transmissivity.
- A hydraulic choking effect due to a lack of connectivity of large and transmissive fractures that becomes stronger with depth.

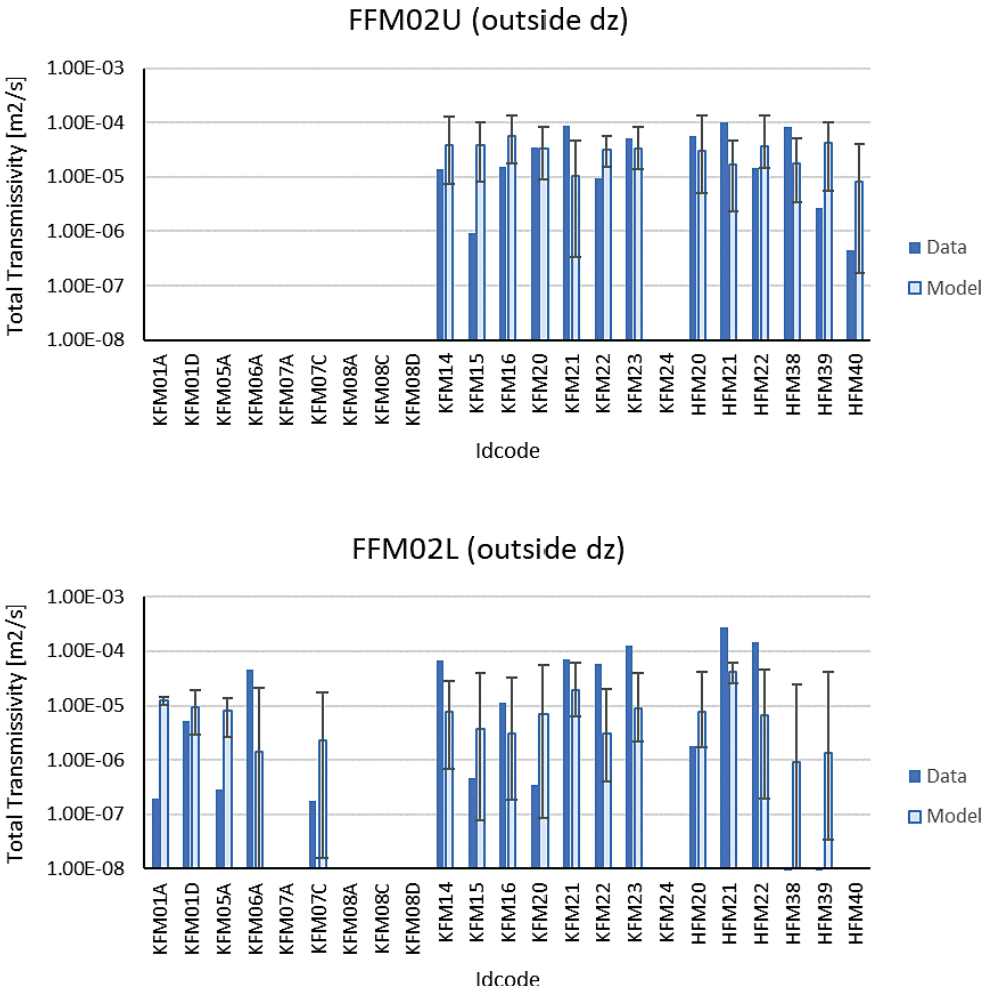


***Figure 4-5.*** *Geometric mean values for Total Q/s outside deformation zones and inside unit FFM02 for 10 realisations for DFN Model Variant 1. Error bars indicate the minimum and maximum of 10 realisations. Data is shown in dark blue.*

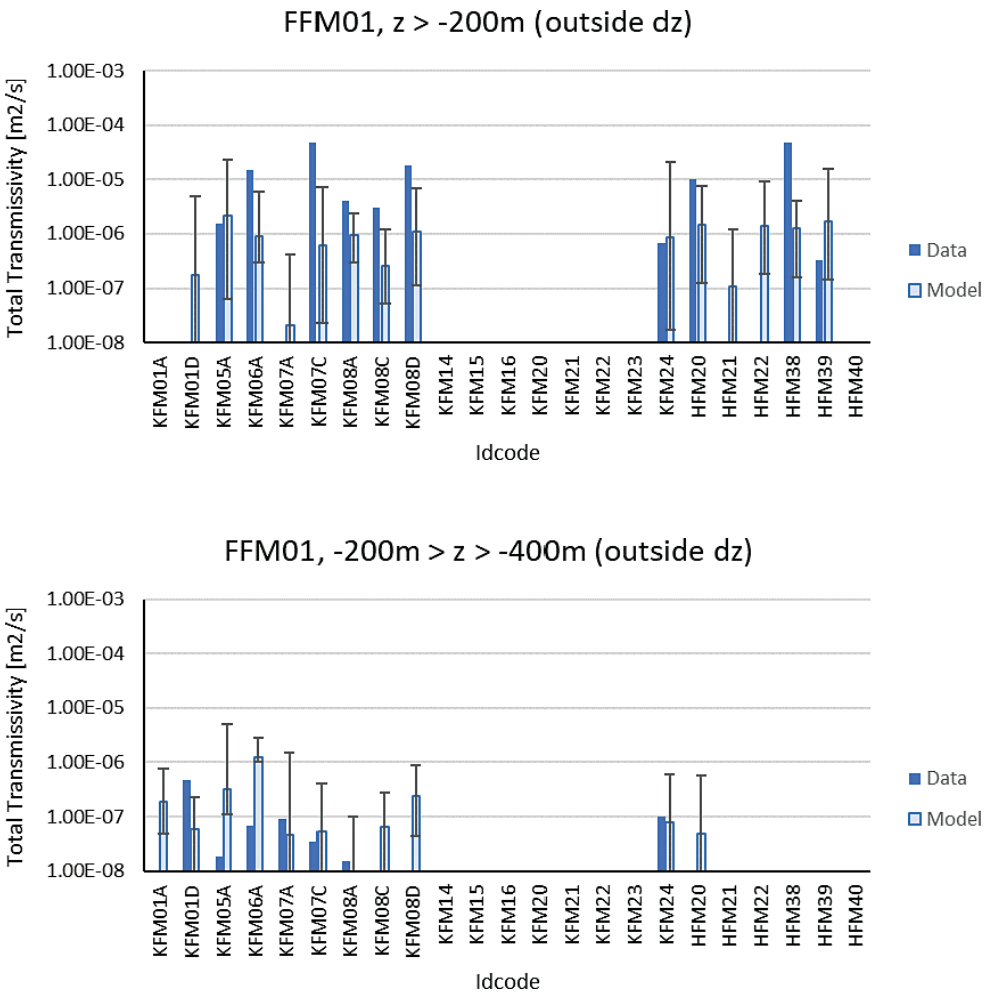


***Figure 4-6.*** *Geometric mean values for Total Q/s outside deformation zones and inside unit FFM01 for 10 realisations for DFN Model Variant 1. Error bars indicate the minimum and maximum of 10 realisations. Data is shown in dark blue.*

The last of these points is illustrated in Figure 4-7, which shows the relative choking of flow as the specific capacity, flow-rate over drawdown, versus transmissivity. Points below the diagonal line becoming increasingly choked either by lack of connectivity or only being connected by lower transmissivity fractures, such that their potential flow-rate is not met due to a lack of supply of water from the network. The highest potential flows are particularly susceptible to this second choking mechanism. It can be seen that the degree of choking of high transmissivity fractures increases with depth, which is necessary to explain what is seen in the measurements.

Two main challenges existed when finding a size distribution for the sheet joints in each calibration; achieving high connectivity in the near surface and low connectivity at depth, and also a spread of transmissivity to give the very wide distribution of measured flows shown in the upper plot of Figure 4-8 for SubH fractures. Figure 4-8 shows a good match to the flow distribution in SubH fractures (ancient + sheet joints in FFM02) in each depth and the very few flows in other sets (see also Figure 4-9). The total flows are typically the result of 1–3 relatively high transmissivity fractures, and consequently are sensitive to the transmissivity and connectivity of these few fractures. The data is sometimes more variable than the simulations, suggesting the real system is even more discrete and variable. The model overpredicts the number of flows in the $10^{-6}$ to $10^{-5}$ $m^2/s$ transmissivity range. However, these flows are secondary contributors to the total flow in the hole which is typically dominated by the few higher transmissivity structures described above.

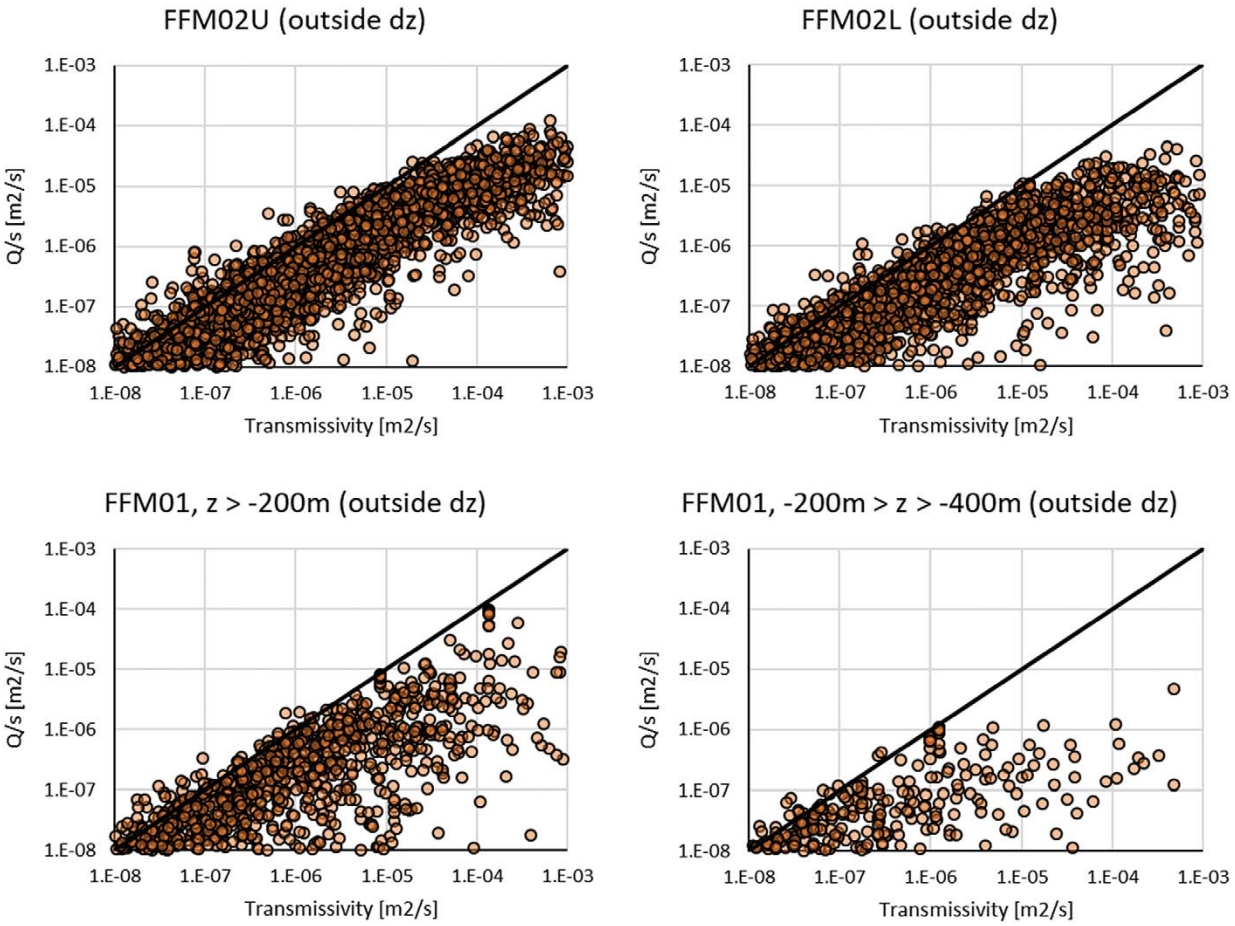


***Figure 4-7.*** *Transmissivity Vs Q/s (10 realisations of DFN Model V1) outside deformation zones, showing the hydraulic choking in each rock unit.*

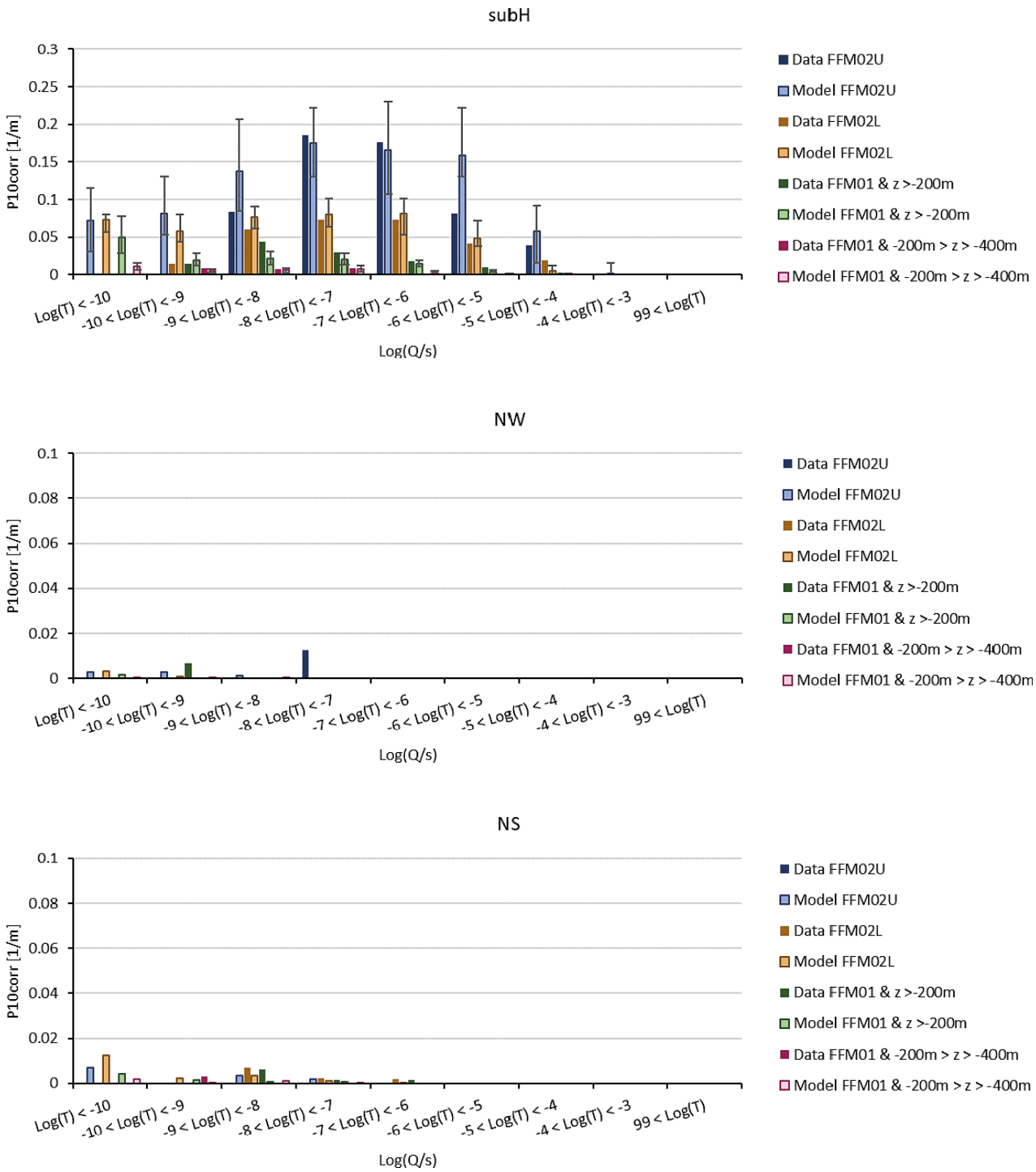


***Figure 4-8.*** *Histograms for the intensity of flowing fractures by rock units FFM02(U/L) and FFM01 (above and below z = −200 m) for orientation sets sub-horizontal, striking NW and striking NS. Model results are the average over 10 realisations of DFN Model Variant 1 (simulated KFM holes only). For the sub-horizontal fracture set, error bars indicate the maximum and minimum results across the realisations.*

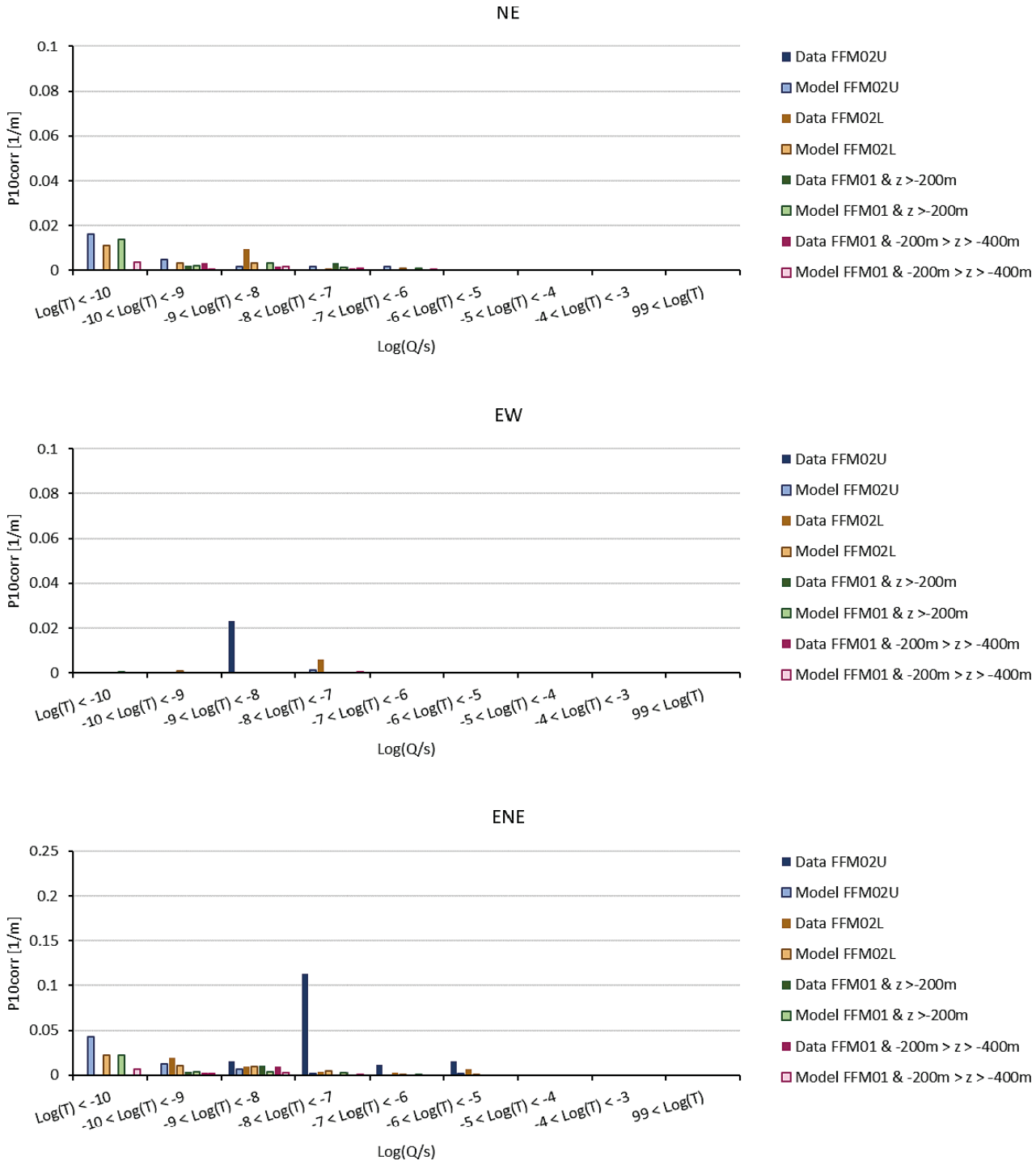


***Figure 4-9.*** *Histograms for the intensity of flowing fractures by rock units FFM02(U/L) and FFM01 (above and below z = −200 m) for orientation sets striking NE, striking EW and striking ENE. Model results are the average over 10 realisations of DFN Model Variant 1 (simulated KFM holes only).*

Figure 4-10 through Figure 4-14 show the equivalent plots for Model Variant 2 with a power-law size model for sheet joints with a calibrated low $k_r$ exponent. This gives similar results to model Variant 1. There is a little more variability in total flows between realisation, which might be of some benefit in describing the variability seen between holes, but otherwise both cases are equally calibrated. It is not the choice of size distribution that matters so much as that they give similar optimal numbers of larger connected fractures.

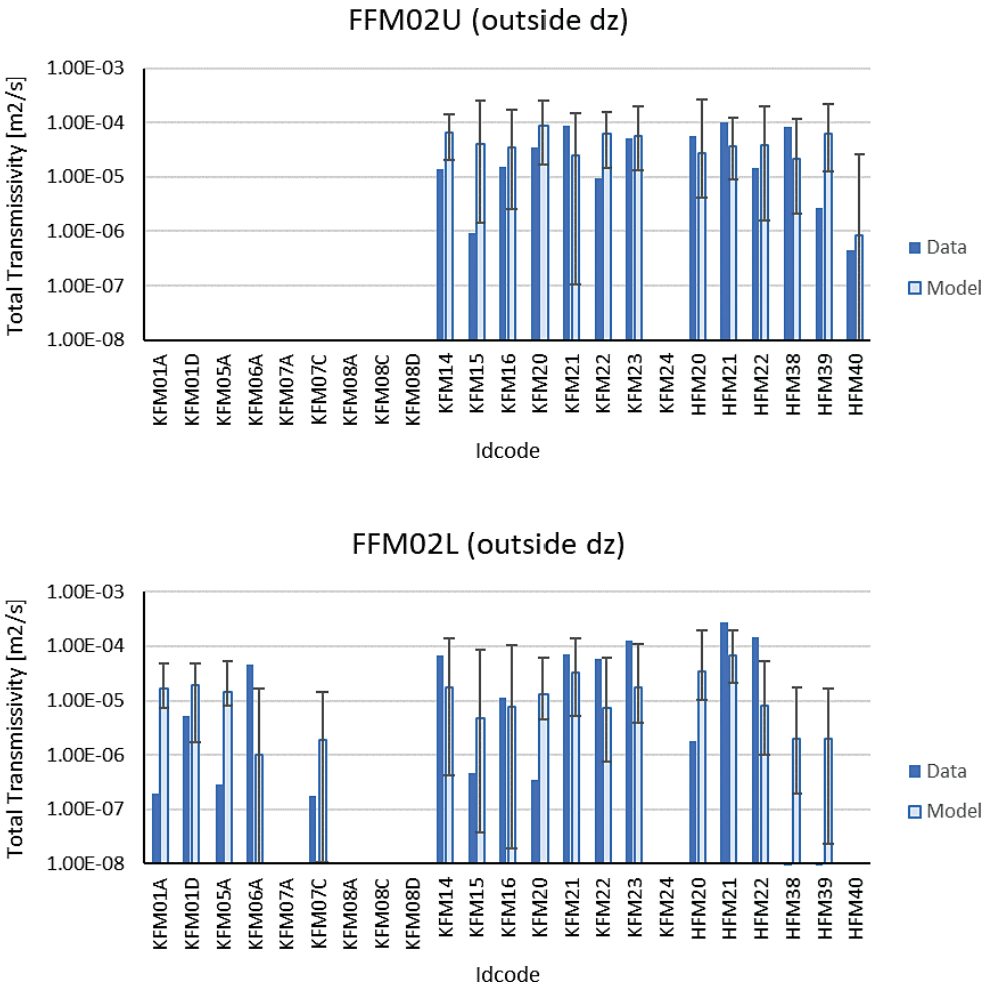


***Figure 4-10.*** *Geometric mean values for Total Q/s outside deformation zones and inside unit FFM02 for 10 realisations for DFN Model Variant 2. Error bars indicate the minimum and maximum of 10 realisations. Data is shown in dark blue.*

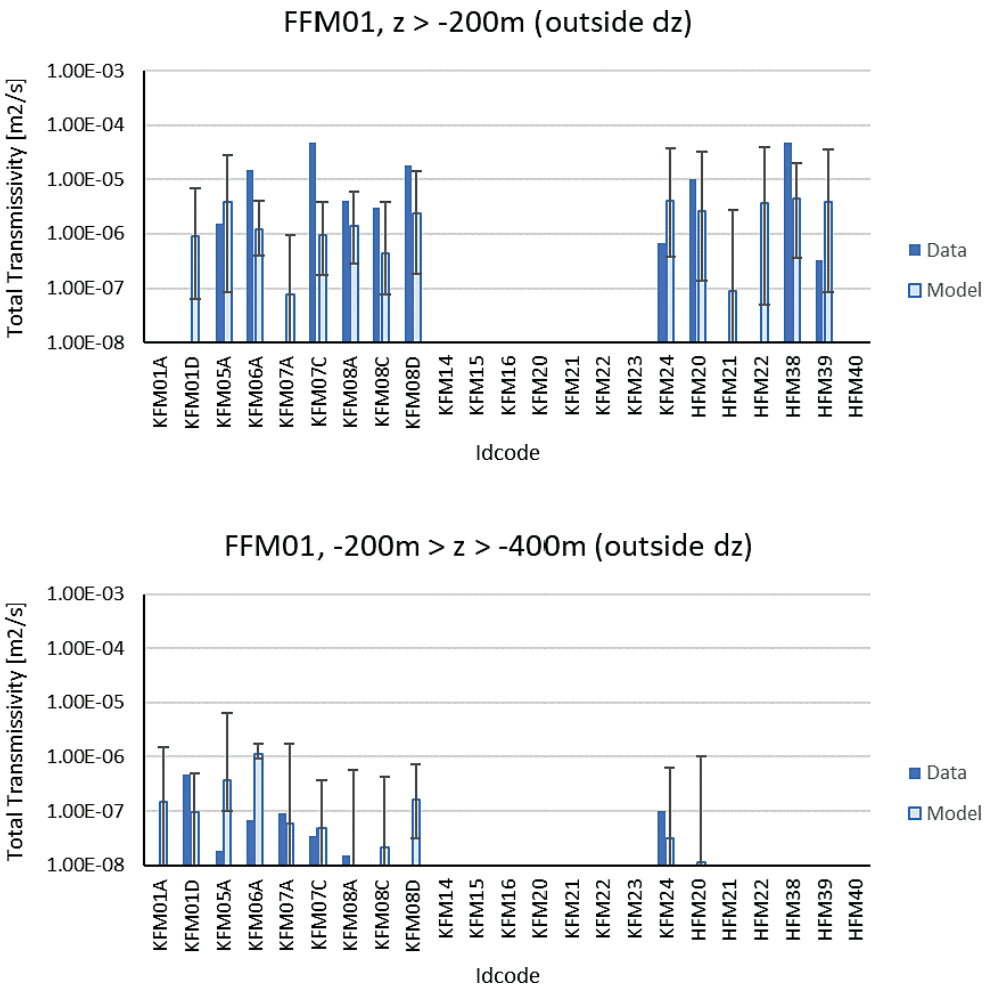


***Figure 4-11.*** *Geometric mean values for Total Q/s outside deformation zones and inside unit FFM01 for 10 realisations for DFN Model Variant 2. Error bars indicate the minimum and maximum of 10 realisations. Data is shown in dark blue.*

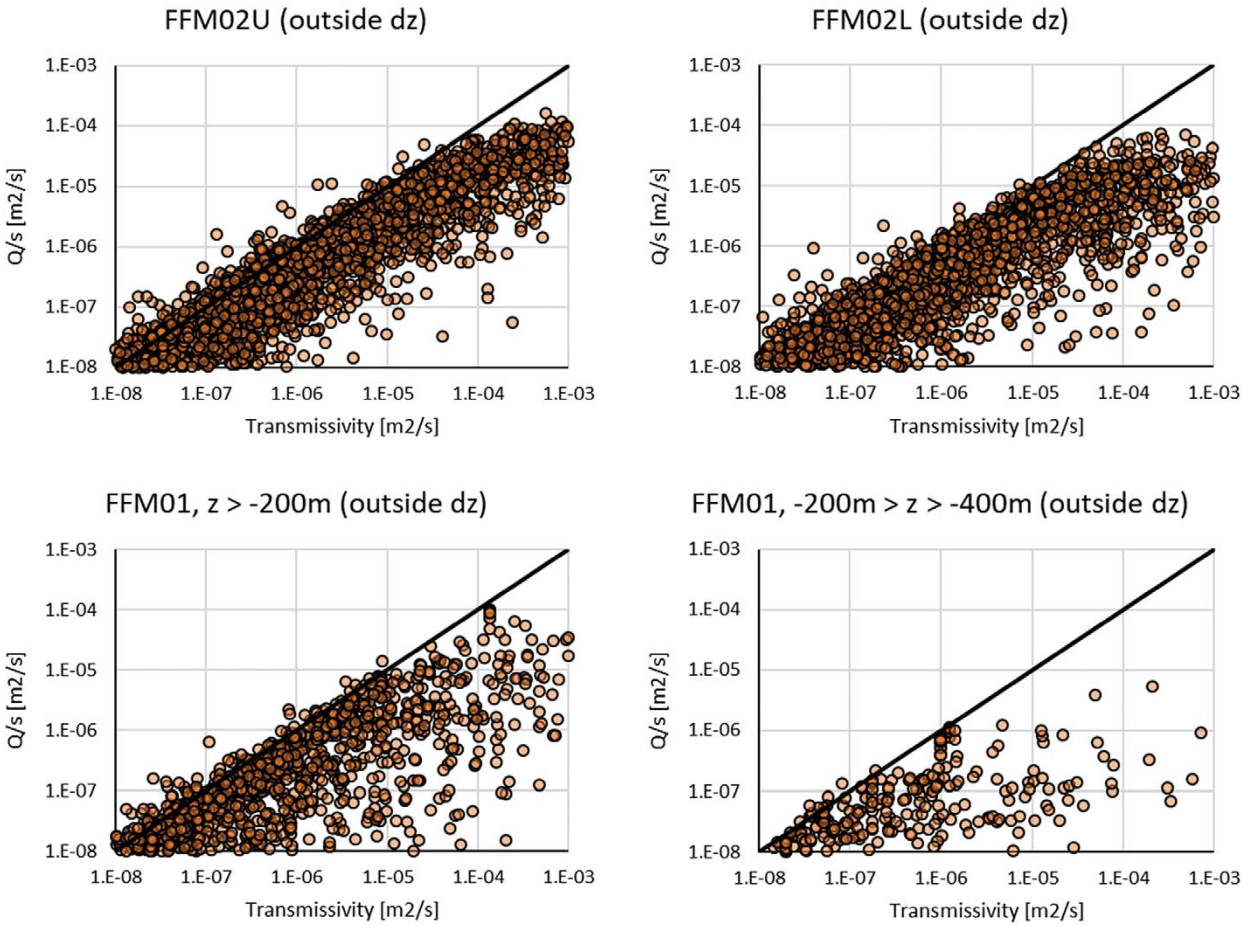


***Figure 4-12.*** *Transmissivity Vs Q/s (10 realisations of DFN Model V2) outside deformation zones, providing an indication of hydraulic choking in each rock unit.*

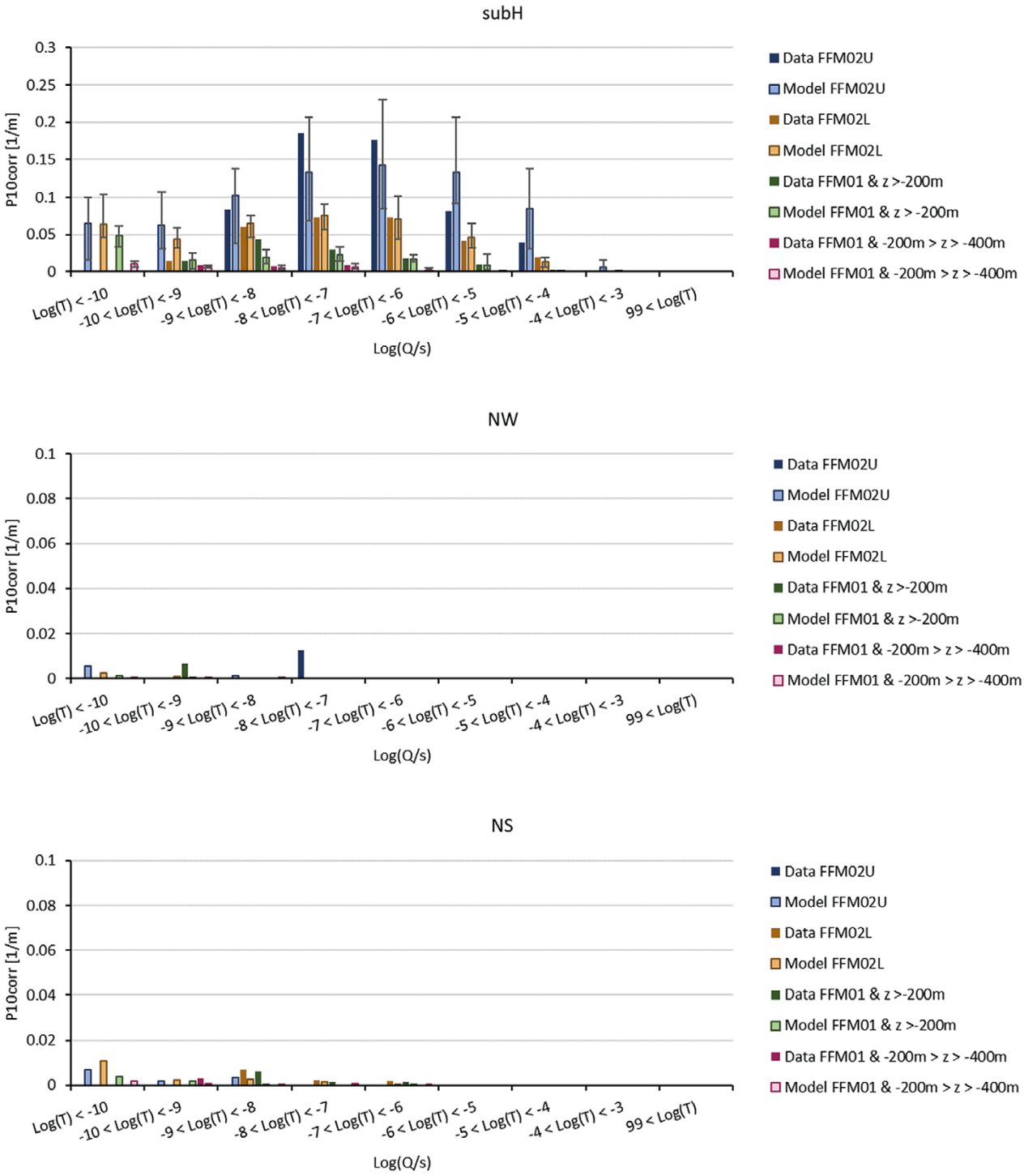


***Figure 4-13.*** *Histograms for the intensity of flowing fractures by rock units FFM02(U/L) and FFM01 (above and below z = −200 m) for orientation sets sub-horizontal, striking NW and striking NS. Model results are the average over 10 realisations of DFN Model Variant 2 (simulated KFM holes only). For the sub-horizontal fracture set, error bars indicate the maximum and minimum results across the realisations.*

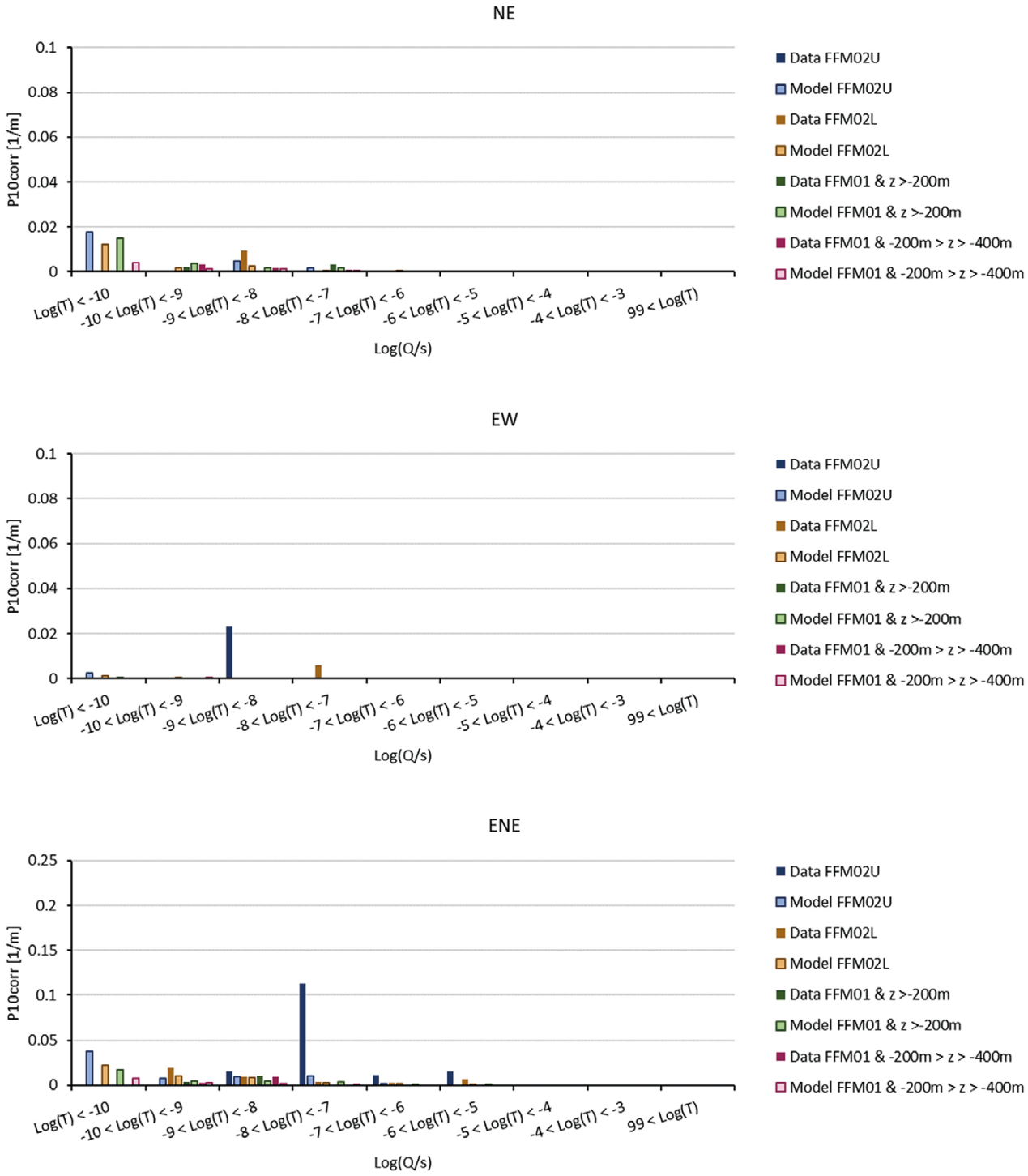


***Figure 4-14.*** *Histograms for the intensity of flowing fractures by rock units FFM02(U/L) and FFM01 (above and below z = −200 m) for orientation sets striking NE, striking EW and striking ENE. Model results are the average over 10 realisations of DFN Model Variant 2 (simulated KFM holes only).*

Figure 4-15 through Figure 4-19 present similar plots for model Variant 3 with a log-normal size distribution for sheet joints but with higher mean and variance in the size. The most notable features of these results are a lower choking factors shown in Figure 4-17 compared to model Variant 1. This also leads to higher, over-predicted, total flows in Figure 4-15. Hence, the size distribution inferred from the trace seen on the inlet channel or its power-law equivalent seem the more representative models.

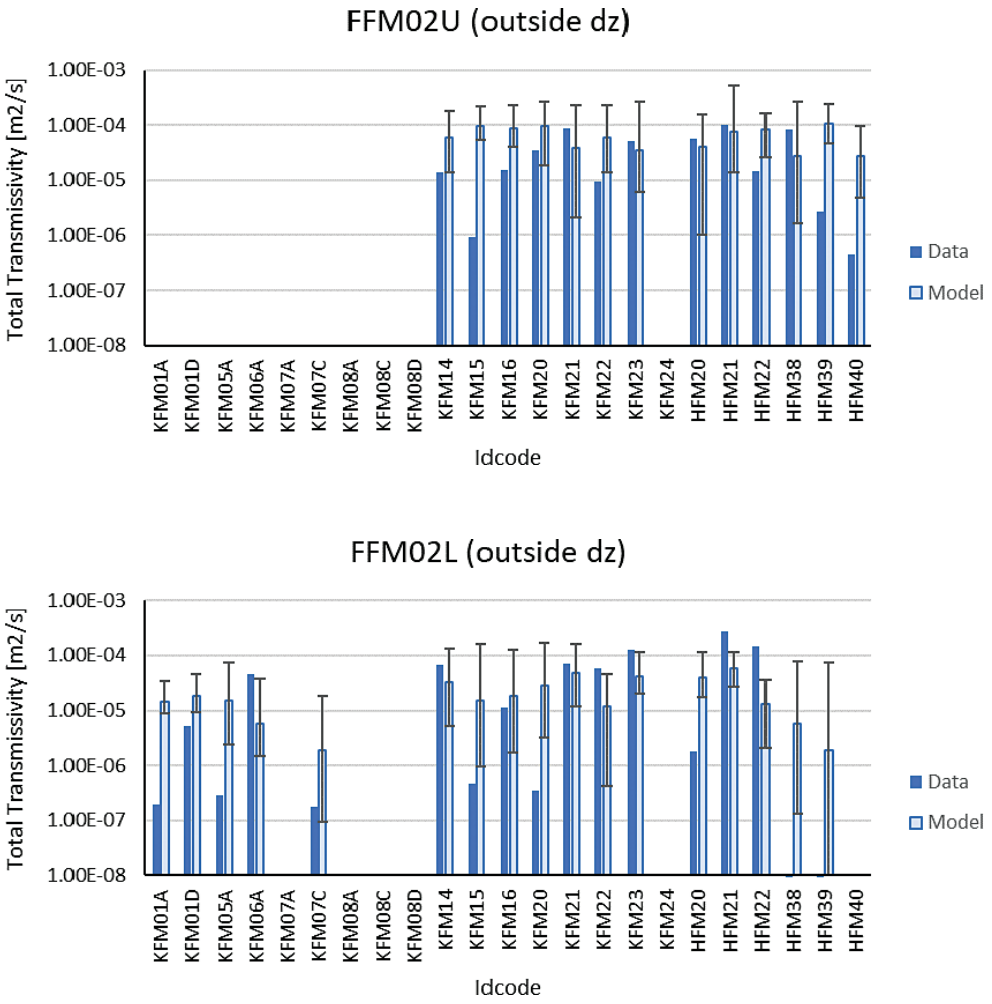


***Figure 4-15.*** *Geometric mean values for Total Q/s outside deformation zones and inside unit FFM02 for 10 realisations for DFN Model Variant 3. Error bars indicate the minimum and maximum of 10 realisations. Data is shown in dark blue.*

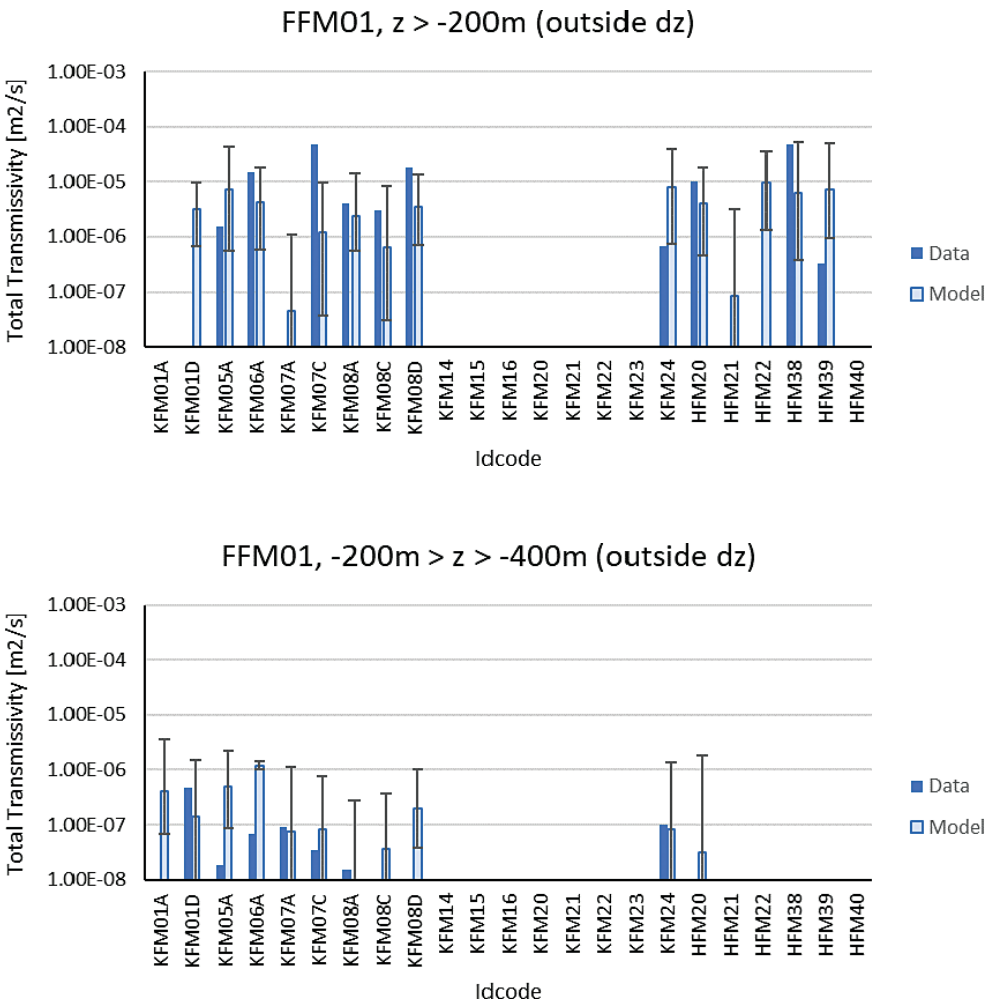


***Figure 4-16.*** *Geometric mean values for Total Q/s outside deformation zones and inside unit FFM01 for 10 realisations for DFN Model Variant 3. Error bars indicate the minimum and maximum of 10 realisations. Data is shown in dark blue.*

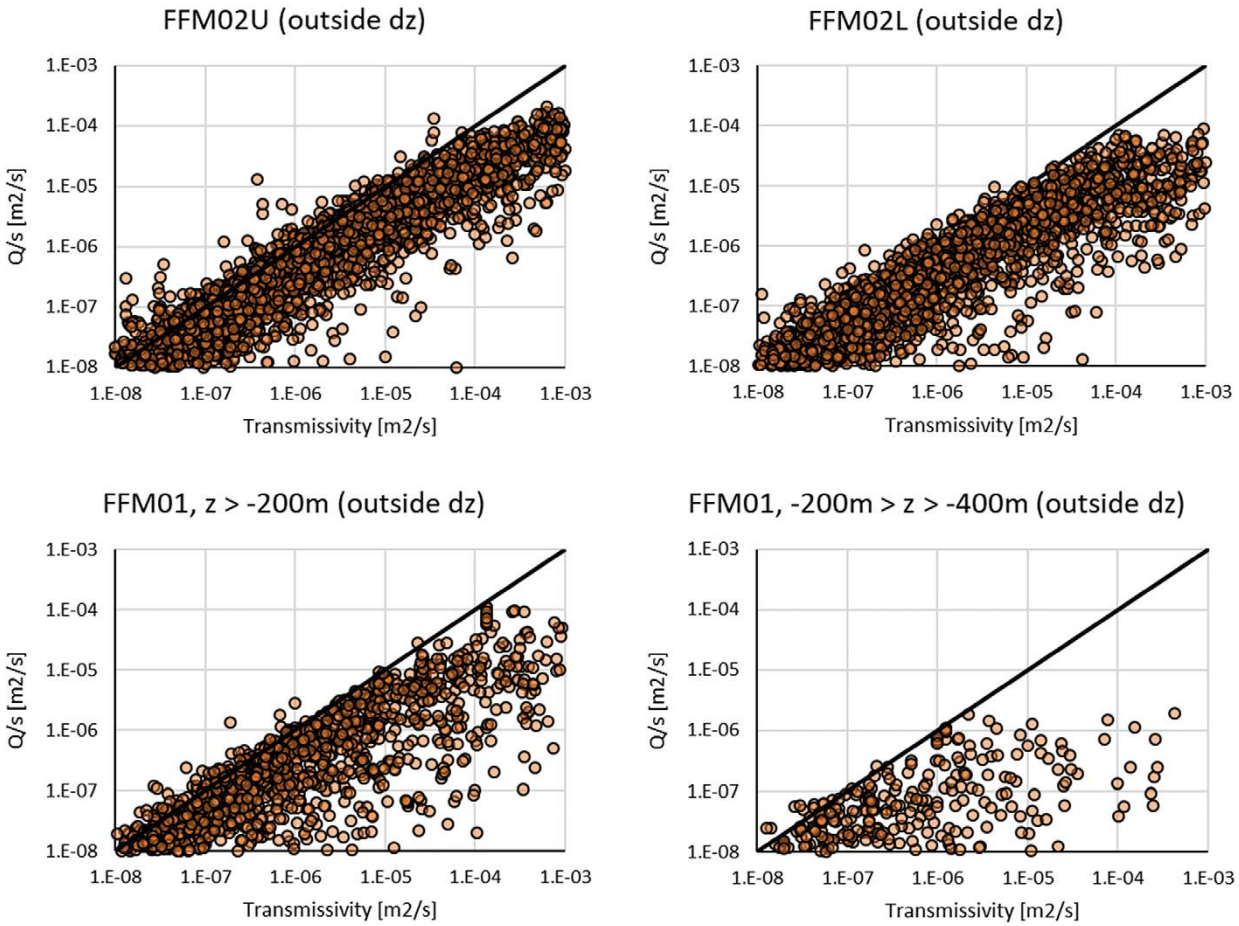


***Figure 4-17.*** *Transmissivity Vs Q/s (10 realisations of DFN Model V3) outside deformation zones, providing an indication of hydraulic choking in each rock unit.*

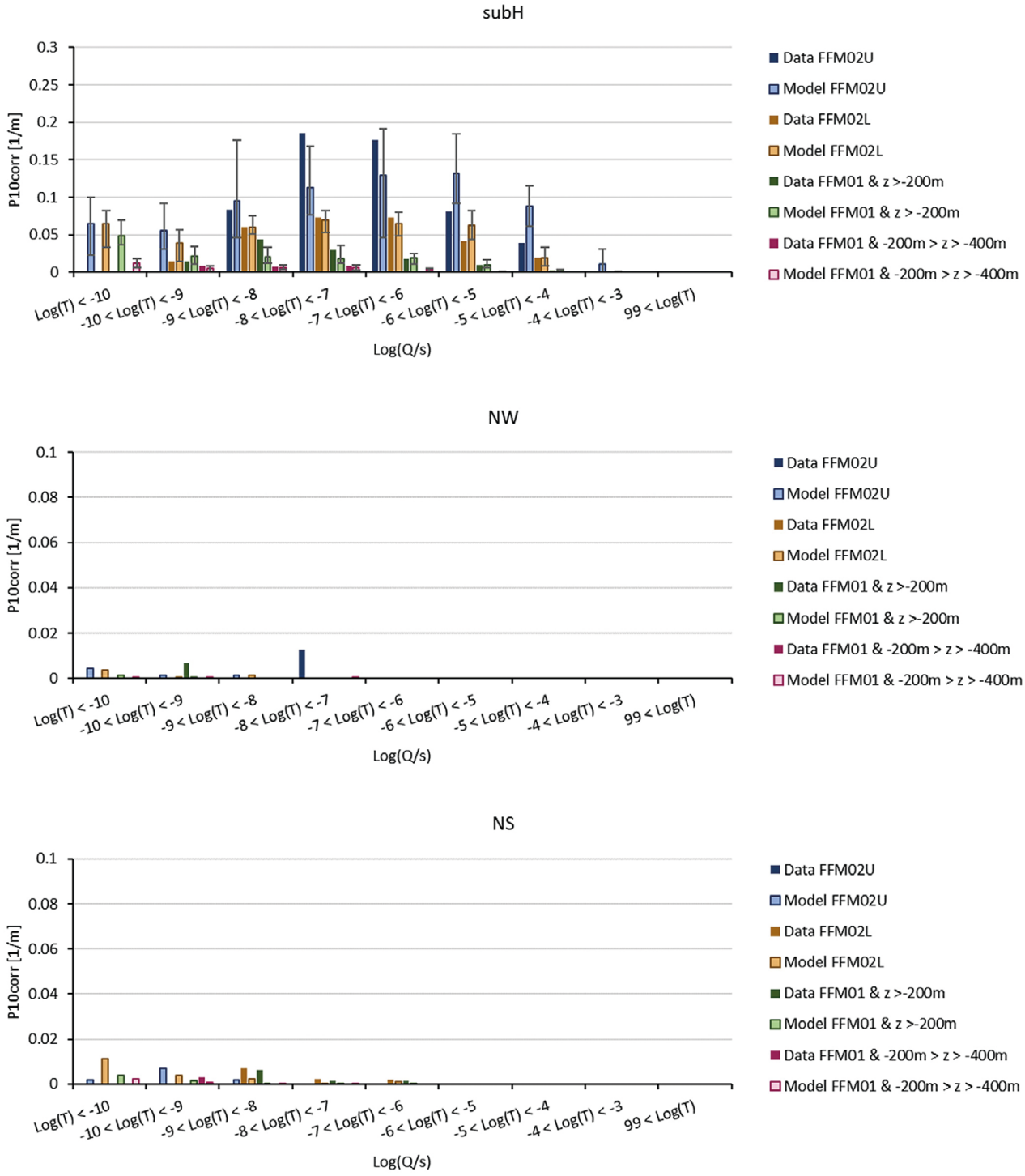


***Figure 4-18.*** *Histograms for the intensity of flowing fractures by rock units FFM02(U/L) and FFM01 (above and below z = −200 m) for orientation sets sub-horizontal, striking NW and striking NS. Model results are the average over 10 realisations of DFN Model Variant 3 (simulated KFM holes only). For the sub-horizontal fracture set, error bars indicate the maximum and minimum results across the realisations.*

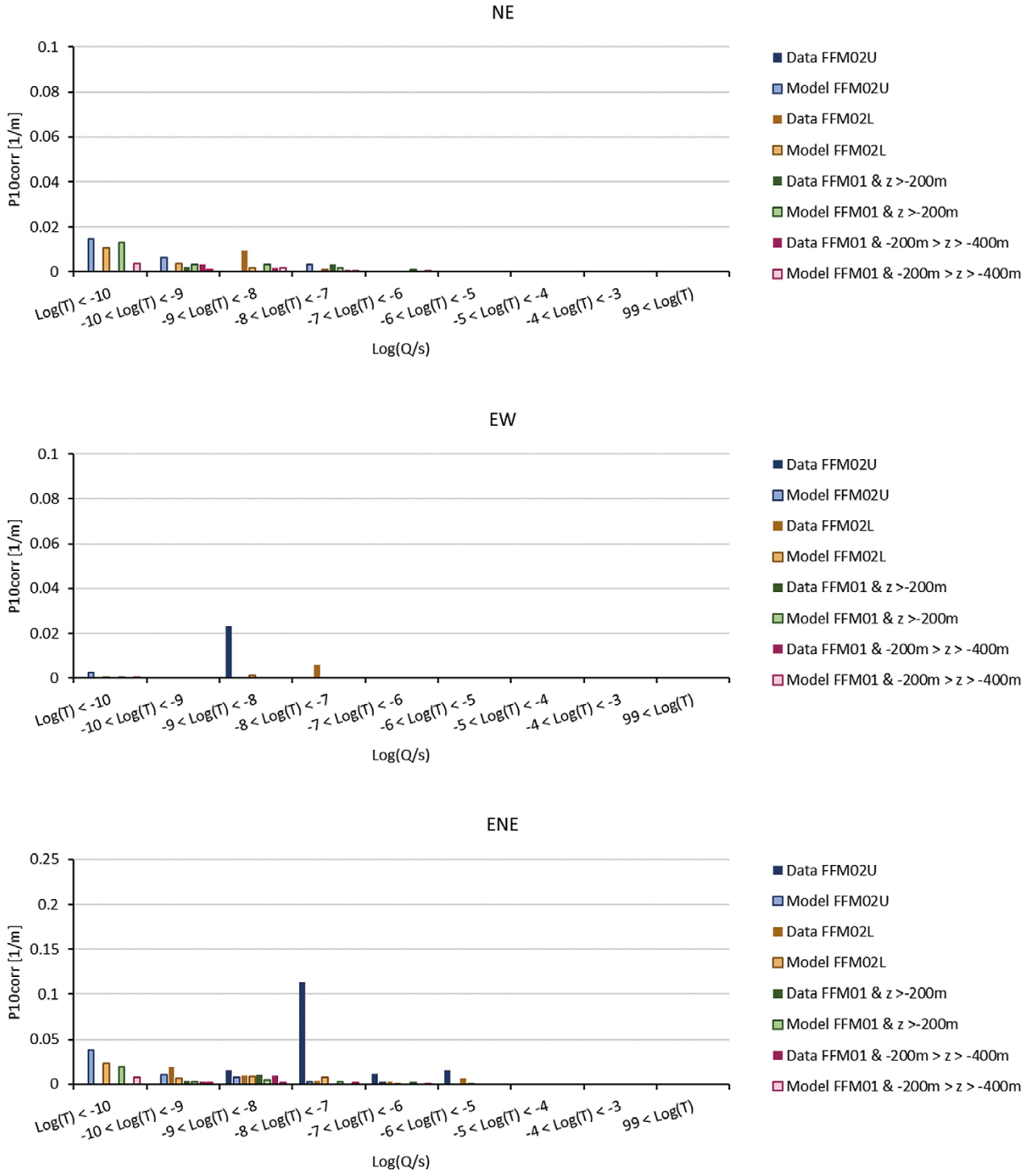


***Figure 4-19.*** *Histograms for the intensity of flowing fractures by rock units FFM02(U/L) and FFM01 (above and below z = −200 m) for orientation sets striking NE, striking EW and striking ENE. Model results are the average over 10 realisations of DFN Model Variant 3 (simulated KFM holes only).*

## 4.3 Modelling of interference tests

### 4.3.1 HFM43 simulation configuration

The interference test conducted in HFM43 was modelled in the cylindrical facility-scale area of diameter 3 800 m and centred around 160900, 6698100. This covered all of the monitored boreholes (apart from the outlying HFM18) and potential flow pathways via deformation zones to the south (Figure 2-1). The test was simulated using an ECPM representation using the Oda method (Oda 1986) to upscale the DFN model Variant 1 after calibration on single-holes tests. Before upscaling, all fractures not connected to the external boundary were removed. The ECPM model is implemented in DarcyTools (Svensson 2010), as shown in Figure 4-20.

The grid extends from the ground surface to 450 m elevation. Octree meshing is used to give variable grid resolution, increasing around areas of interest. The following resolutions were applied:

- 0.5 m at the borehole intervals,
- 9 m vertical and 18 m horizonal resolution above −30 m elevation,
- 18 m around the deformation zones,
- a maximum of 36 m elsewhere.

Both monitoring and pumping intervals were represented as a chain of adjacent grid cells mirroring the path of the borehole. These intervals were modelled with a very low specific storage ($1 \times 10^{-21}$ m$^{-1}$) and a very high transmissivity ($1 \times 10^{-3}$). This aimed to simulate the intervals as hydraulic conduits. By only applying these properties to the monitored intervals, gaps with more limited hydraulic connectivity were maintained between packed-off monitored intervals in the same borehole, see Figure 4-21.

Pumping in HFM43 was modelled as a fixed pressure value, constant down the whole pumped interval at each timestep, that was varied each timestep to achieve the measured constant abstraction rate into the pumping interval. The flow rate was set to match the mean flow rate for the actual HFM43 test; 270.6 L/min (0.00451 m$^3$/s). The modelled test duration was set to that of the actual test: ~21 days.

The base of the grid was modelled as a no-flow boundary, the lateral exterior faces of the grid were configured as hydrostatic, and the top of the grid was given a nominal low recharge of flow approximating 1 mm of rain per month ($3.8 \times 10^{-10}$ m/s) as little rain was reported during the test period.

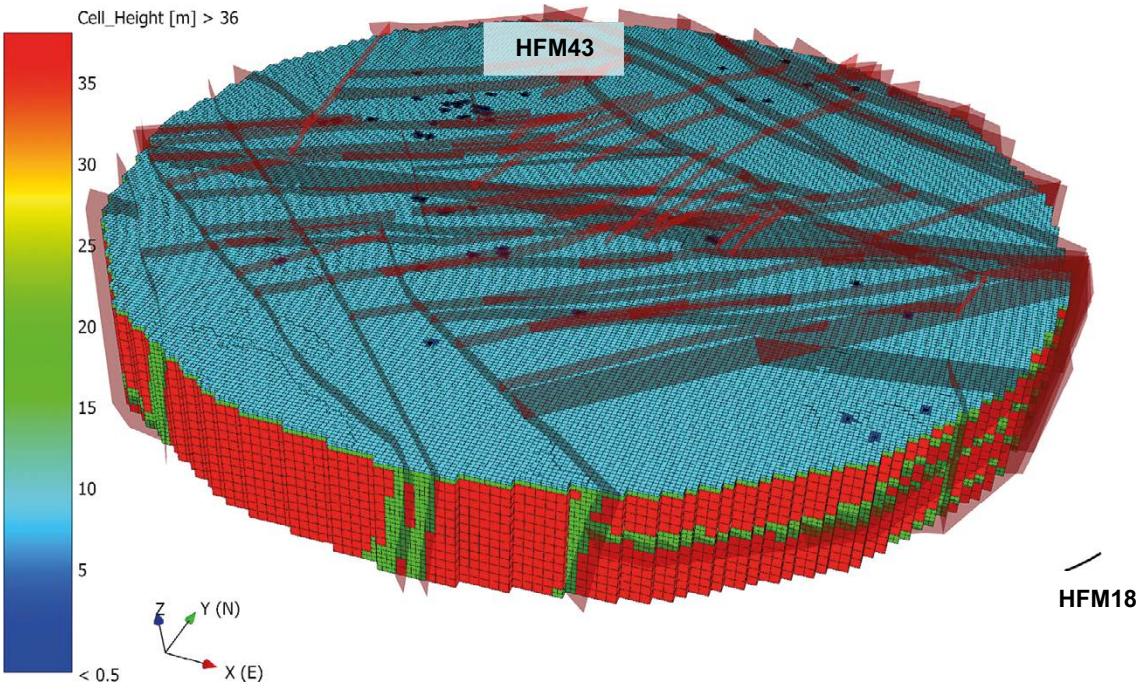


***Figure 4-20.*** *View of the DarcyTools grid with BFZs around the grid and HFM18. The grid is 3 800 m in diameter and up to 465 m thick. Its location is shown in Figure 2-1.*

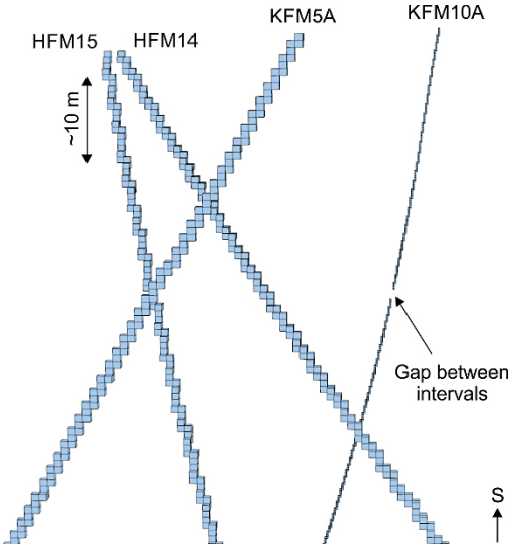


***Figure 4-21.*** *Visualisation of the grid cells that compose the monitoring or pumping intervals.*

### 4.3.2 HFM43 simulation results

One realisation of each of the three fracture model variants is simulated. Fracture model Variant 3 results in the drawdown closest to the actual drawdown, but all models give a reasonable prediction, given they are one realisation of an unconditioned stochastic model, see Table 4-2. A comparison of drawdowns in monitored intervals and time to a response being detected is shown in Figure 4-22 for the 3 variants models and the data. The models span the drawdowns where they occur. Model Variant 2 (power-law size model) is the best fit overall, although Model Variant 1 better predicts some of the near field large drawdowns. However, the ECPM model does not predict the discrete nature of the responses because it is a continuum model, connecting all adjacent cells. Oda geometric upscaling has a tendency to provide an upper limit for equivalent hydraulic conductivity, not providing representing effects such as hydraulic choking effects, a deficiency that can be expected with all ECPM methods. The times to respond also seem to be in good agreement for monitoring holes that gave a significant drawdown. Some tens of realisations of each model variants would be required to conclude if any one of model variants were performing consistently better than the others.

**Table 4-2. Actual and simulated drawdowns for the HFM43 interference test.**

| | Drawdown at end of pumping (m) |
|---|---|
| Actual Test | 9.6 |
| Model Variant 1 | 18.4 |
| Model Variant 2 | 12.8 |
| Model Variant 3 | 10.4 |

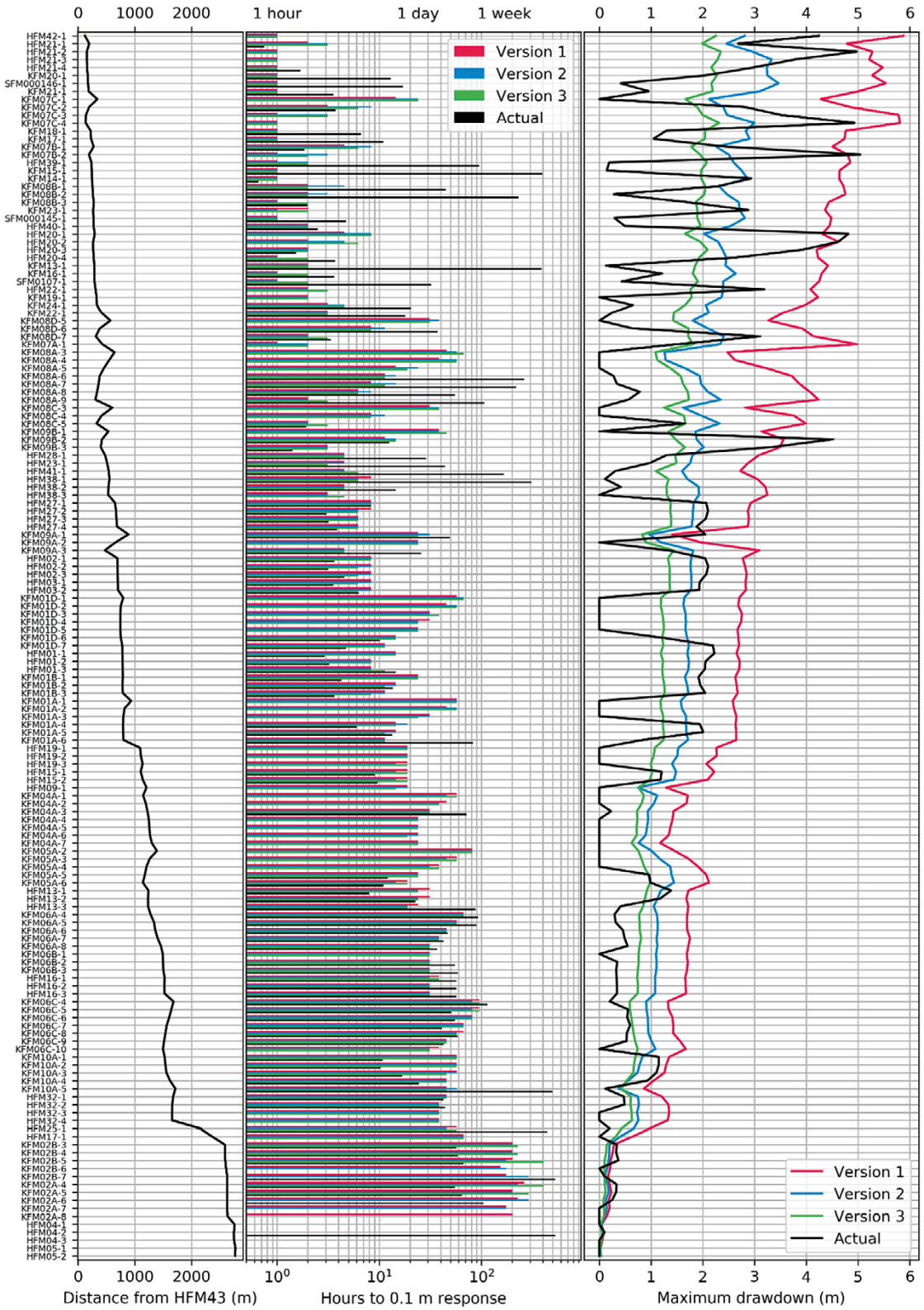


***Figure 4-22.*** *Graphs showing the observed and simulated responses to the interference tests at HFM43 in the three variant models ("versions" here).*

Figure 4-23 shows some examples of transient drawdown in two different holes for the three model variants. The drawdown magnitudes are of the correct order of magnitude in both holes, but again the measured responses are more discrete than the modelled ones. This again is likely to be a result of the continuous nature of the ECPM models with flow between the intervals even though the spacing between the intervals has been assigned low conductivity. Fine grids would be needed around each gap of the monitored intervals to have any chance of predicting the variability in drawdowns between intervals.

In summary, the ECPM representation of the DFN model variants all perform reasonably in simulating the HFM43 interference test in terms of both drawdowns and response times. However, the continuity of the ECPM representation does not reproduce the discrete nature of measured responses with areas unaffected by the pumping in HFM43 or the differences in drawdowns between different intervals in the same hole. Simulating interference tests directly with a DFN model may better replicate these features of the responses.

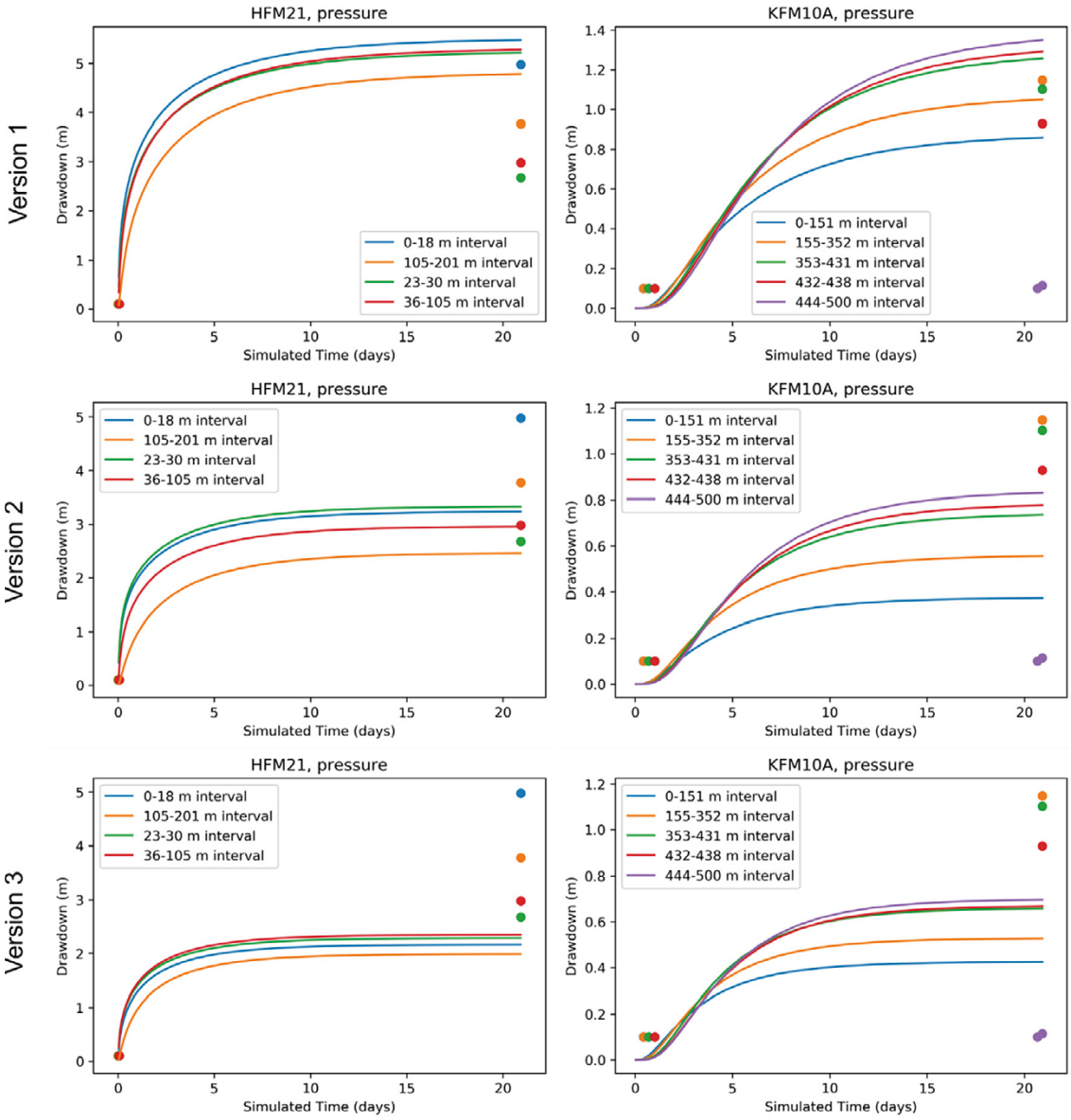


***Figure 4-23.*** *Graphs showing the flow responses for the actual interference test (dots) and three different fracture variants (lines) for a borehole close (< 200 m) to the pumping hole and far (> 1 500 m) from the pumping hole (HFM21 and KFM10A respectively).*

## 4.4 Upscaling of hydraulic properties

### 4.4.1 Comparison for PFL tests in KFM23

The grids used in the single-hole calibrations were sub-areas of the facility-scale grid used for the interference test of Section 4.3. For KFM23 it measures c 550 m in diameter and is centred at 160279, 6698676. The hydraulic test in this hole is used as a comparison of performing these single-hole tests in a DFN versus ECPM simulations using DarcyTools.

The lateral external boundaries were set as fixed pressure, and the top and bottom boundaries were set as no-flow. The same DFN realisation of model Variant 1 is used as in Section 4.3.

Three upscaling methods were tried, GEHYCO volume weighted (vol.), GEHYCO area weighted (Area) and Oda. In brief, the GEHYCO (Area) method is an update of the GEHYCO (Vol.) method that reduces the smearing of each fracture over the cells it intersects and some neighbours.

Oda upscaling was carried out in FracMan and produced a six-component cell centred conductivity tensor. Only the diagonal tensor components (Kxx, Kyy and Kzz) were used. To convert from cell-centred upscaled conductivities to face centred conductivities for use in DarcyTools, the harmonic mean of the two neighbouring cells was used to allow for difference in cell size on the octree grid. When considering two neighbouring cells A and B:

$$K_f = \frac{D_A + D_B}{\frac{D_A}{K_A} + \frac{D_B}{K_B}}$$ Equation (4-12)

Where:

$Kf$ = cell face permeability between A and B.

$D_A$, $D_B$ = length of cells A and B respectively in the subject dimension.

$K_A$, $K_B$ = cell permeability in the subject dimension of cells A and B respectively.

Four simulations of the steady-state inflows to KFM23 under PFL-f conditions were made:

- The raw DFN model using FracMan;
- An ECPM model using DarcyTools with hydraulic conductivity upscaled using FracMan's Oda method;
- An ECPM model using DarcyTools with hydraulic conductivity upscaled using GEHYCO(Vol) method; and
- An ECPM model using DarcyTools with hydraulic conductivity upscaled using GEHYCO(Area) method.

A comparison of the total flows to the hole are shown in Figure 4-24 summed over the borehole cylinder. The ECPM results using the Oda upscaled properties is reasonably close to the DFN simulation. The GEHYCO(Vol) results are around one order of magnitude higher, while the GEHYCO (Area) method is an improvement, about a factor 2 lower. Figure 4-25 gives a bit more detail, showing the flows from individual fracture/cell intersects. The results are mostly in this same order, but it is also seen that the GEHYCO results sometimes smear beyond where the DFN calculates the flows.

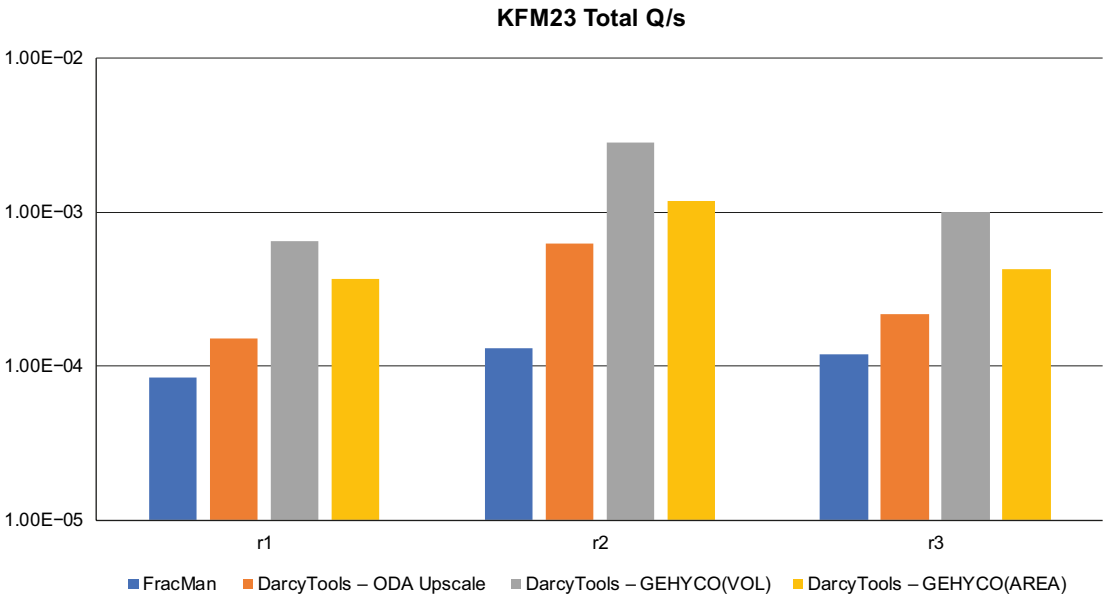


***Figure 4-24.*** *Comparison of total simulated specific capacity ($m^2/s$) to KFM23 for 1 realisation of a PFL-f test using FracMan, DarcyTools using FracMan's Oda upscaling, DarcyTools GEHYCO (Vol) and (Area) methods.*

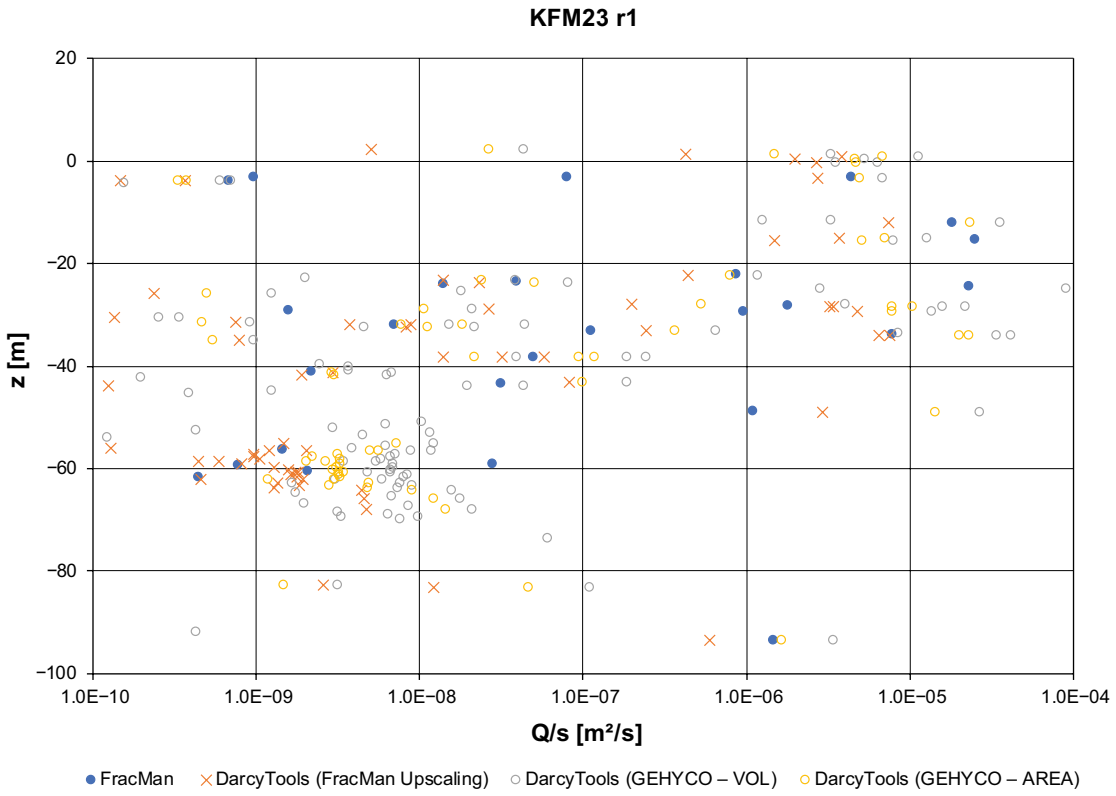


***Figure 4-25.*** *Comparison of discrete specific capacities ($m^2/s$) to KFM23 for 1 realisation of a PFL-f test using FracMan, DarcyTools using FracMan's Oda upscaling, DarcyTools GEHYCO (Vol) and (Area) methods.*

### 4.4.2 Geometric (Oda) versus flow-based upscaling

Both Oda method implemented in FracMan and GEHYCO in DarcyTools are analytical methods using only fracture geometry and properties without factoring connectivity and hydraulic choking. The Oda method should therefore be considered as an upper bound for the true equivalent hydraulic conductivity tensor. A more accurate, but computationally intensive method of upscaling is to simulate flows across each grid cell and each axial direction, see e.g. (Lei et al. 2015) for a review of methods. Here, we compare the results of Oda and flow-based upscaling for a DFN model using similar properties to those of FFM02L, with a power-law size distribution and significant inter-fracture heterogeneity, see Figure 4-26. The model is split into an array of 1 000 blocks and both methods used to upscale each block to a permeability tensor, as compared in Figure 4-27. There is a clear correlation between the two sets of results, but the permeabilities are lower for the flow-based upscaling because of variable connectivity and hydraulic choking due to the sparsity and variability in the network.

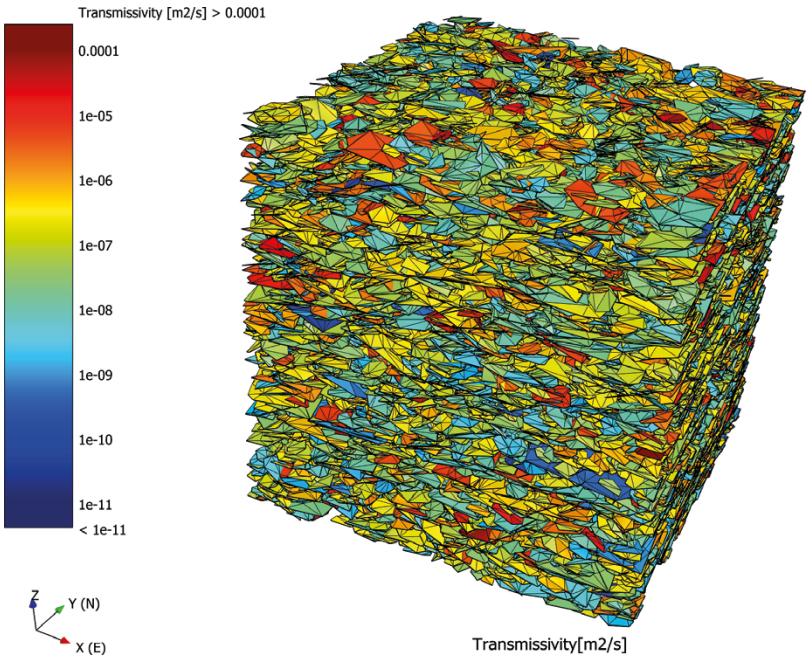


***Figure 4-26.*** *DFN block based on FFM02L properties with inter-fracture heterogeneity used as a test of upscaling methods.*

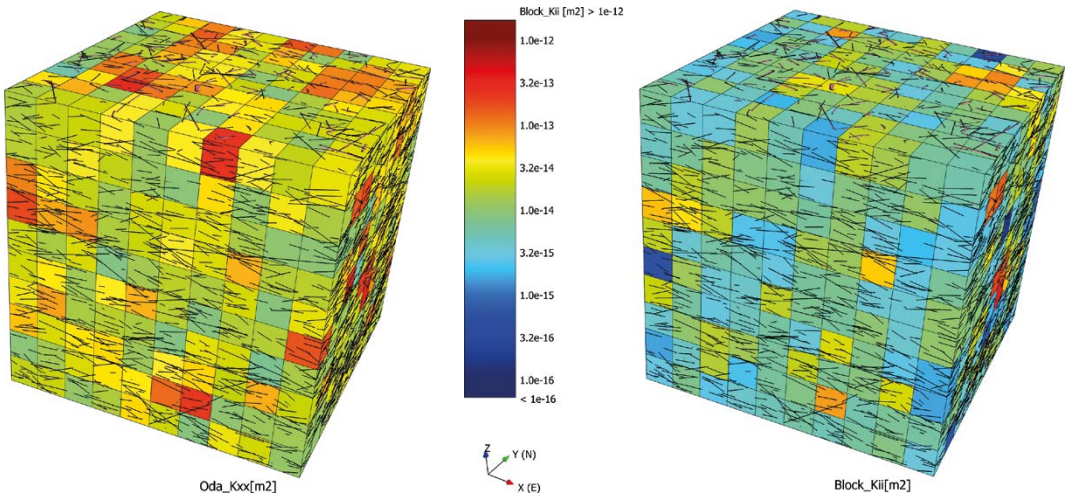


***Figure 4-27.*** *Upscaled Kxx permeability for a 10×10×10 array of cells. Left) Oda geometric upscaling, Right) Flow-based upscaling.*

Figure 4-28 makes a cross-plot of the flow-based and Oda-based permeabilities in the x axis direction across all 100 cells. This demonstrates that the Oda results are indeed an upper bound for the flow-based values and that most of the cloud values lies within 1 factor 1–1/3 of the Oda values. The median ratio is about 0.35 and about 70 % of flow-based values are less than ½ the Oda-based value. This is consistent with the over-prediction of total flow to KFM23 by a about a factor 2–3 between Oda based upscaling and DFN simulation. It is therefore preferable to use DFN based simulation where possible, flow-based upscaling where an ECPM approach is necessary, or to use the Oda method for numerical speed, but rescale the calculated permeabilities based on some numerical comparisons such as this between flow-based and Oda-based upscaling to derive a case specific scaling factor.

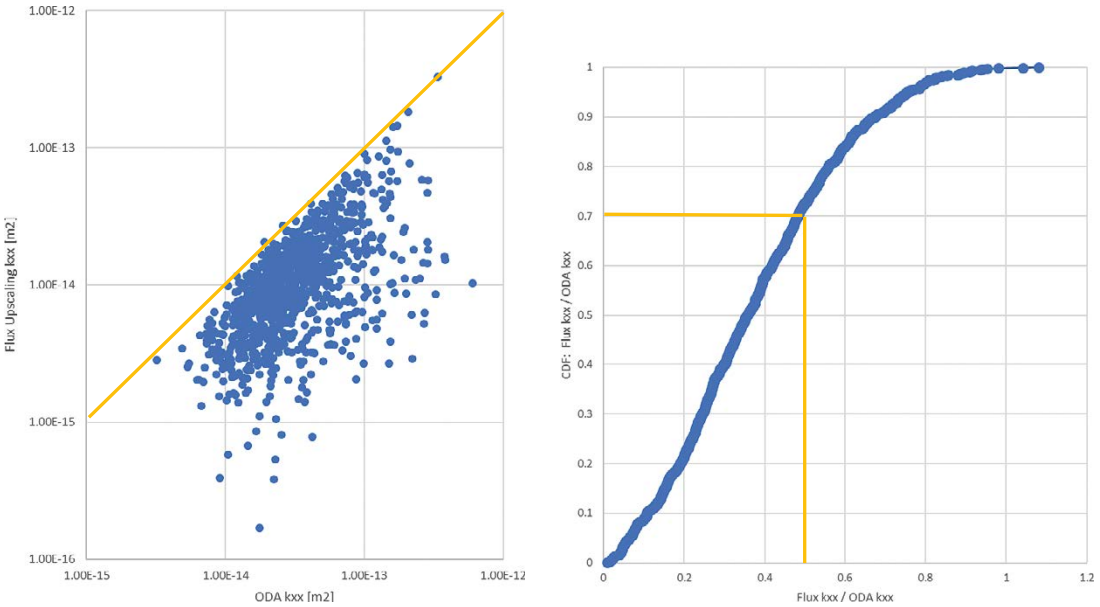


***Figure 4-28.*** *Left) Cross-plot of flow-based versus Oda upscaled Kxx over all cells. Right) Cumulative distribution of ratio of flow-based to Oda based Kxx.*

### 4.4.3 Upscaling to MIKE SHE

Having calibrated on the single-hole hydraulic tests and checked against the HFM43 interference test, the facility-scale model was upscaled and the properties extrapolated to the catchment-scale required for near-surface hydrological modelling in MIKE SHE.

The MIKE SHE grid has the following specification:

- Origin at 154750, 6689970, −1 000,
- 20 m horizontal cell resolution,
- 1 100 cells along the x axis,
- 1 000 cells along the y axis.
- Vertical cell resolution is:
  - 5 m from 0 to −30 m elevation,
  - 20 m from −30 to −200 m elevation,
  - 50 m from −200 to −500 m elevation,
  - 100 m from −500 to −1 000 m elevation.

The resulting grid has 27.5 million cells and covers 440 km³. The hydraulic properties of the ZFMs, upscaled using the Oda method, were directly applied to this grid, but the large volume is impractical for generation of DFNs that include the size distribution used in the non-ZFM fractures here. Instead, the non-ZFM fractures were upscaled to the portion of the grid covering the facility-scale area used in modelling the HFM43 interference test using the Oda method, and then extrapolated using the statistical distribution of the permeability field. The extrapolation used random sampling of the cells at the same elevation inside the area of the grid with non-ZFM fractures. The result in shown in Figure 4-29.

This extrapolation was carried out by randomly sampling those grid cells in the DFN region, but outside the lens region, to fill the cells outside the DFN region (Figure 4-29). This was applied on each vertical layer in grid to maintain the depth trends. For those grid cells lower than the maximum depth of the DFN region, the depth of the DFN region was extrapolated. This was done independently for the DFN region inside the lens, and the DFN region outside the lens. The depth trend was assumed to follow a power law.

In addition, the geometries of the modelled fractures were made available as fab files. A description of this file format is given in the Appendix.

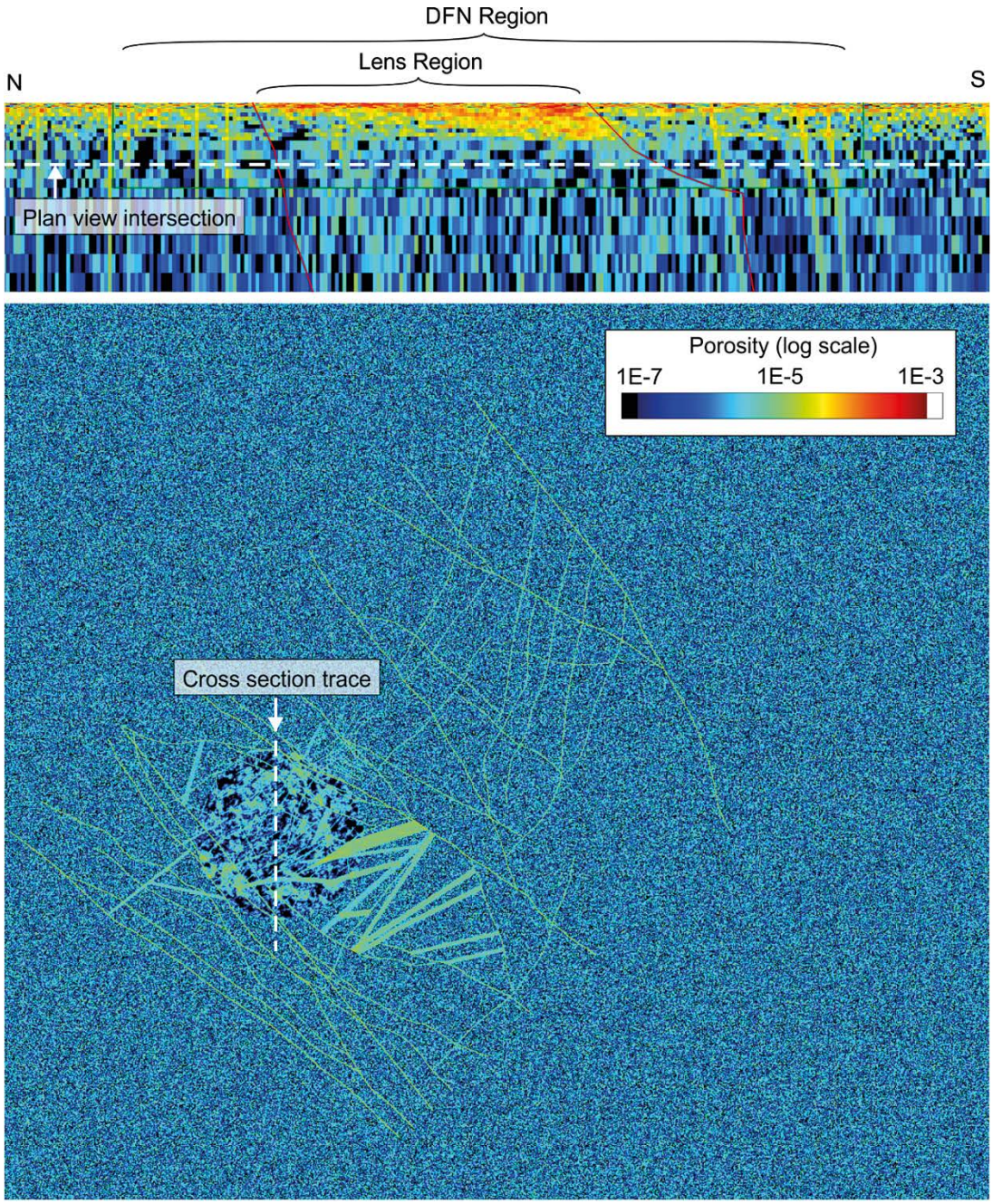


***Figure 4-29.*** *Cross-section and plan views of the MIKE SHE grid with upscaled and extrapolated porosity values from fracture Variant 1, with the DFN and lens regions highlighted.*

## 4.5 Summary of DFN recipe

Table 4-3 and Table 4-4 gather the geometric parameters used for modelling open fractures and the following equations summarise the hydraulic parameters as a function of the effective normal stress, where the truncated normal distribution is denoted N (mean, std. dev., min., max).

**Table 4-3. Actual Open fracture intensities for the various domain/set combinations.**

| | Open fracture intensities from boreholes $P_{32}$ ($r > r_0$) ($m^2/m^3$) | | | | | | |
|---|---|---|---|---|---|---|---|
| **Domain** | **SubH** | **Sheet joint** | **NW** | **NS** | **ENE** | **NE** | **EW** |
| Outside Lens (z > −30 m) | 0.35 | 0.38 | 0.56 | 0.45 | 1.05 | 0.43 | 0.36 |
| Outside Lens (−30 > z > −200 m) | 0.65 | | 0.56 | 0.26 | 0.58 | 0.25 | 0.28 |
| Outside Lens (z < −200 m) | 0.38 | | 0.53 | 0.12 | 0.16 | 0.16 | 0.05 |
| FFM02 Upper | 0.78 | 1.23 | 0.21 | 0.27 | 0.87 | 0.15 | 0.28 |
| FFM02 Lower | 0.78 | 0.57 | 0.21 | 0.23 | 0.50 | 0.21 | 0.20 |
| FFM01/FFM06 (−30 > z > −200 m) | 0.78 | | 0.21 | 0.11 | 0.46 | 0.24 | 0.11 |
| FFM01/FFM06 (z < −200 m) | 0.34 | | 0.16 | 0.12 | 0.34 | 0.19 | 0.10 |

**Table 4-4. Actual Open fracture orientation and size parameters by set across all domains.**

| | Univariate Fisher Orientation | | | Power-law size | | | Log-normal size | |
|---|---|---|---|---|---|---|---|---|
| **Set** | **Trend** | **Plunge** | **Fisher Conc.** | **$k_r$ [-]** | **$r_0$ / $r_{min}$ [m]** | **$r_{max}$ [m]** | **Mean [m]** | **Std. Dev. [m]** |
| ENE | 149.7 | 2.58 | 21.8 | 2.62 | 0.038 | 300 | | |
| EW | 188.4 | 0.98 | 24 | 3.4 | 0.038 | 300 | | |
| NE | 302.3 | 2.57 | 25.8 | 2.62 | 0.038 | 300 | | |
| NS | 267.1 | 1.34 | 18.3 | 2.75 | 0.038 | 300 | | |
| NW | 53.91 | 1.69 | 17.7 | 3.2 | 0.038 | 300 | | |
| SubH | 357.4 | 86.1 | 24.5 | 2.5 | 0.038 | 300 | | |
| Sheetjoints (v1) | 357.4 | 86.1 | 24.5 | | 10 | 300 | 14.7 | 11.9 |
| Sheetjoints (v2) | 357.4 | 86.1 | 24.5 | 2.2 | 14.6 | 300 | | |
| Sheetjoints (v3) | 357.4 | 86.1 | 24.5 | | 10 | 300 | 38.2 | 33.9 |

$$\log_{10}(A') = \log_{10}(2 \cdot 10^{-5}) + 0.6N(0,1,-2,2) \quad \text{Equation (4-13)}$$

$$e_h = \left( \frac{A' r^{0.5}}{1 + \frac{9\sigma_n'}{B}} \right), \quad B = 30\ MPa \quad \text{Equation (4-14)}$$

$$T = \frac{\rho g}{12\mu} e_h^3 \quad \text{Equation (4-15)}$$

$$S = 0.001\ \sqrt{T} \quad \text{Equation (4-16)}$$

# 5 Conclusions

The current study has prototyped an update of the structural-hydraulic model for the shallow system using the newly acquired data from KFM11A–KFM24. This update allows the properties of individual fractures as well as networks to be analysed and implemented as discrete fracture network (DFN) models when simulating realisations of the fracture system. Building on the DFN descriptions for the deeper bedrock in SDM-Site (Follin 2008), an integrated model for the deep and shallow system as well the 2018 updated deformation zone model has been assembled as the foundation for the hydrogeological property model of the complete bedrock system.

A major challenge for this study has been to differentiate ancient sub-horizontal fractures seen throughout the bedrock from an increasing presence of reactivated or relatively young sub-horizontal fractures such as sheet joints associated with changes in loading with glacial cycling and to model these two components in a DFN model. Another major challenge has been to conceptualise and parameterise the DFN to reproduce the strong hydraulic anisotropy and the three–four orders of magnitude reduction in flow-rates over just a few hundred vertical metres between the surface and repository target depth.

The hydraulic properties of the DFN model have been calibrated on single-hole PFL-f hydraulic tests, impeller logging and checked against a three week long interference test in HFM43.

The key result of this analysis and modelling exercise is a hydrogeological property model that extends over the local catchment area, 22 km by 20 km, for input to hydrological modelling of the environmental impacts of construction of the facility.

The developed DFN model is described as a prototype since the ongoing modelling methodology planning for the underground accesses and operational stages require many conceptual and toolkit updates relative to SDM-Site. However, several notable progressions have been made, including:

- Integration of borehole geometric, structural and hydraulic data with interpretations and models in a “spatially aware” database environment.
- Formulating transmissivity through a hydromechanical coupling to stress to describe hydraulic anisotropy and depth dependencies.
- Calibrating DFN connectivity and hydraulic properties by simulating hydraulic tests in each individual borehole in the contact of it geological setting.

Outstanding methods still to be incorporated include:

- Developing a DFN model for all fractures (open and sealed) and representing intra-fracture heterogeneity as means to go from geometric DFN modelling to hydraulic DFN modelling.
- Use of semi-stochastic modelling methods to condition fractures and deformation zones to observations and high confidence interpretations.
- Use of genetically generated DFN modelling to produce more realistic patterns of fracture terminations and connectivity.
- Further integration of fracture hydraulic, mechanical properties and rock stresses.

Following these refinements, further calibration of the model parameters will be required.

# References

SKB's (Svensk Kärnbränslehantering AB) publications can be found at www.skb.com/publications.


**Carlsson A, 1979.** Characteristic features of a superficial rock mass in southern central Sweden: horizontal and subhorizontal fractures and filling material. PhD thesis. Uppsala University, Sweden.

**Curtis P, Petersson J, Triumf C-A, Isaksson H, 2009.** Site investigation SFR. Deformation zone modelling. Model version 0.1. SKB P-09-48, Svensk Kärnbränslehantering AB.

**Darcel C, Davy P, Le Goc R, 2012.** Statistical Fracture Domain methodology for DFN modeling applied to site characterization. Proceedings of EUROCK 2012, Stockholm, Sweden, 28–30 May 2012. BeFo (Bergteknisk Forskning) and International Society for Rock Mechanics (ISRM).

**Darcel C, Le Goc R, Davy P, 2013.** Development of the statistical fracture domain methodology – application to the Forsmark site. SKB R-13-54, Svensk Kärnbränslehantering AB.

**Eshelby J D, 1957.** The determination of the elastic field of an ellipsoidal inclusion and related problems. Vol. Proceeding of the Royal Society A 241. doi:10.1098/rspa.1957.0133

**Follin S, 2008.** Bedrock hydrogeology Forsmark. Site descriptive modelling, SDM-Site Forsmark. SKB R-08-95, Svensk Kärnbränslehantering AB.

**Follin S (ed), 2019.** Multidisciplinary description of the access area of the planned spent nuclear fuel repository in Forsmark prior to construction. SKB R-17-13, Svensk Kärnbränslehantering AB.

**Follin S, Stigsson M, 2013.** A transmissivity model for deformation zones in fractured crystalline rock and its possible correlation to in situ stress at the proposed high-level nuclear waste repository site at Forsmark, Sweden. Hydrogeology Journal 22, 299–311.

**Follin S, Levén J, Hartley L, Jackson P, Joyce S, Roberts D, Swift B, 2007.** Hydrogeological characterisation and modelling of deformation zones and fracture domains, Forsmark modelling stage 2.2. SKB R-07-48, Svensk Kärnbränslehantering AB.

**Follin S, Hartley L, Rhén I, Jackson P, Joyce S, Roberts D, Swift B, 2013.** A methodology to constrain the parameters of a hydrogeological discrete fracture network model for sparsely fractured crystalline rock, exemplified by data from the proposed high-level nuclear waste repository site at Forsmark, Sweden. Hydrogeology Journal 22, 313–331.

**Forssman I, Zetterlund M, Forsmark T, Rhén I, 2006.** Correlation of Posiva Flow Log anomalies to core mapped features in KFM06A and KFM07A. Forsmark site investigation. SKB P-06-56, Svensk Kärnbränslehantering AB.

**Forssman I, Forsmark T, Rhén I, 2008.** Forsmark site investigation. Correlation of Posiva Flow Log anomalies to core mapped features in KFM02B, KFM08D and KFM11A. SKB P-07-128, Svensk Kärnbränslehantering AB.

**Fox A, La Pointe P, Hermanson J, Öhman J, 2007.** Statistical geological discrete fracture network model. Forsmark modelling stage 2.2. SKB R-07-46, Svensk Kärnbränslehantering AB.

**Glamheden R, Fredriksson A, Roeshoff K, Karlsson J, Hakami H, Christiansson R, 2007.** Rock mechanics Forsmark. Site descriptive modelling Forsmark stage 2.2. SKB R-07-31, Svensk Kärnbränslehantering AB.

**Goodman R E, Taylor R L, Brekke T L, 1968.** A model for the mechanics of jointed rock. Journal of Soil Mechanics and Foundations Divisin 94, 637–659.

**Gudmundsson A, Løtveit I F, Gjesdal O, 2002.** Fracture-generated permeability and groundwater yield in Norway. NGU Bulletin 439, 61–69.

**Hakala M, Ström J, Valli J, Juvani J, 2019.** Structural control on stress variability at Forsmark. SKB R-19-23, Svensk Kärnbränslehantering AB.

**Hartley L, Roberts D, 2013.** Summary of discrete fracture network modelling as applied to hydrogeology of the Forsmark and Laxemar sites. SKB R-12-04, Svensk Kärnbränslehantering AB.

**Hartley L, Baxter S, Hoek J, Joyce S, Mosley K, Williams T, Fox A, Cottrell M, La Pointe P, Gehör S, Darcel C, Le Goc R, Aaltonen I, Vanhanarkaus O, Löfman J, Poteri A, 2018.** Discrete Fracture Network Modelling (Version 3) in support of Olkiluoto Site Description 2018. Posiva Working Report 2017-32, Posiva Oy, Finland.

**KASAM, 2001.** Nuclear waste: state-of-the-art reports 2001. Stockholm: Swedish National Council for Nuclear Waste.

**Klimczak C, Schultz R A, Parashar R, Reeves D M, 2010.** Cubic law with aperture-length correlation: implications for network scale fluid flow. Hydrogeology Journal 18, 851–862.

**La Pointe P R, Wallmann P C, Dershowitz W S, 1993.** Stochastic estimation of fracture size through simulated sampling. International Journal of Rock Mechanics and Mining Sciences & Geomechanics Abstracts 30, 1611–1617.

**Lei Q, Latham J-P, Tsang C-F, Xiang J, Lang P, 2015.** A new approach to upscaling fracture network models while preserving geostatistical and geomechanical characteristics. Journal of Geophysical Research: Solid Earth 120, 4784–4807.

**Lunkka J P, Moisio K, Vainio A, 2013.** Subglacial hydrology of the lake district ice lobe during the Younger Dryas (ca 12 500–11 600 years ago) in the Kylaeniemi area, SE Finland. Posiva Working Report 2013-12, Posiva Oy, Finland.

**Martel S J, 2006.** Effect of topographic curvature on near-surface stresses and application to sheeting joints. Geophysical Research Letters 33. doi:10.1029/2005gl024710

**Martel S J, 2011.** Mechanics of curved surfaces, with application to surface-parallel cracks. Geophysical Research Letters 38. doi:10.1029/2011gl049354

**Martel S J, 2016.** Effects of small-amplitude periodic topography on combined stresses due to gravity and tectonics. International Journal of Rock Mechanics and Mining Sciences 89, 1–13.

**Martel S J, 2017.** Progress in understanding sheeting joints over the past two centuries. Journal of Structural Geology 94, 68–86.

**Mattila J, Viola G, 2014.** New constraints on 1.7 Gyr of brittle tectonic evolution in southwestern Finland derived from a structural study at the site of a potential nuclear waste repository (Olkiluoto Island). J Journal of Structural Geology 67, 50–74.

**Morland G, 1997.** Petrology, lithology, bedrock structures, glaciation and sea level: Important factors for groundwater yield and composition of Norwegian bedrock boreholes. NGU-rapport 97.122 II, Geological Surbey of Norway.

**Munier R, Stenberg L, Stanfors R, Milnes A G, Hermanson J, Triumf C-A, 2003.** Geological Site Descriptive Model. A strategy for the model development during site investigations. SKB R-03-07, Svensk Kärnbränslehantering AB.

**Mäkelä J, 2012.** Drilled well yield and hydraulic properties in the Precambrian crystalline bedrock of Central Finland. PhD thesis. University of Turku, Finland.

**Oda M, 1986.** An equivalent continuum model for coupled stress and fluid flow analysis in jointed rock masses. Water Resources Research 22, 1845–1856.

**Olofsson I, Simeonov A, Stephens M, Follin S, Nilsson A-C, Röshoff K, Lindberg U, Lanaro F, Fredriksson A, Persson L, 2007.** Site descriptive modelling Forsmark, stage 2.2. A fracture domain concept as a basis for the statistical modelling of fractures and minor deformation zones, and interdisciplinary coordination. SKB R-07-15, Svensk Kärnbränslehantering AB.

**Olson J E, 2003.** Sublinear scaling of fracture aperture versus length: An exception or the rule? Journal of Geophysical Research: Solid Earth 108. doi:10.1029/2001jb000419

**PostGIS, 2017.** PostGIS: Spatial and geographic objects for PostgreSQL. Available at: https://postgis.net/documentation/

**PostgreSQL, 2017.** PostgreSQL: Documentation. Available at: https://www.postgresql.org/docs/

**Saintot A, Stephens M B, Viola G, Nordgulen Ø, 2011.** Brittle tectonic evolution and paleostress field reconstruction in the southwestern part of the Fennoscandian Shield, Forsmark, Sweden. Tectonics 30. doi:10.1029/2010tc002781

**Sandström B, Tullborg E-L, Smellie J, MacKenzie A B, Suksi J, 2008.** Fracture mineralogy of the Forsmark site. SDM-Site Forsmark. SKB R-08-102, Svensk Kärnbränslehantering AB.

**Schultz R A, Mège D, Diot H, 2008a.** Emplacement conditions of igneous dikes in Ethiopian Traps. Journal of Volcanology and Geothermal Research 178, 683–692.

**Schultz R A, Soliva R, Fossen H, Okubo C H, Reeves D M, 2008b.** Dependence of displacement – length scaling relations for fractures and deformation bands on the volumetric changes across them. Journal of Structural Geology 30, 1405–1411.

**SKB, 2008.** Site description of Forsmark at completion of the site investigation phase. SDM-Site Forsmark. SKB TR-08-05, Svensk Kärnbränslehantering AB.

**SKB, 2013.** Site description of the SFR area at Forsmark at completion of the site investigation phase. SDM-PSU Forsmark. SKB TR-11-04, Svensk Kärnbränslehantering AB.

**Stephens M B, 2010.** Bedrock geology – overview and excursion guide. Forsmark site investigation. SKB R-10-04, Svensk Kärnbränslehantering AB.

**Stephens M B, Fox A, La Pointe P, Simeonov A, Isaksson H, Hermanson J, Öhman J, 2007.** Geology Forsmark. Site descriptive modelling Forsmark stage 2.2. SKB R-07-45, Svensk Kärnbränslehantering AB.

**Stephens M B, Follin S, Petersson J, Isaksson H, Juhlin C, Simeonov A, 2015.** Review of the deterministic modelling of deformation zones and fracture domains at the site proposed for a spent nuclear fuel repository, Sweden, and consequences of structural anisotropy. Tectonophysics 653, 68–94.

**Stigsson M, 2008.** Analysis of uncertainty in orientation of fractures coupled to PFL anomalies. Site descriptive modelling SDM-Site Laxemar. SKB P-08-104, Svensk Kärnbränslehantering AB.

**Stigsson M, 2016.** Orientation uncertainty of structures measured in cored boreholes: methodology and case study of Swedish crystalline rock. Rock Mechanics and Rock Engineering 49, 4273–4284.

**Svensson U, 2010.** Darcy Tools version 3.4. Verification, validation and demonstration. SKB R-10-71, Svensk Kärnbränslehantering AB.

**Söderlund P, Hermansson T, Page L M, Stephens M B, 2009.** Biotite and muscovite $^{40}Ar$–$^{39}Ar$ geochronological constraints on the post-Svecofennian tectonothermal evolution, Forsmark site, central Sweden. International Journal of Earth Sciences 98, 1835–1851.

**Terzaghi R, 1965.** Sources of error in joint surveys. Géotechnique 15, 287–304.

**Willis-Richards J, Watanabe K, Takahashi H, 1996.** Progress toward a stochastic rock mechanics model of engineered geothermal systems. Journal of Geophysical Research: Solid Earth 101, 17481–17496.

**Winberg A, Andersson P, Byegård J, Poteri A, Cvetkovic V, Dershowitz W, Doe T, Hermanson J, Gómez-Hernández J J, Hautojärvi A, Billaux D, Tullborg E-L, Holton D, Meier P, Medina A, 2003.** Final report of the TRUE Block Scale project. 4. Synthesis of flow, transport and retention in the block scale. SKB TR-02-16, Svensk Kärnbränslehantering AB.

**Witherspoon P A, Wang J S Y, Iwai K, Gale J E, 1980.** Validity of cubic law for fluid flow in a deformable rock fracture. Water Resources Research 16, 1016–1024.

**Öhman J, Bockgård N, Follin S, 2012.** Site investigation SFR. Bedrock hydrogeology. SKB R-11-03, Svensk Kärnbränslehantering AB.

# Appendix

**Description of each line in a .fab file, an ascii file describing discrete fracture networks.**

| Line # | Parameter/Keyword | Valid Values/Keyword | Example |
|---|---|---|---|
| 1 | BEGIN Format | Keyword, the beginning of format specification | BEGIN Format |
| 2 | Format = | Specification of whether the file is in Ascii or (Ascii) or Babylonian (base 60) notation (Babylonian) | Ascii |
| 3 | Scale = | scale of the box containing all fractures in meters (float) | 100 |
| 4 | XAxis = | coordinate system (right handed) | East or South |
| 5 | NumFractures = | number of fractures in the file (integer) | 200 |
| 6 | NumTessFractures = | number of non-planar (tessellated) fractures (integer) | 5 |
| 7 | NumRockBlocks = | number of cells defining continuum elements (integer) | 2000 |
| 8 | NumNodes = | number of nodes fractures (integer), tessfracture, and rock block | 800 |
| 9 | NumProperties = | number of properties to be assigned to fractures and blocks (integer between 3 and 20) | 3 |
| 10 | NumNodeProps = | number of properties to be assigned to nodes (integer between 0 and 20) | 0 |
| 11 | NumSets = | number of fracture sets (integer) | 5 |
| 12 | END Format | Keyword, the end of format data block | END Format |
| | | Blank line | |
| 13 | BEGIN Properties | Keyword, the beginning of fracture property specification | BEGIN Properties |
| 14 | Prop1 = (Real*4) | Property type (keyword), property name (text of up to 20 characters enclosed in quotes). Repeat this record NumProperties+NumNodeProps times to specify all property names and types. Valid types are (Real*4), (Integer*4), and (Text*20) | Prop1 = (Real*4) ”Transmissivity” |
| 15 | END Properties | Keyword | END Properties |
| | | Blank line | |
| 16 | BEGIN Sets | Keyword, the beginning of fracture set specification | BEGIN Sets |
| 17 | Set1 = | The set name enclosed by a pair of double-quotes, # of characters up to 20. Repeat this record NumSets times | Set1 = “Conjugate Shear A” |
| 18 | END Sets | Keyword | END Sets |
| | | Blank line | |
| 19 | BEGIN Fracture | Keyword for beginning of fracture specification | BEGIN Fracture |
| 20 | Fracture #, # of vertices, Set #, Properties | Fracture number (integer), Number of vertices (integer), set number (integer), Properties (NumProperties float) | 1 4 1 2.300E−06 2.700E−05 1.100E−03 |
| 21 | x,y,z coordinates for the vertex, node properties | Vertex index (integer), x,y,z coordinates (float), node properties if any (float). Repeat for each vertex of the fracture | 1 −1.000000E+02 9.999999E+01 −1.000000E+01 |
| 22 | x,y,z components of fracture unit normal vector | 0 (integer), then, three direction cosines for the unit normal (three float) | 0 2.244704E−01 6.784559E−01 −6.995074E−01 |

| Line # | Parameter/Keyword | Valid Values/Keyword | Example |
|---|---|---|---|
| 23 | | Repeat 20, 21, 22 for each fracture | |
| 24 | END Fracture | Keyword | END Fracture |
| | | Blank Line | |
| 25 | BEGIN TessFracture | Keyword for beginning of non-planar (tessellated) fractures | BEGIN TessFracture |
| 26 | # FractureNum NumNodes NumFaces SetNum Prop1,Prop2, ..., PropN | Fracture Number (integer), number of nodes (integer), number of faces (integer), Set number (integer), properties (NumProp float numbers) | 1 4 2 3 |
| 27 | index, x,y,z coordinates for the first node, node properties | Index (integer), x,y,z coordinates (three float), node properties if any(float).<br>Repeat NumNodes times | −1.000000E+02 9.999999E+01 |
| 28 | FaceNum NumNodes Node1 Node2 | Index (integer), number of nodes defining the face (integer, usually 3), indices for the nodes defining the cell (integers) | 1 3 4 3 2 |
| 29 | | Repeat 26, 27, 28 for all TessFractures | |
| 30 | END TessFrac | Keyword | END TessFrac |
| | | Blank Line | |

Arkitektkopia AB, Bromma, 2021

SKB is responsible for managing spent nuclear fuel and radioactive waste produced by the Swedish nuclear power plants such that man and the environment are protected in the near and distant future.

**skb.se**